SURFACE BRIGHTNESS PROFILES AND COLOR GRADIENTS OF GALAXIES IN THE HUBBLE DEEP FIELDS NORTH AND SOUTH

By

PIMOL MOTH

A DISSERTATION PRESENTED TO THE GRADUATE SCHOOL
OF THE UNIVERSITY OF FLORIDA IN PARTIAL FULFILLMENT
OF THE REQUIREMENTS FOR THE DEGREE OF
DOCTOR OF PHILOSOPHY

UNIVERSITY OF FLORIDA

2003

Copyright 2003

by

Pimol Moth

I dedicate this work to my parents, to Somnang, and to all of the victims of the killing fields.

ACKNOWLEDGMENTS

I would not be here today without the support of the wonderful people in my life. I owe the greatest gratitude to my mother and father, Vilay and Chhakloem, whose courage and determination I admire very much. Here they were in a foreign land with no money, no knowledge of the English language, and with sad memories of a war-torn land, yet they were able to overcome every hardship and challenge. It was because of them that I am allowed the priceless opportunity to do anything I set my mind to. There is no way I will be able to repay them for all that they have given me. I thank my sister, Sochieta; and brother, Komnith. Growing up with them was sometimes enfuriating, but always interesting and fun. They are not only my brother and sister, they are my friends for life. Sochieta inspires me with her strong and independent spirit. Komnith keeps me up to date with current affairs, and will go far in life with his enviable and exasperating ability to maintain a completely calm demeanor in debates. I thank my grandfather, whose multi-talents and very interesting life inspires me to set high goals and reach for the top. I thank my grandmother, who is the best cook in the world; and my aunt, who was the first to expose me to the idea of astronomy (although she probably doesn't remember it). I also thank my grandfather, Loth. Unfortunately, I didn't get a chance to know him too well as an adult, but I remember the bond that I felt for him during my childhood.

I thank my advisor, Richard Elston, whose expertise in the field I respect very much and whose help and guidance were much appreciated. He taught me the value of thinking critically and working independently. I thank Rafael Guzmán who helped me during a critical time. I appreciate very much the time

he unselfishly took out of his schedule to help me. I thank Katherine Wu whose support, encouragement, and advice helped to keep me sane during the hard times. I thank Mark Dickinson for taking the time to help me understand the data better. He explained everything very well in his timely emails to me. I thank Robert Pina for his help on IDL. I thank the members of my thesis committee for taking the time to read my dissertation and attend my oral exam. I thank all the secretaries who do such a good job in keeping the department running smoothly and helping me to get out of some jams.

I owe a great deal of gratitude to all the people in my life who have touched me with their love and friendship. In particular, I thank James Radomski whose patience, wit, and wisdom are unmatchable. He always knows the perfect thing to do and say to lift my spirits. I thank my past and present officemates. Their presence always made the office a pleasant place to work. I thank Ana and Eric for their friendship and for being there for me through the good times as well as the bad. I cherish all the talks we have together. I thank Lauren, Karl, and Ily for their support and friendship. I thank Veera whom I will always consider as a friend because he is always there for people during rough times. I thank Safiyya who is my oldest friend and who is like me in so many ways. I thank Joyce for always being there to listen to me and for sending me cards of encouragement. Last, but not least, I thank Lulu and Patty whose phone conversations and friendship I cherish. They are two of the few people who know me the best, and they will always have a special place in my heart.

Funds for this research were made possible by the NASA Florida Space Grant Consortium, Massey Dissertation Fellowship, the CAREER Grant AST 98 75448, NASA grant: "A NICMOS Map of the HDF", GO-07817.05-96A, and the University of Florida.

TABLE OF CONTENTS

page

ACKNOWLEDGMENTS iv

ABSTRACT viii

CHAPTERS

1 INTRODUCTION 1

1.1 Lyman-break Technique 2
1.2 Nature of Lyman-break Galaxies 3
1.2.1 Optical and Near-Infrared Spectroscopy 4
1.2.2 Morphology 5
1.2.3 Spatial Clustering 7
1.2.4 Mass Spectrum 7
1.3 Thesis Topic 9
1.3.1 Surface Brightness Profiles as a Probe of Morphologies . . . 10
1.3.2 Color Gradients as Probes of the Distribution of Stellar Populations 11
1.3.3 The Big Picture: Comparing Observations with Theoretical Models 12

2 METHODOLOGY 14

2.1 Data and Sample Selection 14
2.2 Point Spread Function Matching 18
2.3 Surface Photometry 21
2.4 Fitting Surface Brightness Profiles 23
2.5 Creating Model Galaxies to Account for PSF Effects 24
2.6 Generating Color Profiles and Determining the Gradients 26
2.7 K-corrections 32

3 RESULTS 34

3.1 Surface Brightness Profiles 35
3.1.1 Hubble Deep Field-North 42
3.1.2 Hubble Deep Field-South 48
3.1.3 Hubble Deep Field-North vs Hubble Deep Field-South . . . 55
3.1.4 Discussion 57

3.2 Color Profiles 63
3.2.1 Hubble Deep Field-North 64
3.2.2 Hubble Deep Field-South 74
3.2.3 Hubble Deep Field-North vs. Hubble Deep Field-South . . 81
3.2.4 Discussion 82

4 SOURCES OF UNCERTAINTIES 88

4.1 Correlation of Pixels 88
4.2 Uncertainties due to Background Subtraction 90
4.3 Dust Obscuration 92
4.4 Selection Effects 93

5 COMPARISONS WITH THEORETICAL MODELS 96

5.1 Comparisons with the BCFL98 Model 97
5.2 Comparisons with the SPF01 Model 98

6 THE NATURE OF LYMAN-BREAK GALAXIES REVISITED 101

7 CONCLUSIONS AND SUGGESTIONS FOR FUTURE WORK 105

7.1 Conclusions 105
7.2 Suggestions for Future Work 107

APPENDIX K-CORRECTION AND COLOR TABLES 109

REFERENCES 142

BIOGRAPHICAL SKETCH 148

Abstract of Dissertation Presented to the Graduate School
of the University of Florida in Partial Fulfillment of the
Requirements for the Degree of Doctor of Philosophy

SURFACE BRIGHTNESS PROFILES AND COLOR GRADIENTS OF GALAXIES IN THE HUBBLE DEEP FIELDS NORTH AND SOUTH

By

Pimol Moth

December 2003

Chair: Richard J. Elston
Major Department: Astronomy

With the availability of the Hubble Deep Fields, we can now probe the properties of galaxies spanning a large range of redshifts at higher resolution and depths than before. Here, I fit elliptical isophotes to the Hubble Deep Fields North and South Wide Field Planetary Camera 2 (WFPC-2) and Near Infrared Camera and Multi-Object Spectrometer (NICMOS) imaging data to study the rest-frame B surface brightness profiles and rest-frame $(UV_{218} - U_{300})_0$, $(U_{300} - B_{450})_0$, and $(B_{450} - V_{606})_0$ color gradients of 20 low-redshift galaxies ($0 < z < 0.5$), 75 intermediate-redshift galaxies ($0.5 \leq z \leq 1.2$) with $I_{814} < 25$, and 70 high-redshift galaxies ($2.0 \leq z \leq 3.6$) with $H_{160} < 27$. I demonstrate the importance of correcting for Point Spread Function (PSF) effects when evaluating the surface brightness profiles since at small scale lengths and faint magnitudes, an $r^{1/4}$ profile can be smoothed out substantially to become consistent with an exponential profile. After taking account for profile smoothing due to the PSF, I found that at higher look-back time, there may be a slight increase in the fraction of galaxies possessing exponential profiles and a slight decrease in the fraction of galaxies possessing $r^{1/4}$ profiles. Results also suggest a statistically insignificant increase in

the fraction of peculiar/irregular type galaxies. From the weighted least-squares fit to the color profiles, I found that at low and intermediate-redshifts, the galaxies possess negative color gradients, indicating a reddening towards the center of the profile; whereas at high-redshifts, the galaxies possess strong positive color gradients, indicating that star formation is more centrally concentrated. This differs from the prevalent mode of extended-disk star formation that is observed in the local universe. After comparing my results with previous observations and recent semi-analytic models that treat galaxy formation and evolution using the cold dark matter (CDM) hierarchical framework, I concluded that the high-redshift galaxies are undergoing mergers. At this stage, these galaxies may predominantly possess $r^{1/4}$ light profiles and are forming stars at a high rate in their central regions. Over time, mergers and interactions may cause the morphologies of galaxies to change and the locations of the star forming regions to shift from the central to the outer parts of the galaxies.

CHAPTER 1
INTRODUCTION

What is the nature of high-redshift galaxies and how do they evolve with time? These are two of the most important questons in astronomy. To answer these questions, we must be able to compare and contrast the properties of galaxies at different redshifts. From numerous multi-wavelength observations of galaxies spanning all morphological types, we now have a good understanding of the properties of present-day galaxies and a wealth of information about galaxies at $z \leq 1.0$, but our knowledge of the properties of galaxies at higher redshifts remains limited. However, over the past several years much advancement has been made in this topic because of the numerous detections of $z \geq 3$ galaxies using the Lyman-break technique (Section 1.1) which allowed us for the first time to directly detect large numbers of galaxies in a young state (Steidel and Hamilton 1993). Understanding the properties of these Lyman-break galaxies (LBGs) when the universe was $\sim 10\%$ of its current age is critical in our efforts to better understand galaxy formation and evolution.

With the availability of the Hubble Deep Fields North and South (HDF-N and HDF-S) (Casertano et al. 2000; Dickinson 1999; Dickinson et al. 2000; Fruchter et al. unpublished 2000; Thompson et al. 1999; Williams et al. 1996), we can probe to fainter surface brightness limits and smaller angular scales than before, the sizes, shapes, and colors of distant galaxies which were too faint and unresolved to be studied in detail by ground-based observations alone. Furthermore, near-infrared data from NICMOS combined with optical data from WFPC-2 give us the unique opportunity to compare surface brightness properties of galaxies with the same rest-frame wavelengths over a wide range of redshifts.

1.1 Lyman-break Technique

In their Lyman-break technique to detect $z \geq 3$ galaxies, Steidel and Hamilton (1993) used a custom suite of broadband filters (U_n, G, $\mathcal{R}$) specifically chosen to isolate the two most conspicuous features in the spectrum of cosmologically distant star-forming galaxies: the flat UV continuum and the strong Lyman-limit spectral break at 912Å (which is a combined product of the intrinsic stellar energy distributions, intervening absorbers, and the galaxy's inherent opacity to Lyman continuum photons) (Steidel and Hamilton 1993). Figure 1-1 shows the main ideas behind the Lyman-break technique. In this technique, filters are placed on either side of the redshifted Lyman-limit to detect high-redshift objects by their pronounced spectral break.

Since the F300W filter in WFPC-2 extends to shorter wavelengths than the U_n filter used by Steidel and Hamilton (1993), the passage of the Lyman-limit into this passband occurs at lower redshifts. Thus, the Lyman-break technique can be used to detect galaxies with $z \geq 2.0$ in the HDF. Applying the color selection criteria from Steidel et al. (1996a) to the filters of the HDF, we can then assume that an object is a Lyman-break galaxy candidate having $z \geq 2.0$ if it satisfies the following color criteria (Dickinson 1998):

$$(U_{300} - B_{450}) \geq 1.0 + (B_{450} - V_{606});\ (B_{450} - V_{606}) \leq 1.2;\ (V_{606}) \leq 27 \qquad (1.1)$$

The 25 brightest galaxies in the HDF-N that were detected using these selection criteria were all spectroscopically confirmed to have redshifts $z \geq 2.0$ (Lowenthal et al. 1997; Steidel et al. 1996a), verifying that this technique is extremely robust. The only major interlopers that could potentially be falsely detected by this color selection are galactic stars. However, they are easily identified by eye and are excluded from the candidate list. The second criterion limits the selection of galaxies to $z \simeq 3.5$. Beyond these redshifts, there is significant absorption of the V_{606} passband due to the line blanketing of the Lyman-α forest which makes the

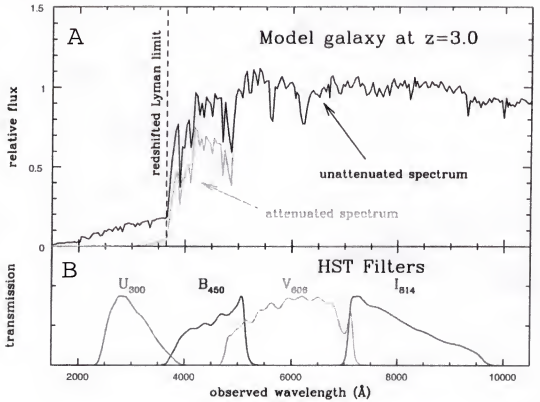

Figure 1–1: Lyman-break technique. A) Spectrum of a model star forming galaxy at $z = 3.0$. The dashed line marks the location of the redshifted Lyman-limit. B) Transmission functions of the WFPC-2 HST filters (from Dickinson, M. 1998, in STScI Symp. Ser. 11, The Hubble Deep Field, ed. M. Livio, S.M. Fall, & P. Madau (New York: Cambridge University Press), Figure 1, 219)

observed colors of these galaxies difficult to distinguish from the colors exhibited by intrinsically red galaxies at lower redshifts.

1.2 Nature of Lyman-break Galaxies

Although the nature of LBGs is not yet well constrained since they have only been detected in large numbers within the last decade, much headway has been made because of the increasing number of imaging and spectroscopic observations of LBGs at a broad range of wavelengths. These recent observations have revealed some important clues to understanding the nature of LBGs. Here I summarize some important results from these previous observations.

1.2.1 Optical and Near-Infrared Spectroscopy

Optical spectroscopic observations of LBGs probing their rest-frame ultraviolet spectrum have revealed many similarities between their spectra and the spectra of local starburst galaxies (Giavalisco 2002; Lowenthal et al. 1997; Pettini et al. 2000; Steidel et al. 1996a, 1999, 2001). Like starbursts, LBGs possess strong blue continua (which indicates the presence of young, massive O and B stars). Furthermore, they also possess strong interstellar absorption lines such as C II, O I, Si II, and Al III; and high-ionization stellar lines such as He II, C IV, Si IV, and N V, albeit there is some variation in the line strength and morphology with each galaxy. Although the spectra of LBGs are very similar to local starbursts, their UV luminosities have been observed to be between 100 and 1500 times higher than that of the star-forming knots seen in local starbursts (Giavalisco 2002; Pettini et al. 2000; Steidel et al. 1999). Thus, stars seem to be forming at a much higher rate in LBGs than in local starbursts.

Pettini et al. (1998, 2001) showed that it was possible to study the spectra of LBGs in the near-IR using some of the largest ground-based telescopes. In principal, using optical spectroscopy to sample the rest-frame ultraviolet continuum produced predominantly by O and B type stars is a more direct method for determining the SFR of galaxies. However, great uncertainty exists regarding the degree of attenuation of UV luminosities by dust. By observing the $z \geq 3$ galaxies in the near infrared, they were able to reduce this problem, since the rest-frame optical wavelengths are much less affected by dust. From their observations of the Hβ, [OII] λ 3727, and [OIII] $\lambda\lambda$ 4959,5007 nebular emission lines, Pettini et al. (1998, 2001) found that the star-formation rates of LBGs deduced from the Hβ line ($20 - 75\ M_{\odot}\ yr^{-1}$) are within the range of values measured using UV luminosity; and that the oxygen abundance can range from as high as solar or as low as $\sim 1/10$ solar.

1.2.2 Morphology

Optical and near-IR imaging of LBGs from both ground-based surveys and the Hubble Deep Fields reveal that LBGs have a variety of morphologies, ranging from relatively regular systems to systems with complicated and irregular substructure (Abraham et al. 1996; Giavalisco et al. 1996; Lowenthal et al. 1997; Steidel et al. 1996a, 1996b). Although LBGs seem to possess a mix of morphologies, they also generally share many common characteristics. On the whole, the Lyman-break population seems to be smaller, more irregular, and more compact than its local counterparts. Figure 1-2 shows some of the galaxies in the HDF-N spanning the U_{300} passband to the H_{160} passband. Most of the LBGs in the figure are undetected in the U_{300} passband because of the flux suppression due to the redshifted Lyman-limit into this passband. Because of this, LBGs are sometimes referred to as "U-dropouts". It is evident that LBGs do not resemble the traditional Hubble sequence of galaxies, since we cannot identify structures such as spiral arms, bulges, disks, and bars. Instead, they seem to possess either one bright core or multiple cores surrounded by fragmented substructures with underlying diffuse nebulosity that are suggestive of merger events or interactions. Although it is evident that these LBGs look very different from galaxies in the traditional Hubble sequence, it is still unclear what type of galaxies they represent and what they will evolve into. From observations of star-formation rates, masses, physical sizes, space density, and morphologies, some (Baugh et al. 1998; Giavalisco et al. 1996; Steidel et al. 1996a, 1996b) believe that these LBGs reside in the centers of very massive dark matter haloes and are the direct progenitors of today's most luminous ellipticals or spiral bulges. In this scenario, LBGs are almost fully assembled and have been forming stars quiescently for over ~ 1 Gyr. However, others believe that LBGs are either the progenitors of low-mass spheroidal galaxies or are low-mass star-bursting objects that have not yet fully assembled but will

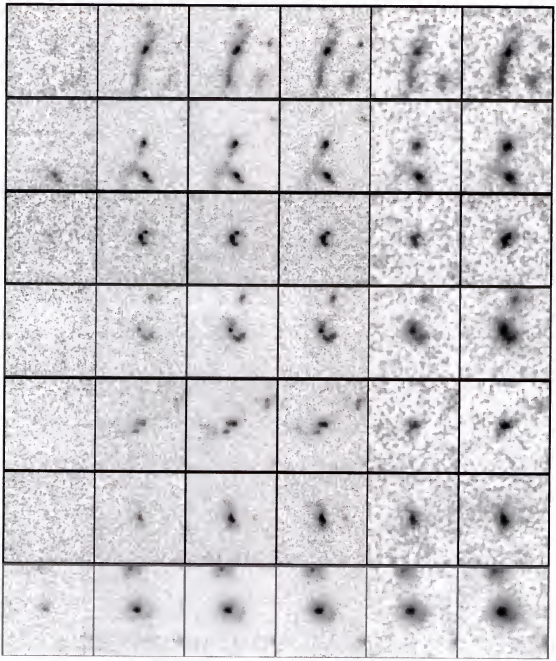

Figure 1–2: Some images of LBGs in the HDF-N taken in the U_{300} through H_{160} passbands. (from Dickinson, M. 1998, "A Complete NICMOS Map of the Hubble Deep Field", The Space Telescope Science Institute, Retrieved May, 2003 from http://nemesis.stsci.edu/~med/hdfNIC7817)

eventually merge to become the larger and more luminous galaxies we see today (Lowenthal et al. 1997; Sawicki and Yee 1998; Sommerville et al. 2001).

1.2.3 Spatial Clustering

Now that we are able to detect LBGs in large numbers, it is possible to study their correlation function and number counts. Many observations consistently reveal that the LBGs exhibit strong spatial clustering (Arnouts et al. 1999; Connolly et al. 1998; Giavalisco and Dickinson 2001; Giavalisco et al. 1994, 1998; Steidel et al. 1998). However, many of these studies may be biased because of large variations in the volume density probed. But given that the effect of the bias is to underestimate the value of the correlation length (Porciani and Giavalisco 2002), the conclusion that LBGs exhibit strong spatial clustering with a correlation length of at least $r_0 \sim 4h^{-1}$ Mpc still holds (Adelberger et al. 1998; Arnouts et al. 1999; Connolly et al. 1998; Giavalisco and Dickinson 2001; Giavalisco et al. 1998). This strong clustering seen in the galaxy's light combined with the weak clustering of the mass predicted by gravitational instability and the cluster normalization at $z \sim 3$ imply that the spatial distribution of LBGs must be biased with respect to the mass (Giavalisco 2002). This means that these galaxies tend to congregate in the peaks of the mass-density field that are more clustered than the average distribution. Given that the bias observed in LBGs is predicted by theory to be collapsed perturbations of dark matter halos (Bardeen et al. 1986; Kaiser 1984), the clustering of LBGs can be used as a powerful tool to test current models of structure formation.

1.2.4 Mass Spectrum

The robust determination of individual masses of galaxies and the overall mass spectrum is crucial in determining whether LBGs are fully assembled; and is the key ingredient in constraining theories of galaxy formation and evolution. However,

because it is difficult to observe these faint high-redshift galaxies, estimates of their masses are uncertain.

The nebular emission line studies of LBGs conducted by different groups (Kobulnicky and Koo 2000; Moorwood et al. 2000; Pettini et al. 1998; Teplitz et al. 2000a, 2000b) consistently reveal that LBGs have dynamic masses that range from 10^{10} and 10^{11} $M_{\odot}$. These estimates are on the same scales as the masses of low to intermediate-luminosity ellipticals and the bulges of $L*$ galaxies (Bender et al. 1992). These conclusions must be viewed with caution since the $(1 + z)^4$ surface brightness dimming would tend to restrict the observations to only the brightest, central part of the galaxy. Furthermore, the emission line regions of local starburst galaxies are known to be mostly confined to the nuclear regions, and thus may not sample the full potential well (Lehnert and Heckmann 1996). If the same can be said of LBGs then these velocity and mass estimates represent lower limits rather than total values. In addition, it is not currently known at what level nongravitational motions (such as large scale outflows and SN events) contribute to the line widths. If the line widths are dominated by these turbulent motions rather than by gravitational motions, then the observed masses could be over-estimated. Although Pettini et al. (2001) observed large-scale outflows (such as galactic-scale superwinds) that can travel at speeds up to several hundred kms^{-1}, it is still uncertain to what degree these motions affect the overall kinematics of the gas.

The total mass of the individual galaxies can also be measured by obtaining the B-band luminosity and multiplying it by the total mass-to-light ratio. At moderate redshifts, the total mass-to-light ratio for starbursts is ~ 100 in solar units. However, since LBGs form stars at much higher rates (Madau et al. 1996; Steidel et al. 1999), their total mass-to-light ratio is about half that of the starbursts, ~ 50 solar units (Giavalisco 2002). By multiplying this value by the rest-frame B-band luminosity obtained by fits to the stellar population synthesis models (Papovich et

al. 2001; Shapley et al. 2001), the total masses of LBGs were found to be between 10^{11} and 10^{13} $M_{\odot}$.

From observations of their spatial clustering, the total mass estimates of LBGs can also be obtained by determining the mass spectrum of the halos that reproduce both the observed volume density and the correlation length (Adelberger et al. 1998; Bullock et al. 2002; Giavalisco 2002; Giavalisco and Dickinson 2001; Porciani and Giavalisco 2002). This method reveals that the total masses of LBGs are between 5×10^{10} and $5 \times 10^{12} M_{\odot}$ which is in general agreement with the mass predictions derived by using the total mass-to-light ratio, but in disagreement with the predictions from kinematic line studies.

From the preceding discussion, it is evident that the masses of LBGs are not yet well constrained by observations. The masses predicted from theoretical models are just as uncertain. Since the mechanics of star formation is complex and not well understood in LBGs, it is nontrivial to include its effects in theoretical models. Because of different assumptions about the triggers of star formation in LBGs, different models predict different values for the mass spectrum of the galaxies. In semi-analytic models that assume that star formation is induced by merger events (Mustakas and Somerville 2002; Somerville et al. 2001; Wechsler et al. 2001), LBGs are predicted to be systems of small masses that reside in much larger and more massive halos. In N-body simulations that assume that the star formation is governed by the hydrodynamics of the baryonic gas, LBGs are predicted to have higher masses (Baugh et al. 1998).

1.3 Thesis Topic

Although we are now able to detect LBGs in large numbers, we still do not know which scenario best describes their nature. Since they are located at such high-redshifts, they are so faint and have such small scale lengths that it is difficult to observe them with ground-based telescopes. The main uncertainties in the

observations of these galaxies stem from low number statistics and inadequate resolution and depths at which they are observed. In this dissertation, I study the properties of the galaxies at two different pointings using the high quality data from the HDF-N and HDF-S. This is important because it will help to improve the statistics and reduce the possible bias in the results that may be attributed to line-of-sight clustering. These two fields also allow me to observe a larger sample of LBGs, ~ 100, at higher depths and resolution than any ground-based observations. By using these high-quality datasets, we can reduce the uncertainties, and thus better understand the nature of LBGs. We can come closer to understanding whether LBGs are fully assembled massive galaxies that are forming stars quiescently; or whether they reside in low-mass haloes and are forming their stars through intense bursts. Furthermore, by comparing the properties of galaxies at low and intermediate-redshifts with the properties of high-redshift LBGs, we can better understand galaxy evolution from an observational standpoint.

1.3.1 Surface Brightness Profiles as a Probe of Morphologies

With the availability of the Hubble Deep Fields we can now probe the morphologies of galaxies at higher redshifts than have been studied in the past. Van Den Bergh et al. (1996, 2000) visually classified the morphologies of galaxies with $21 < I_{814} < 25$ mag in the HDF-N. However, they were not able to include Lyman-break galaxies in their sample. At present, morphological studies of LBGS are rare because of limitations in resolution and surface brightness. In many cases, isophotal analyses show that many LBGs possess smooth morphologies that could be characterized by either an $r^{1/4}$ or an exponential profile (Giavalisco 2002). However, they seem to be more compact and more irregular than local galaxies and do not resemble the traditional Hubble sequence (Abraham et al. 1996; Van Den Bergh et al. 1996, 2000). Marleau and Simard (1998) conducted a study of the

morphology of galaxies in the HDF-N by using a profile decompositiom method on 522 galaxies down to $I_{814} < 26$. Their results indicated a decrease in the fraction of bulge-dominated galaxies with look-back time. In this study, I produce surface brightness profiles of galaxies to probe the global galaxy structure and classify the morphologies of galaxies at intermediate and high-redshifts. By comparing galaxies at different redshifts, I can determine whether there has been evolution in their morphologies. Although surface brightness profiles should not be viewed as a robust method to constrain the morphologies of galaxies, they can reveal the presence of general trends and are less subjective in nature than visual classification.

When studying the surface brightness profiles of such faint and small galaxies as those in the Hubble Deep Fields, it is important to take into account the effects of the PSF. In this study, I create models of elliptical and disk galaxies spanning a range of magnitudes and scale lengths; and convolve them with the PSF in order to compare them with the observed sample of galaxies. In this way, I was able to more accurately classify their morphologies. By using the surface brightness profiles of the galaxies, which is an independent study of the morphologies of the galaxies, results from this study can be compared with past studies of galaxy morphologies.

1.3.2 Color Gradients as Probes of the Distribution of Stellar Populations

Another observational test of galaxy evolution is the study of color gradients, which will give us an idea of the distribution of stellar populations in the galaxies and whether this distribution changes with time. The study of color gradients will also help us to understand whether the star formation in LBGs is quiescent or whether it occurs in bursts. Because of limits in resolution, the study of the color profiles of galaxies has been predominantly restricted to the low and intermediate-redshift regimes. Previous studies of early-type galaxies at $z \leq 1.0$ showed that they tend to have redder colors in their central regions and gradually become bluer outwards (Franx et al. 1989; Peletier 1990; Tamura and Ohta 2000; Tamura et al.

2000; Vader et al. 1988). This trend in the color profiles can be explained by either a stellar age or metallicity gradient (which becomes degenerate at $z = 0$) (Silva and Elston 1994). Most studies concur that models involving the metallicity gradient best reproduce the color gradients seen in early-type galaxies at $z \leq 1.0$. On the other hand, the gradients observed in late-type galaxies may be due to both age and metallicity effects (de Jong 1996). That is, the central parts of the galaxies in general have older stars and higher metallicity than the outer parts causing them to have redder colors toward the centers.

The deep, high resolution, multi-wavelength data from the HDFs give us the rare opportunity to determine the color profiles of galaxies at higher redshifts than those studied in the past. In this dissertation, I performed a weighted least-squares fit to the color profiles to determine the color gradients of the galaxies. To assess whether the distribution of the stellar populations has evolved, I compared the rest-frame ultraviolet and optical color gradients of LBGs to those at low and intermediate-redshifts. I also explored the processes that may be responsible for any trends detected in the color profiles at different redshifts, while keeping in mind all of the uncertainties involved. To accurately interpret the color gradients, I discuss uncertainties due to background subtraction, correlation of pixels, dust, and selection effects since they can all produce artificial color gradients.

1.3.3 The Big Picture: Comparing Observations with Theoretical Models

No study of galaxy evolution would be complete unless it includes a comparison with theoretical models. Previously, it was thought that galaxies were formed at high-redshifts from a monolithic collapse (Eggen et al. 1962; Tinsley & Gunn 1976). This scenario held that galaxies formed most of their stars from a single burst of star formation and then evolved quiescently through time. These galaxies would then be the direct progenitors of the luminous ellipticals and spiral bulges that we see today.

Currently, the hierarchical structure formation model (Baugh et al. 1998; Cole et al. 1994; Kauffman et al. 1997; Roukema et al. 1997; White & Frenk 1991) represents the popular framework for how structure formed and evolved in the universe. This model assumes that the universe is dominated by nonbaryonic dark matter, which only interacts with visible matter through its gravitational influence and ultimately determines where galaxies will form. It predicts that gravitational perturbations in the early universe cause the smallest mass fluctuations to collapse first and then to merge into larger structures, until they form the mature galaxies we observe today.

Early versions of these models assumed specific values of the Hubble constant (H_0) and cosmological density (Ω) parameters. Under these assumptions, the model predicted a late formation age of massive luminous galaxies. These conclusions conflicted with some existing observations of galaxies in distant clusters that dated the formation epoch of the oldest stellar population at $z > 2$ (Aragón-Salamanca et al. 1993; Ellis at al. 1997; Stanford et al. 1995, 1998). Recently, models of hierarchical structure formation have become more generalized and allow input of different values of cosmological parameters. Using the currently favored values of H_0 and Ω, many simulations now allow for early formation of massive galaxies that have completed the bulk of their star formation and exhausted their fuel on short timescales. Baugh et al. 1998 (BCFL98) and Somerville et al. (2001) (SPF01) used semi-analytical models under this hierarchical framework to analyze the properties of the high-redshift Lyman-break galaxies. To interpret the trends noted in observations and to understand how they fit in with the overall picture of galaxy formation and evolution, I compared my results with these recent semi-analytical models that invoke the cold dark matter hierarchical framework. In this study, I assumed a cosmology where $H_0 = 71 kms^{-1}Mpc^{-1}$, $\Omega_0 = 0.3$, and $\Lambda_0 = 0.7$.

CHAPTER 2
METHODOLOGY

2.1 Data and Sample Selection

The original HDF-N data were a Director's Discretionary program on HST designed to image a field at high galactic latitude using the WFPC-2 camera in four passbands spanning the wavelengths $0.3 - 0.8$ μm (Williams et al. 1996). These WFPC-2 images spanned limiting magnitudes of $\sim AB = 28$ for the F300W, F450W, and F606W passbands and $AB = 28.7$ for the F814W passband. At low-redshifts, these images were sufficient to study the galaxies in the rest-frame optical wavelengths. However at $z > 1$, the WFPC-2 images could only be used to study the rest ultraviolet properties of the galaxies, since their rest optical wavelengths were shifted into the near-IR. Near-IR data of galaxies in the HDF-N were available from ground-based observations (Dickinson et al. 1998; Hogg et al. 1996). However, since the ground-based data were taken at much lower resolution ($\sim 1''$) and reached shallower depths than did the WFPC-2 images, it was very difficult to compare the properties of high-redshift galaxies with their lower redshift counterparts at the same rest-frame wavelengths. To address this problem, I used data taken by Dickinson et al. (1999, 2000) who embarked on a General Observer's (GO) Program 7817 to image the entire WFPC-2 region (5.9 arcmin^2) of the HDF-N in the near-IR using the NICMOS Camera 3 F110W and F160W filters. The data reached an average depth of $AB = 26.1$ in F110W and F160W with an SNR of 10 in $0.''7$ diameter aperture and has a PSF of FWHM $= 0.''22$ after the dithered data was combined by drizzling.

Given that the HDF-N represents only one position in the sky and probes only a small volume, the results may be biased, particularly since observations

show that there may be strong clustering at $z > 2$. To improve the statistics and keep the bias to a minimal, I increased the sample size by exploring a different area of the sky. The obvious choice was the data from the HDF-S WFPC-2 and NICMOS fields, since I could analyze the galaxies at approximately the same depths and resolution as the HDF-N. However, in the HDF-S, the PSF matching of the F110W and F160W filters to that of the F222M filter (Section 2.2) resulted in an effective FWHM $\sim 0.''33$ which is somewhat less than that of the HDF-N. But this resolution is much better than can be found in any other deep near-IR imaging dataset taken by ground-based observations, all of which have FWHM of no better than $\sim 0.''7$. It is important to note that for the HDF-S, the NICMOS observations were taken at a different pointing than the WFPC-2 observations and also have different fields of views. The WFPC-2 observations reached a limiting depth of $\sim AB = 28$ in F450W, F606W, and F814W; and a depth of ~ 27 in F300W with a SNR of 10 in 0.2 square arcseconds (Casertano et al. 2000). After PSF matching was performed, the resulting FWHM was $\sim 0.''2$. The NICMOS Camera 3 observations reached a limiting depth of $\sim AB = 27$ in F110W and F160W, and $AB = 24$ in F222M with an SNR of 10 in 0.8 square arcsecs (Fruchter et al. 2000). The FOV of the Southern HDF NICMOS field is 1 arcmin^2 which is 1/6 the size of the WFPC-2 and NICMOS fields of the HDF-N. The HDF North and South WFPC-2 and NICMOS imaging data had already been reduced by the Space Telescope Science Institute to remove basic instrumental effects and were combined using the Drizzle procedure (Fruchter and Hook 2002). Sky subtraction and image registration between the different filters had also been performed for these data.

Since I compare the properties of galaxies at a range of redshifts, it is important to establish what is meant by low, intermediate, and high-redshift galaxies. I

define *low-redshift* galaxies as those having redshifts of $0.1 \leq z \leq 0.5$; *intermediate-redshift* galaxies as those having redshifts of $0.5 \leq z \leq 1.2$; and *high-redshift* galaxies as those having redshifts of $2.0 \leq z \leq 3.6$. I also sometimes refer to these high-redshift galaxies as Lyman-break Galaxies (LBGs) since they were identified with the Lyman-break technique. I do not include galaxies with $1.2 \leq z \leq 2.0$ in the sample because at these redshifts, there are no prominent optical features to robustly constrain the redshifts.

It is important to study the properties of the galaxies at different redshifts at the same rest-frame wavelengths, because some galaxies might experience what is called morphological K-corrections. This is a phenomenon that occurs when galaxies at different redshifts look different when viewed through the same passband, since the passband would represent different rest-frame wavelengths. For example, the I_{814} image for a galaxy at redshift $z = 0.5$ would reflect the properties of the galaxy at the rest optical wavelengths whose light would include both young and old stellar populations; whereas for a galaxy at redshift $z = 3$, the I_{814} image would represent the rest-UV wavelengths of the galaxy which is dominated by the younger, bluer stellar populations. Thus, if we want to compare the properties of the same stellar populations, we need to choose our passbands such that they reflect the same rest wavelengths at all redshifts.

To avoid the morphological K-correction problem, I studied the intermediate-redshift galaxies in the HDF-N using the WFPC-2 images taken in the F450W (B_{450}), F606W (V_{606}), and F814W (I_{814}) passbands; and the high-redshift galaxies using the WFPC-2 F814W (I_{814}) and NICMOS CAM3 images taken in F110W (J_{110}) and F160W (H_{160}) to probe their rest-frame U_v, U, and B properties. In the HDF-N, the sample consists of 33 intermediate-redshift galaxies with $I_{814} < 25$ identified by spectroscopic redshifts (Cohen et al. 1996; Zepf et al. 1997) and 50 high-redshift galaxies with $H_{160} < 27$, 25 of which were identified by spectroscopic

redshifts (Lowenthal et al. 1997; Steidel et al. 1996a) and 25 by photometric redshifts (Budávari et al. 2000).

Because of the availability of the F222M (K_{222}) passband in the HDF-S, I could probe to longer rest-frame wavelengths than the HDF-N sample. By using the K_{222} passband, I could study the rest-frame V properties of the LBGs. To study galaxies at the same rest-frame wavelengths as the high-redshift sample, I probed galaxies at low and intermediate-redshifts using the WFPC-2 data. I studied the low and intermediate-redshift galaxies in the HDF-S WFPC-2 images using the B_{450}, V_{606}, and I_{814} data; and the high-redshift galaxies using NICMOS CAM3 images taken in J_{110}, H_{160}, and K_{222} to probe their rest-frame U, B, and V properties. In the HDF-S, the sample consists of 20 low-redshift galaxies and 42 intermediate-redshift galaxies with $I_{814} < 25$, and 20 high-redshift galaxies with $H_{160} < 26$ all of which were identified by photometric redshifts (Chen et al. 1998; Gwyn and Hartwick 1996; Yahata et al. 2000). Table 2-1 summarizes the data and sample selection for the two HDF fields.

Table 2–1: The Hubble Deep Fields North and South data and sample

Field	RA(J2000)	Dec(J2000)	FOV[a]	Camera	Filters	#	Redshifts
HDF-N	12:36:49.4	62:12:58.0	5.9	WFPC-2	B_{450}, V_{606}, I_{814}	33	0.5 – 1.2
HDF-N	12:36:49.4	62:12:58.0	5.9	WFPC-2	I_{814}	50	2.0 – 3.5
				NICMOS	J_{110}, H_{160}		
HDF-S	22:32:56.2	−60:33:02.7	5.9	WFPC-2	B_{450}, V_{606}, I_{814}	20	0.1 – 0.5
						42	0.5 – 1.2
HDF-S	22:32:51.7	−60:38:48.2	1.0	NICMOS	J_{110}, H_{160}, K_{222}	20	2.0 – 3.6

[a] arcmin^2

By combining the results from the two Hubble Deep Fields, the conclusions will be more reliable since the statistical errors will be reduced. To fairly interpret the results from the two fields, the characteristics of the sample of galaxies in the two fields must not be too divergent from each other to ensure that the results are not biased by the sample selection. The histogram of the distribution of the redshifts in the intermediate and high-redshift sample in the two fields are shown in Figure 2-1. The median redshifts of the intermediate-redshift galaxies are 0.752

and 0.620 for the HDF-N and HDF-S repectively. The median redshifts of the high-redshift galaxies are 2.55 and 2.39 for the HDF-N and HDF-S respectively. From the plots and from the values of the medians, we can see that there is not too much difference between the HDF-N and HDF-S sample in terms of the distribution in redshifts. Figure 2-2 shows the distribution of magnitudes for the intermediate and high-redshift sample in the two fields. From the histograms, it is clear that the distribution of magnitudes in the two Hubble Deep Fields are similar in both shape and amplitude. Furthermore, the medians of the distributions differ by only an insignificant amount. The median of I_{814} mags for the intermediate-redshift galaxies is 22.94 in the HDF-N and 23.08 in the HDF-S. The median of H_{160} mags for the high-redshift galaxies is 24.95 in the HDF-N and 24.85 in the HDF-S.

2.2 Point Spread Function Matching

To perform accurate color gradient analysis, it is important that the PSFs of the different filters match since differences in the the shape of the PSFs can result in artificial color gradients. For the HDF-N, PSF matching of the B_{450}, V_{606}, I_{814}, and J_{110} images to the H_{160} image had already been performed (Dickinson et al. 1999, 2000) resulting in an effective resolution of $\sim 0.''22$. For the HDF-S NICMOS and WFPC-2 images, I used the IRAF task PSFMATCH in order to produce the convolution kernel needed to degrade the higher resolution PSFs to match the poorer resolution PSF. For the NICMOS images, this involved matching the J_{110} and the H_{160} PSFs to the K_{222} PSF. For the WFPC-2 images, this involved matching the V_{606} PSF to the resolution of the I_{814} PSF. To perform the PSF matching, it is important to choose stars that are unsaturated and well isolated. In the HDF-S NICMOS image, all of the stars in the field are unsaturated. This is because the image was sampled repeatedly in order for the pipeline software to be able to detect saturated pixels and discard them during readout (Dickinson, 2003 private communication). Out of the four stars in the field, I performed PSF

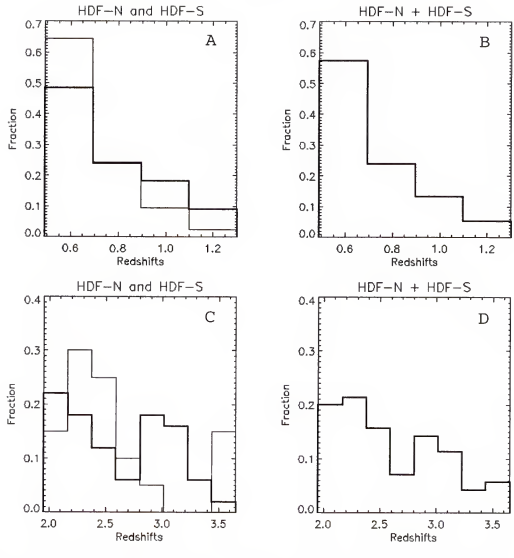

Figure 2–1: Redshift distribution of galaxies in the HDFs North and South sample. A) The redshift distribution of the intermediate-redshift sample in the HDF-N (bold) and HDF-S (normal). The distribution is normalized to the total number of intermediate-redshift galaxies in the respective fields. B) The redshift distribution of all the intermediate-redshift galaxies in the HDF-N and HDF-S combined. The distribution is normalized to the total number of intermediate-redshift galaxies in both fields. C) The redshift distribution of the high-redshift sample in the HDF-N (bold) and HDF-S (normal). The distribution is normalized to the total number of high-redshift galaxies in the respective fields. D) The redshift distribution of all the high-redshift galaxies in the HDF-N and HDF-S combined. The distribution is normalized to the total number of high-redshift galaxies in both fields.

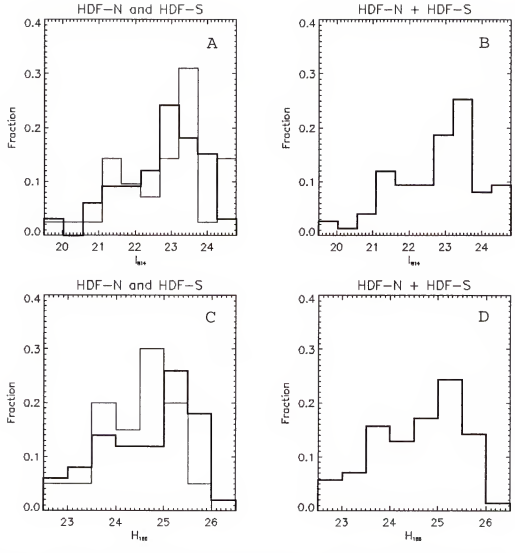

Figure 2–2: Magnitude distribution of galaxies in the HDFs North and South sample. A) The distribution of I_{814} magnitude of the intermediate-redshift sample in the HDF-N (bold) and HDF-S (normal). The distribution is normalized to the total number of intermediate-redshift galaxies in the respective fields. B) The distribution of the I_{814} magnitudes of all the intermediate-redshift galaxies in the HDF-N and HDF-S combined. The distribution is normalized to the total number of intermediate-redshift galaxies in both fields. C) The distribution of H_{160} magnitudes of the high-redshift sample in the HDF-N (bold) and HDF-S (normal). The distribution is normalized to the total number of high-redshift galaxies in the respective fields. D) The distribution of the H_{160} magnitudes of all the high-redshift galaxies in the HDF-N and HDF-S combined. The distribution is normalized to the total number of high-redshift galaxies in both fields.

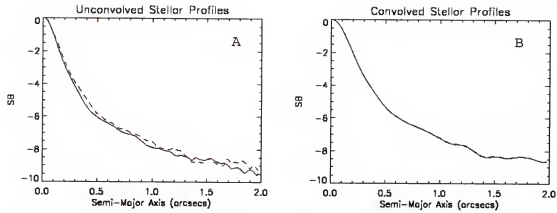

Figure 2–3: PSF matching of the HDF-S WFPC-2 field. A) The unconvolved stellar profiles of a star from the V_{606} (solid) and I_{814} (dashed) passbands of the HDF-S WFPC-2 field. B) The same stellar profiles after PSF matching was performed. The resulting FWHM is $\sim 0.''2$.

matching on the two stars that were the most isolated. In the HDF-S WFPC-2 image, I chose the brightest unsaturated and isolated star in the field. To filter out the high frequency noise from the PSF matching function, I applied a cosine bell taper since this produced the most realistic looking PSF, although it resulted in a broadened PSF due to the smoothing of the kernel. After generating the kernels, I used the FCONVOLVE task in the IRAF/STSDAS package to convolve the images with their respective kernels. The PSF matching process resulted in a FWHM of $\sim$ $0.''2$ in the HDF-S WFPC-2 field and $0.''3$ in the HDF-S NICMOS images. Figure 2-3 shows the profiles of the V_{606} (solid) and I_{814} (dashed) PSFs in the HDF-S WFPC-2 field before and after convolution. Figure 2-4 shows the profiles of the J_{110} (solid), H_{160} (dotted), and K_{222} (dashed) PSFs in the HDF-S NICMOS field before and after convolution. As an independent check on the PSF matching, I checked for color gradients in the stellar profile to verify that they were minor.

2.3 Surface Photometry

I performed detailed surface photometry on the sample of galaxies using the ELLIPSE task in the IRAF/STSDAS package. This task fits elliptical isophotes to the galaxies using the iterative scheme described in Jedrzejewski (1987). I entered inital guesses for the ellipse center (x,y), ellipticity (e), and position angle (ϕ) and

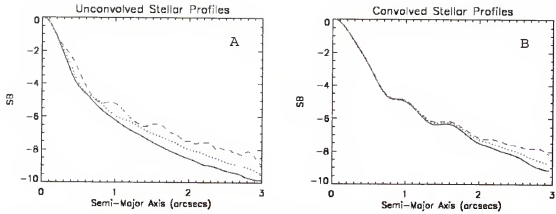

Figure 2–4: PSF matching of the HDF-S NICMOS field. A) The unconvolved stellar profiles of a star from the J_{110} (solid), H_{160} (dotted), and K_{222} (dashed) passbands of the HDF-S NICMOS field. B) The same stellar profiles after PSF matching was performed. The resulting FWHM is $\sim 0.''3$.

allowed the task to update these parameters following the iteration scheme. The errors in the azimuthally averaged intensity are obtained from the rms scatter of the intensity measurements along each fitted isophote. To generate color profiles, it was important that I kept the ellipses fixed between the different filters since positional displacement of the isophotes in the different filters may cause the color distribution of the galaxy to be artificially asymmetric. To ensure that the surface brightness profiles of the different passbands were generated using the same fitted ellipses, I combined the images taken in different passbands; fitted ellipses to the combined image; and then used the set of ellipses generated from the combined image as the input ellipses for "no-fit" mode on each individual image. Many of the galaxies, especially at high-redshifts, possessed nearby companions. To perform the fits only on the galaxy of interest, I masked out the companion. I then converted all fluxes to AB magnitudes (Oke and Gunn 1983) which is described by:

$$m(AB) = -2.5log(f_\nu) - 48.6 \tag{2.1}$$

Here, the monochromatic flux (f_ν) is expressed in terms of frequency and is in units of $ergs^{-1}cm^{-2}Hz^{-1}$.

2.4 Fitting Surface Brightness Profiles

From the elliptical isophotes, I produced azimuthally averaged radial surface brightness profiles. I produced profiles for the images taken in the I_{814} and H_{160} passbands for the intermediate and high-redshift samples respectively. At the respective redshifts of the galaxies, these images represent approximately their rest-frame B wavelengths. For the HDF-N images, I performed the surface brightness analysis on the PSF matched images. For the HDF-S images, I performed the analysis on the images before PSF matching was performed given that the resolution was better in those images.

I analyzed the resulting intensity distribution using the STSDAS task NFIT1D to perform χ^2 fitting to the surface brightness profiles. Locally, the profiles would be fit with the sum of an $r^{1/4}$ bulge (de Vaucouleurs 1948) and an exponential disk (Freeman 1970) profile. However, the scale lengths of most of the galaxies (especially at high-redshifts) were so small and severely affected by PSF smearing that it was difficult to obtain reliable fits using these profiles. Thus, I decided to fit the radial light profiles with a generalized exponential (Sérsic (1968)):

$$S(r) = S(e)exp[-(1.9992n - 0.3271)((r/R(e))^{1/n} - 1)] \tag{2.2}$$

where *R(e)* is the half-light radius, *S(e)* is the flux at *R(e)*, $S(r)$ is the surface brightness at r, and n is the Sérsic index which tells us about the degree of flattening in the profile ($n = 1$ recovers the exponential disk profile and $n = 4$ recovers the $r^{1/4}$ law). Trujillo et al. (2001) have applied an analytic approach to study the effects of the PSF on the Sérsic profiles. They found that, of the free parameters in the Sérsic profile, the one that is affected most by the PSF is n which is smaller in the observed profile than in the actual profile. Furthermore, the higher the original value of n is, the more it will be affected by the PSF. At the faint magnitudes and small scale lengths of typical high-redshift galaxies in the HDFs, I showed that the PSF can potentially flatten both an exponential

and an $r^{1/4}$ profile into a Sérsic profile with $n < 1$. It then becomes challenging to distinguish between galaxies having exponential profiles from those having de Vaucouleurs profiles. Section 2.5 explains my attempts to understand the effects of the PSF on the surface brightness profiles to more accurately classify morphologies.

2.5 Creating Model Galaxies to Account for PSF Effects

To account for the effects of the PSF on the data, I created model galaxies and convolved them with the PSF to match the resolution of the data. I created 10 galaxies with exponential disk profiles ($n = 1$) and 10 with $r^{1/4}$ ($n = 4$) bulge profiles with varying half-light radii. These galaxies possessed I_{814} magnitudes = 21, 22, 23, and 24 to simulate the intermediate-redshift sample; and H_{160} magnitudes = 23 and 24 to simulate the high-redshift sample. Since the HDF-N WFPC-2 and NICMOS images have all been degraded to match the resolution of the H_{160} passband, I convolved the model galaxies with an isolated, unsaturated star taken from this passband. Given that the surface brightness profiles of the galaxies in the HDF-S field were generated using the I_{814} and H_{160} images before PSF matching was performed, the model galaxies are convolved with a star on these images to simulate the intermediate and high-redshift galaxies respectively. I performed the convolution using the IRAF task FCONVOLVE which takes the fourier transform of the model galaxy and the PSF (normalized to conserve flux), multiplies them together, and then takes the inverse transform of the product to produce the final convolved galaxy. I then added the model galaxies onto blank areas of the sky in the HDFs North and South I_{814} and H_{160} images to simulate the intermediate-redshift and high-redshift sample respectively. By doing so, I include the contribution of the background noise which exists in the image. However, I chose to neglect the poisson noise from the galaxies themselves since it is negligible compared to the background noise.

I then generated surface brightness profiles and fit Sérsic profiles to the convolved disk and spheroid galaxies to determine the degree of flattening due to the PSF. Tables 2-2 and 2-3 lists the half-light radii and the Sérsic indices of the convolved model galaxies with I_{814} magnitudes= 21, 22, 23, and 24 in the HDF-N and HDF-S respectively. Tables 2-4 and 2-5 lists the half-light radii and the Sérsic indices of the convolved model galaxies with H_{160} magnitudes= 23 and 24 in the HDF-N and HDF-S respectively. The tables show that, after convolution with the PSF, the profiles of all the galaxies are significantly flattened, i.e., their Sérsic index, n, decreased significantly from the original profile (recall that $n = 1$ for disks and $n = 4$ for spheroids). In fact, Tables 2-2 and 2-3 show that after convolution with the PSF, the Sérsic indices of the mock intermediate-redshift galaxies in the HDF-N originally possessing an $r^{1/4}$ profile can drop all the way to a value of 1 which is indicative of an exponential profile. Tables 2-4 and 2-5 reveal an even more drastic drop in Sérsic indices of the mock high-redshift galaxies after they had been convolved with the PSF of the HDF-N. At the small scale lengths and faint magnitudes typical of the high-redshift galaxies in the sample, the Sérsic indices of the model spheroids drop to 1 and below rendering them almost indistinguishable from the model disks. Furthermore, the smaller the galaxy is, the more the value of n decreases for both the disk and bulge models. Consequently it would be very difficult to determine from the convolved profile whether it originally possessed an exponential or an $r^{1/4}$ profile.

Fortunately, trends exist and make it possible to distinguish between the two types of galaxies even after they have been significantly flattened by the PSF. Although at a given radius and magnitude both profiles are severely smoothed out, n for the spheroid is always higher than n for the disk; i.e., the disk has a more flattened profile. For example in the HDF-N, at $I_{814} = 21$ and half-light radius of approximately $0.''84$, n for the spheroid is 1.736 whereas n for the disk

is 0.789 (Table 2-2) which is significantly lower. This trend occurs at all radii and magnitudes. Thus, although the surface brightness profiles of the galaxies in the HDF are significantly affected by the PSF, it is still possible to broadly classify galaxies morphologically by comparing the value of n and the half-light radii of these galaxies at a given magnitude with those of our model galaxies. However, caution must be taken when using this method to classify the morphologies of galaxies with half-light radii less than $0.12''$ since it would be pushing the resolution limit of the instrument and, consequently, the results would not be reliable. Fortunately, there are no galaxies in the sample where this applies. It is also important to note that, for galaxies in the high-redshift sample, I can only reliably classify the morphologies if they possesss H_{160} magnitudes < 24.5. At fainter magnitudes, the Sérsic indices of a disk and spheroid at a given radius is within the range of the scatter. One must keep in mind also that this galaxy classification scheme is not intended to be used to classify galaxies on a case by case basis, but rather to obtain statistics about the galaxy population as a whole.

2.6 Generating Color Profiles and Determining the Gradients

I determined the color profiles of the galaxies by subtracting the surface brightness profile of one passband from the surface brightness profile of the adjacent passband. In the HDF-N, I generated $(B_{450} - V_{606})$ and $(V_{606} - I_{814})$ color profiles for the intermediate-redshift sample; and $(I_{814} - J_{110})$ and $(J_{110} - H_{160})$ color profiles for the high-redshift sample to probe their rest-frame $(UV_{218} - U_{300})_0$ and $(U_{300} - B_{300})_0$ profiles. In the HDF-S, I generated $(V_{606} - I_{814})$ color profiles for the low-redshift and intermediate-redshift sample; and $(J_{110} - H_{160})$ and $(H_{160} - K_{222})$ color profiles for the high-redshift sample to probe their rest-frame $(U_{300} - B_{300})_0$ and $(B_{450} - V_{606})_0$ color profiles. I then applied K-corrections described in Section 2.7 to transform them to their rest-frame colors. The K-corrections applied are minimal since I have chosen to work with passbands that closely map to their

Table 2–2: Half-light radii and Sérsic indices of convolved model disks ($n = 1$) and spheroids ($n = 4$) in the I_{814} passband in the HDF-N

#	Profile	R_{21}[a]	n_{21}[b]	R_{22}[c]	n_{22}[d]	R_{23}[e]	n_{23}[f]	R_{24}[g]	n_{24}[h]
1	Disk	1.012	0.781	0.984	0.790	0.928	0.771	0.840	0.805
2	Disk	0.956	0.816	0.956	0.800	1.024	0.789	0.900	0.630
3	Disk	0.844	0.789	0.816	0.750	0.772	0.689	0.696	0.582
4	Disk	0.800	0.793	0.800	0.769	0.836	0.746	0.768	0.676
5	Disk	0.712	0.785	0.712	0.765	0.756	0.747	0.720	0.732
6	Disk	0.628	0.773	0.628	0.744	0.596	0.714	0.600	0.681
7	Disk	0.556	0.740	0.552	0.713	0.536	0.690	0.508	0.690
8	Disk	0.480	0.727	0.472	0.696	0.460	0.671	0.440	0.643
9	Disk	0.408	0.692	0.400	0.678	0.392	0.655	0.380	0.631
10	Disk	0.308	0.707	0.304	0.694	0.300	0.668	0.296	0.630
11	Spheroid	0.804	1.651	0.764	1.366	0.704	1.094	0.604	0.910
12	Spheroid	0.832	1.736	0.804	1.435	0.676	1.209	0.568	1.013
13	Spheroid	0.748	1.603	0.692	1.336	0.596	1.127	0.624	0.987
14	Spheroid	0.704	1.572	0.656	1.360	0.596	1.151	0.440	0.910
15	Spheroid	0.604	1.521	0.560	1.337	0.496	1.111	0.432	0.906
16	Spheroid	0.564	1.517	0.548	1.346	0.508	1.115	0.452	0.914
17	Spheroid	0.508	1.480	0.504	1.325	0.492	1.114	0.456	0.913
18	Spheroid	0.436	1.368	0.428	1.266	0.384	1.089	0.352	0.917
19	Spheroid	0.388	1.320	0.392	1.227	0.388	1.108	0.400	0.984
20	Spheroid	0.300	1.088	0.300	1.063	0.296	0.992	0.304	0.870

[a] Half-light radius in arcseconds for $I_{814} = 21$.

[b] Sérsic index for $I_{814} = 21$.

[c] Half-light radius in arcseconds for $I_{814} = 22$.

[d] Sérsic index for $I_{814} = 22$.

[e] Half-light radius in arcseconds for $I_{814} = 23$.

[f] Sérsic index for $I_{814} = 23$.

[g] Half-light radius in arcseconds for $I_{814} = 24$.

[h] Sérsic index for $I_{814} = 24$.

Table 2–3: Half-light radii and Sérsic indices of convolved model disks ($n = 1$) and spheroids ($n = 4$) in the H_{160} passband of the HDF-N

#	Profile	R_{23}[a]	n_{23}[b]	R_{24}[c]	n_{24}[d]
1	Disk	0.488	0.754	0.288	0.605
2	Disk	0.432	0.672	0.384	0.623
3	Disk	0.372	0.635	0.364	0.630
4	Disk	0.292	0.595	0.300	0.591
5	Disk	0.252	0.593	0.248	0.582
6	Disk	0.232	0.590	0.228	0.554
7	Disk	0.232	0.622	0.236	0.588
8	Disk	0.220	0.618	0.208	0.599
9	Disk	0.200	0.615	0.208	0.609
10	Disk	0.188	0.622	0.196	0.592
11	Spheroid	0.416	0.848	0.356	0.716
12	Spheroid	0.392	0.892	0.368	0.804
13	Spheroid	0.364	0.904	0.332	0.771
14	Spheroid	0.296	0.794	0.304	0.783
15	Spheroid	0.272	0.785	0.260	0.715
16	Spheroid	0.248	0.760	0.240	0.731
17	Spheroid	0.240	0.744	0.236	0.690
18	Spheroid	0.224	0.715	0.240	0.686
19	Spheroid	0.208	0.690	0.196	0.636
20	Spheroid	0.204	0.687	0.212	0.681

[a] Half-light radius in arcseconds for $H_{160} = 23$.

[b] Sérsic index for $H_{160} = 23$.

[c] Half-light radius in arcseconds for $H_{160} = 24$.

[d] Sérsic index for $H_{160} = 24$.

Table 2–4: Half-light radii and Sérsic indices of convolved model disks ($n = 1$) and spheroids ($n = 4$) in the I_{814} passband in the HDF-S

#	Profile	R_{21}[a]	n_{21}[b]	R_{22}[c]	n_{22}[d]	R_{23}[e]	n_{23}[f]	R_{24}[g]	n_{24}[h]
1	Disk	0.959	0.850	0.872	0.870	0.724	0.840	0.681	0.899
2	Disk	0.851	0.851	0.792	0.830	0.720	0.817	0.720	0.894
3	Disk	0.792	0.857	0.776	0.858	0.621	0.859	0.613	0.960
4	Disk	0.732	0.853	0.689	0.849	0.557	0.875	0.545	0.977
5	Disk	0.653	0.838	0.629	0.824	0.549	0.839	0.537	0.933
6	Disk	0.593	0.841	0.545	0.825	0.549	0.841	0.434	0.855
7	Disk	0.513	0.827	0.497	0.798	0.462	0.784	0.430	0.800
8	Disk	0.438	0.814	0.434	0.768	0.418	0.759	0.378	0.757
9	Disk	0.366	0.805	0.358	0.763	0.350	0.721	0.338	0.591
10	Disk	0.255	0.791	0.251	0.750	0.247	0.715	0.251	0.697
11	Spheroid	0.864	1.723	0.629	1.386	0.597	1.348	0.521	1.204
12	Spheroid	0.792	1.794	0.597	1.477	0.454	1.189	0.450	1.370
13	Spheroid	0.780	1.748	0.736	1.497	0.386	1.116	0.354	1.107
14	Spheroid	0.680	1.891	0.565	1.496	0.414	1.200	0.410	1.312
15	Spheroid	0.657	1.806	0.549	1.447	0.394	1.177	0.354	1.128
16	Spheroid	0.605	1.813	0.541	1.540	0.509	1.329	0.306	0.912
17	Spheroid	0.557	1.847	0.458	1.522	0.382	1.265	0.322	1.106
18	Spheroid	0.466	1.849	0.342	1.502	0.326	1.296	0.287	1.058
19	Spheroid	0.386	1.811	0.350	1.523	0.287	1.171	0.287	0.921
20	Spheroid	0.299	1.628	0.291	1.488	0.255	1.230	0.235	1.026

[a] Half-light radius in arcseconds for $I_{814} = 21$.

[b] Sérsic index for $I_{814} = 21$.

[c] Half-light radius in arcseconds for $I_{814} = 22$.

[d] Sérsic index for $I_{814} = 22$.

[e] Half-light radius in arcseconds for $I_{814} = 23$.

[f] Sérsic index for $I_{814} = 23$.

[g] Half-light radius in arcseconds for $I_{814} = 24$.

[h] Sérsic index for $I_{814} = 24$.

Table 2–5: Half-light radii and Sérsic indices of convolved model disks ($n = 1$) and spheroids ($n = 4$) in the H_{160} passband of the HDF-S

#	Profile	R_{23}[a]	n_{23}[b]	R_{24}[c]	n_{24}[d]
1	Disk	0.615	0.742	0.600	0.791
2	Disk	0.570	0.829	0.555	0.797
3	Disk	0.480	0.704	0.435	0.695
4	Disk	0.450	0.716	0.457	0.717
5	Disk	0.383	0.716	0.375	0.650
6	Disk	0.330	0.755	0.322	0.734
7	Disk	0.300	0.702	0.300	0.669
8	Disk	0.262	0.725	0.255	0.655
9	Disk	0.240	0.773	0.240	0.706
10	Disk	0.218	0.802	0.218	0.751
11	Spheroid	0.465	1.058	0.375	0.852
12	Spheroid	0.442	1.144	0.360	0.888
13	Spheroid	0.285	1.093	0.397	0.942
14	Spheroid	0.345	0.960	0.285	0.785
15	Spheroid	0.323	0.965	0.270	0.793
16	Spheroid	0.315	1.009	0.278	0.846
17	Spheroid	0.293	0.994	0.278	0.919
18	Spheroid	0.263	0.934	0.240	0.814
19	Spheroid	0.240	0.894	0.248	0.918
20	Spheroid	0.218	0.873	0.225	0.844

[a] Half-light radius in arcseconds for $H_{160} = 23$.

[b] Sérsic index for $H_{160} = 23$.

[c] Half-light radius in arcseconds for $H_{160} = 24$.

[d] Sérsic index for $H_{160} = 24$.

rest-frame wavelengths. I then performed a weighted least-squares fit to the profile. For the HDF-N, I started the fit 0.″14 out from the center of the profile since the color differences near the center might reflect slight differences in the PSF between the two passbands rather than indicate true color changes in the galaxy. For the HDF-S, I used all the isophotes since the PSF matching was very good in the center. From the fits, I was able to obtain the value of the color gradient.

The main source of error in this procedure was the uncertainty in the determination of the local sky background values. The global sky background subtraction might be adequate for the larger and brighter galaxies in the intermediate-redshift sample, but for the smaller and fainter galaxies in the high-redshift sample, there could be residuals in the background that could significantly change the value and even the sign of the color gradient if the effect is huge. I determined the value of the local sky background by extending the elliptical isophotes out past five scale lengths in 0.″12 increments taking care to mask out nearby objects. I then adopted the value of the background as the typical value of the flux level in the outermost isophotes. From this method, I found that in general there had been an overestimation in the global background value in the reduced images used for this study. The uncertainties due to the background subtraction are discussed in Section 4.2 and were added in quadrature to the errors in the color gradients.

The errors in the median value of the color gradients reported for each sample set were determined by using a bootstrapping technique. In this technique, the bootstrap samples are randomly drawn from the population of the original sample with the same sample size. I repeatedly (10,000 times) caculated the medians of the bootstrap sample and then interpreted the standard deviation in the medians of these bootstrap samples as the standard error of the original sample median.

2.7 K-corrections

When two galaxies are observed at different distances with the same intrinsic brightness through the same passband, two different magnitudes will be measured not only because of the inverse square law, but also because their spectral energy distributions (SED) will be shifted towards longer wavelengths and also "stretched" by a factor of $(1+z)$ due to the expansion of the universe. To correct for this effect and to convert the color profiles to their rest-frame values, K-corrections must be applied to the results. I use the definition of the K-correction from Oke and Sandage (1968):

$$K_i(z) = 2.5log_{10}(1+z)+2.5log_{10}\left[\int S_i(\lambda)F(\lambda)d(\lambda) \Big/ \int S_i(\lambda)F(\lambda/1+z)d(\lambda)\right] \quad (2.3)$$

where $S_i(\lambda)$ is the sensitivity function of the detector i, $F(\lambda)$ is the observed energy flux density, $F(\lambda/1+z)$ is the energy flux density of the galaxy at rest, $d(\lambda)$ is the bandwidth of the detector i, and $K_i(z)$ is the K-correction of the galaxy observed through detector i at redshift z. The first term of the correction is due to the "stretching" of the passband whereas the second term represents the shifting of the SED to longer wavelengths.

Since K-corrections do not currently exist for the NICMOS passbands, I generated my own set by using the SEDs from Devriendt at al. (1999). They used the STARDUST model to produce SEDs for galaxies ranging from local spirals, starbursts, luminous infrared galaxies (LIRGS), and ultraluminous infrared galaxies (ULIRGS) extending from the far-UV to sub-mm wavelengths. Their SEDs also included the effects of internal extinction and emission of dust in the galaxies. I obtained the throughputs for the WFPC2 and NICMOS passbands by anonymous ftp from the Space Telescope Science Insitute and accessed these tables using the IRAF task CALCBAND. I then generated K-corrections using the SEDs for the model galaxies from Devriendt at al. (1999). The K-corrections

for the UV_{218} through the K_{222} passbands are derived for redshifts with rest-frame wavelengths in the observed passband greater than 1300Å up to redshifts of 4.0. I used linear interpolation to increment the redshifts by 0.001. I then used the K-corrections to generate colors ranging from $(UV_{218} - U_{300})$ up to $(H_{160} - K_{222})$ for the model galaxies at redshifts up to 4.0. To find the appropriate K-correction for the observed colors, I matched the redshift and the observed colors of my sample galaxies with that of the model galaxies. The colors of the galaxies were approximated by taking the average of all the colors from the isophotes.

CHAPTER 3
RESULTS

In this section, I present the results from the surface brightness and color profile analysis. I present the profile classification of intermediate and high-redshift galaxies based on the results from the surface brightness profiles, galaxy models discussed in Section 2.5, and visual inspection. At intermediate-redshifts, I_{814} surface brightness profiles were generated while, at high-redshifts, H_{160} surface brightness profiles were generated. At the respective redshifts, these passbands correspond to the rest-frame B band. Since the study focuses on comparing the properties of intermediate and high-redshift galaxies, I do not generate surface brightness profiles for the low-redshift sample.

I include low-redshift galaxies in this study solely to compare the results of the rest-frame $(B_{450} - V_{606})_0$ color gradients with that of the high-redshift sample. For galaxies in the HDF-N, I use the $(B_{450} - V_{606})$ color profiles of the intermediate-redshift sample and the $(I_{814} - J_{110})$ color profiles of the LBGs to compare how the rest-frame $(UV_{218} - U_{300})_0$ color gradients change with time. For both the HDF-N and the HDF-S, I use the $(V_{606} - I_{814})$ color profiles of the intermediate-redshift sample and the $(J_{110} - H_{160})$ color profiles of the LBGs to understand how the rest-frame $(U_{300} - B_{450})_0$ color gradients changes with time. Since the K_{222} band is available for the HDF-S, I can also study the temporal evolution of the rest-frame $(B_{450} - V_{606})_0$ color gradients using the $(H_{160} - K_{222})$ profiles for the high-redshift galaxies and the $(V_{606} - I_{814})$ profiles of the low-redshift galaxies.

Tables 3-1 and 3-2 summarizes the statistics from the surface brightness and color profile analysis for the 33 galaxies in the intermediate-redshift and 50 galaxies in the high-redshift sample respectively for the HDF-N. Tables 3-3, 3-4,

and 3-5 lists the statistics for the 20 galaxies in the low-redshift sample, 42 galaxies in the intermediate-redshift sample, and 20 galaxies in the high-redshift sample respectively for the HDF-S.

3.1 Surface Brightness Profiles

Ideally galaxies that possess exponential profiles would have a Sérsic index of 1 whereas galaxies that possess a de Vaucouleurs profile would have a Sérsic index of 4. However, I have demonstrated in Section 3.1 that when classifying morphologies based on the Sérsic indices, it is critical to take into account the role of the PSF since (in many cases) the PSF can smooth what was originally an $r^{1/4}$ profile to one with $n < 1$. To more accurately classify morphologies, I generated model galaxies discussed in Section 2.5, convolved them with the PSF of the image, and compared their Sérsic indices after convolution with the Sérsic indices of the galaxies in the sample.

I generated ($r_{1/2} - n$) (half-light radii versus Sérsic indices) plots of the galaxy models and the galaxies in the sample to classify the morphologies of all the galaxies in the intermediate-redshift bin and those with $H_{160} \leq 24.5$ in the high-redshift bin. The galaxies whose Sérsic indices fall above the locus for the model spheroids were classified as possessing $r^{1/4}$ profiles since this would indicate that they possess profiles that are steeper than the models; whereas those whose Sérsic indices fall below the locus for the model disks were classified as possessing exponential profiles since this would indicate that they possess profiles that are shallower than the models. For the galaxies that have Sérsic indices with values that fall in between the locus of the model spheroids and disks, I placed an acceptance limit of 5 σ. If the values of the Sérsic indices were less than 5 σ away from the locus of spheroids, I classified them as possessing $r^{1/4}$ profiles; if they were less than 5 σ from the locus of the disks, I classified them as possessing exponential

Table 3–1: $0.5 \leq z \leq 1.2$ galaxies in the HDF-N

ID[a]	z^b	$M_I{}^c$	$n(I_{814})^d$	Class[e]	$R(I_{814})^f$	$\Delta(UV_{218}-U_{300})_0{}^g$ $\Delta\log(r)$	$\Delta(U_{300}-B_{450})_0{}^h$ $\Delta\log(r)$
(1)	(2)	(3)	(4)	(5)	(6)	(7)	(8)
2-353	0.609	23.67	0.6998 ± 0.0008	Exp	1.867	0.187 ± 0.077	0.008 ± 0.022
2-251	0.962	21.32	2.4128 ± 0.0020	deV	3.056	0.818 ± 0.024	0.990 ± 0.013
2-661	0.819	23.22	0.7738 ± 0.0004	Exp	4.574	−0.123 ± 0.018	−0.011 ± 0.009
2-514	0.752	21.84	0.9400 ± 0.0003	Int	2.711	−0.036 ± 0.014	0.002 ± 0.012
2-950	0.517	23.60	0.6345 ± 0.0006	Exp	3.004	−0.086 ± 0.019	−0.022 ± 0.005
2-809	0.498	23.44	...	Irr	2.368	−0.288 ± 0.052	−0.060 ± 0.016
2-702	0.559	23.09	0.7001 ± 0.0012	Exp	2.995	0.038 ± 0.009	−0.042 ± 0.005
2-652	0.557	21.09	0.8540 ± 0.0004	Int	3.716	0.395 ± 0.008	0.150 ± 0.003
2-1023	0.564	23.02	0.6237 ± 0.0005	Exp	4.110	−0.045 ± 0.011	0.048 ± 0.013
1-105	0.846	24.04	0.8923 ± 0.0014	deV	1.663	−0.640 ± 0.054	0.338 ± 0.040
2-1018	0.559	23.75	1.0071 ± 0.0011	deV	3.413	−0.200 ± 0.039	−0.182 ± 0.115
2-860	0.851	22.56	0.6221 ± 0.0002	Exp	3.406	−0.304 ± 0.033	−0.297 ± 0.006
2-982	1.148	22.81	0.8546 ± 0.0015	Int	5.210	−0.207 ± 0.016	−0.315 ± 0.086
2-402	0.557	20.97	0.8346 ± 0.0005	Exp	4.530	−0.137 ± 0.005	−0.132 ± 0.005
4-493	0.849	21.70	1.9410 ± 0.0014	deV	2.749	−0.436 ± 0.058	−0.186 ± 0.007
4-89	0.681	24.04	0.6743 ± 0.0008	Exp	3.080	0.098 ± 0.022	−0.070 ± 0.010
4-132	0.511	24.10	0.5805 ± 0.0009	Exp	2.204	0.192 ± 0.029	0.103 ± 0.015
3-430	0.875	23.52	0.6693 ± 0.0016	Exp	3.886	−0.226 ± 0.152	−0.315 ± 0.010
4-950	0.609	22.27	0.8792 ± 0.0007	Int	3.530	−0.125 ± 0.013	−0.135 ± 0.010
4-221	0.952	22.94	0.7173 ± 0.0012	Int	3.877	0.141 ± 0.012	0.248 ± 0.010
3-350	0.642	20.97	0.8820 ± 0.0005	Int	4.224	−0.457 ± 0.005	−0.318 ± 0.004
3-404	0.520	23.58	0.7805 ± 0.0011	Exp	2.520	0.173 ± 0.030	0.182 ± 0.009
4-928	1.015	22.32	1.4232 ± 0.0010	deV	2.327	−0.316 ± 0.028	−0.553 ± 0.019
3-610	0.518	19.95	2.3243 ± 0.0152	deV	7.975	−0.415 ± 0.009	−0.271 ± 0.001
			0.8263 ± 0.0020	Exp			
3-551	0.560	22.95	0.5967 ± 0.0004	Exp	2.997	0.095 ± 0.013	0.086 ± 0.005
3-378	1.225	24.06	...	Irr	5.564	−0.269 ± 0.009	−0.429 ± 0.014
4-565	0.752	22.74	1.1104 ± 0.0014	deV	2.149	0.076 ± 0.014	0.191 ± 0.012
3-486	0.790	21.99	1.1928 ± 0.0009	deV	3.467	−0.673 ± 0.010	−0.538 ± 0.006
4-727	1.242	23.18	1.0207 ± 0.0012	deV	2.116	0.085 ± 0.012	0.275 ± 0.010
4-775	1.010	22.50	0.9882 ± 0.0009	Int	4.126	−0.323 ± 0.024	−0.317 ± 0.012
4-850	0.961	24.61	0.6211 ± 0.0013	Exp	2.460	0.098 ± 0.037	0.096 ± 0.024
4-260	0.962	22.88	0.8264 ± 0.0013	Int	6.500	−0.292 ± 0.003	−0.213 ± 0.003
3-321	0.680	21.43	1.9040 ± 0.0027	deV	3.311	−0.035 ± 0.027	−0.198 ± 0.004

[a] IDs are from Williams et al. 1996.

[b] Redshifts are from Cohen et al. 1996 and Zepf et al. 1997.

[c] F814W AB mag within ~ 26 mag arcsec^{-2}.

[d] Sérsic index in rest-frame B.

[e] (deV) de Vaucouleurs, (Exp) exponential, (Int) intermediate, (Irr) irregular.

[f] I_{814} half-light radius in kiloparsecs.

[g] Rest-frame $(UV_{218} - U_{300})_0$ color gradient within $R_{1/2} \sim 4$ kpc.

[h] Rest-frame $(U_{300} - B_{450})_0$ color gradient within $R_{1/2} \sim 4$ kpc.

Table 3–2: $2.0 \leq z \leq 3.5$ galaxies in the HDF-N

ID[a]	z^b	$M_H{}^c$	n(H_{160})[d]	Class[e]	R(H_{160})[f]	$\Delta(UV_{218}-U_{300})_0{}^g$ $\Delta\log(r)$	$\Delta(U_{300}-B_{450})_0{}^h$ $\Delta\log(r)$
(1)	(2)	(3)	(4)	(5)	(6)	(7)	(8)
2-82	2.267	23.81	0.645 ± 0.002	Exp	2.573	0.463 ± 0.211	−0.232 ± 0.144
2-239	2.427	24.58	0.974 ± 0.004	...	2.361	0.289 ± 0.183	0.101 ± 0.138
2-454	2.009	23.55	0.629 ± 0.001	Exp	2.488	0.204 ± 0.179	−0.416 ± 0.131
2-449	2.005	22.56	0.874 ± 0.002	deV	2.223	0.486 ± 0.101	−0.210 ± 0.071
2-585.1	1.980	24.39	0.794 ± 0.004	deV	1.905	−0.080 ± 0.062	−0.331 ± 0.044
2-585.11	1.980	22.52	0.766 ± 0.002	Exp	3.917	0.065 ± 0.087	−0.346 ± 0.059
2-76	3.160	25.37	...	...	1.826	−0.185 ± 0.263	0.062 ± 0.192
2-525	2.237	23.63	0.840 ± 0.003	deV	2.787	0.406 ± 0.224	−0.212 ± 0.151
2-901	3.181	24.19	0.735 ± 0.002	deV	2.206	0.162 ± 0.208	0.191 ± 0.154
2-565	3.162	24.60	...	...	1.849	0.361 ± 0.468	−0.869 ± 0.318
2-903	2.233	24.04	0.706 ± 0.001	deV	1.694	0.419 ± 0.226	−0.642 ± 0.150
2-637	3.368	24.98	0.688 ± 0.004	...	1.249	0.787 ± 0.651	−0.082 ± 0.449
1-54	2.929	23.10	...	Irr	2.382	−0.181 ± 0.084	−0.078 ± 0.055
2-643	2.991	24.41	...	Irr	2.075	0.590 ± 0.217	0.037 ± 0.132
2-591	2.489	24.04	0.787 ± 0.002	deV	1.557	0.179 ± 0.189	0.103 ± 0.137
4-639	2.591	24.66	0.764 ± 0.003	...	1.569	0.536 ± 0.261	−0.538 ± 0.217
4-52	2.931	23.58	...	Irr	2.995	−0.292 ± 0.128	−0.365 ± 0.092
3-118	2.232	23.52	0.865 ± 0.002	deV	1.615	0.322 ± 0.241	−0.309 ± 0.175
3-243	3.233	25.17	0.769 ± 0.006	...	1.217	0.466 ± 0.226	−0.073 ± 0.154
4-445	2.500	22.56	0.913 ± 0.003	deV	2.183	−0.004 ± 0.148	−0.109 ± 0.102
4-289	2.969	25.63	...	...	1.615	0.617 ± 0.350	−0.914 ± 0.288
4-497	2.800	25.15	0.709 ± 0.004	...	1.465	−0.907 ± 0.595	1.348 ± 0.435
4-555.12	2.803	23.12	0.960 ± 0.004	deV	1.962	0.375 ± 0.083	−0.085 ± 0.054
4-555.11	2.803	23.20	1.465 ± 0.006	deV	3.179	0.096 ± 0.066	−0.081 ± 0.045
4-363	2.980	25.06	...	...	1.735	1.034 ± 0.269	−1.983 ± 0.239
2-890	2.305	25.06	0.758 ± 0.003	...	1.840	0.438 ± 0.476	−0.716 ± 0.300
2-949	2.579	25.04	0.752 ± 0.003	...	1.698	0.364 ± 0.630	−0.646 ± 0.425
2-746	3.074	26.25	...	...	1.986	0.402 ± 0.491	0.202 ± 0.278
2-313	3.417	25.37	0.783 ± 0.004	...	1.313	0.374 ± 0.503	0.134 ± 0.326
2-122	3.066	25.78	0.505 ± 0.002	...	1.333	−0.077 ± 0.582	0.615 ± 0.417
2-131	3.184	24.89	...	...	1.798	0.351 ± 0.292	−0.529 ± 0.163
3-675	3.531	25.31	0.451 ± 0.002	...	1.717	−0.013 ± 0.433	−0.092 ± 0.281
3-748	2.521	25.26	0.790 ± 0.006	...	1.528	−0.209 ± 0.593	1.374 ± 0.409
4-83	2.930	25.63	...	...	1.719	0.248 ± 0.491	0.057 ± 0.305
4-245	3.155	24.73	0.767 ± 0.004	...	2.813	−0.429 ± 0.754	−0.441 ± 0.527
3-813	3.149	25.77	0.827 ± 0.009	...	1.515	0.372 ± 0.822	0.484 ± 0.491
3-875	2.330	23.17	0.510 ± 0.001	Exp	2.974	0.044 ± 0.112	−0.283 ± 0.073
3-916	2.159	23.85	0.808 ± 0.003	deV	1.860	−0.054 ± 0.380	0.267 ± 0.285
4-421	2.119	25.67	0.772 ± 0.007	...	1.524	0.571 ± 0.469	−0.817 ± 0.326
2-59	2.255	27.37	0.574 ± 0.005	...	0.989	1.168 ± 1.303	−1.773 ± 1.009
2-755	1.970	25.17	...	...	2.493	0.352 ± 0.225	−0.676 ± 0.145
2-180	2.035	25.77	0.680 ± 0.004	...	2.061	1.017 ± 0.416	−0.807 ± 0.196
2-693	2.012	23.79	...	Irr	2.275	0.115 ± 0.111	−0.252 ± 0.082
2-321	2.503	24.49	0.644 ± 0.002	deV	1.428	0.417 ± 0.559	−0.061 ± 0.327
2-790	2.025	25.47	0.622 ± 0.003	...	1.718	0.822 ± 0.722	0.584 ± 0.379
2-496	2.936	25.81	0.728 ± 0.004	...	1.276	−0.381 ± 1.027	0.727 ± 0.735
2-973	2.775	25.90	...	...	1.668	−0.191 ± 0.656	0.497 ± 0.456
2-392	2.206	25.38	...	...	1.880	0.464 ± 0.161	−1.223 ± 0.154
2-347	2.307	25.30	0.525 ± 0.003	...	1.529	0.970 ± 0.493	−1.304 ± 0.340
1-67	2.124	25.56	0.571 ± 0.004	...	1.576	−0.456 ± 0.580	0.678 ± 0.407

[a] IDs are from Williams et al. 1996.

[b] Redshifts are from Steidel et al. 1996, Lowenthal et al. 1997, and Budavári et al. 2000.

[c] F160W AB mag within ~ 26 mag arcsec^{-2}.

[d] Sérsic index in rest-frame B.

[e] (deV) de Vaucouleurs, (Exp) exponential, (Int) intermediate, (Irr) irregular.

[f] H_{160} half-light radius in kiloparsecs.

[g] Rest-frame $(UV_{218} - U_{300})_0$ color gradient within ~ 28 mag arcsec^{-2}.

[h] Rest-frame $(U_{300} - B_{450})_0$ color gradient within ~ 28 mag arcsec^{-2}.

Table 3–3: $0 < z < 0.5$ galaxies in the HDF-S

ID[a]	z^b	$M_I{}^c$	$R(I_{814})^d$	$\frac{\Delta(B_{450}-V_{606})_0{}^e}{\Delta\log(r)}$
(1)	(2)	(3)	(4)	(5)
2305	0.468	22.88	3.586	-0.033 ± 0.008
2360	0.423	23.48	2.313	-0.146 ± 0.015
1942	0.423	23.26	4.299	0.015 ± 0.007
1754	0.468	20.05	3.667	-0.144 ± 0.006
1922	0.492	21.83	0.684	-0.046 ± 0.004
1753	0.445	22.15	3.776	-0.013 ± 0.003
10427	0.492	20.17	3.069	-0.087 ± 0.003
1285	0.296	21.67	1.763	-0.003 ± 0.003
1187	0.492	22.63	0.685	-0.011 ± 0.008
926	0.468	22.10	1.925	0.070 ± 0.006
956	0.492	23.09	3.297	-0.092 ± 0.006
617	0.382	20.63	3.891	-0.131 ± 0.006
667	0.268	21.16	3.132	-0.037 ± 0.003
476	0.423	22.33	3.797	-0.072 ± 0.005
478	0.492	23.11	2.592	-0.064 ± 0.006
431	0.079	22.64	0.199	0.020 ± 0.005
10015	0.492	23.51	4.541	-0.009 ± 0.014
254	0.445	22.13	1.246	0.031 ± 0.004
108	0.382	22.91	0.603	-0.013 ± 0.006
87	0.468	21.26	4.761	-0.086 ± 0.004

[a] IDs are from Casertano et al. 2000.

[b] Redshifts are from Chen et al. 1998 and Yahata et al. 2000.

[c] F814W AB mag within ~ 26 mag arcsec^{-2}.

[d] I_{814} half-light radius in kiloparsecs.

[e] Rest-frame $(B_{450} - V_{606})_0$ color gradient within $R_{1/2} \sim 4$ kpc.

profiles; and if they were more than 5 σ away from either loci, I classified them as possessing intermediate profiles.

There were a few galaxies that possessed Sérsic indices with less than 5 σ deviations from both loci. In these cases, I classified them according to the magnitude of their deviation. If the deviation from the locus of model spheroids was less than it was from the locus of model disks, then I classified those galaxies as possessing $r^{1/4}$ profiles. If however, the converse was true, I classified those galaxies as possessing exponential profiles. But here is where I introduce some uncertainty in the classification scheme. Since these galaxies have such small deviations from both loci, even though I associate these galaxies with a certain profile, it does not mean that they cannot possess the other types of profiles. For example: although one galaxy (ID 3-404) was classified as possessing an exponential profile since its Sérsic index was only 2.1 σ away from the locus of the model disks, there was still a good chance that it could possess an $r^{1/4}$ profile since

Table 3–4: $0.5 \leq z \leq 1.2$ galaxies in the HDF-S

ID[a]	z^b	$M_I{}^c$	$n(I_{814})^d$	Class[e]	$R(I_{814})^f$	$\frac{\Delta(U_{300}-B_{450})_0{}^g}{\Delta\log(r)}$
(1)	(2)	(3)	(4)	(5)	(6)	(7)
2338	0.573	21.28	1.096 ± 0.0007	Int	3.828	−0.028 ± 0.010
2461	1.052	23.42	0.972 ± 0.0020	deV	1.569	−0.030 ± 0.010
2537	0.634	23.37	1.363 ± 0.0030	deV	1.495	−0.079 ± 0.013
2467	0.545	22.13	0.908 ± 0.0010	Int	2.233	−0.015 ± 0.003
2438	0.859	23.39	2.559 ± 0.0050	deV	3.648	−0.471 ± 0.013
2394	0.859	23.39	1.020 ± 0.0020	Irr	2.867	−0.059 ± 0.006
2389	1.107	23.58	0.555 ± 0.0009	Exp	2.423	−0.098 ± 0.007
2141	0.545	21.67	1.056 ± 0.0008	Int	4.987	−0.170 ± 0.007
2142	0.603	22.00	1.091 ± 0.0010	Int	2.099	0.083 ± 0.005
2403	0.634	23.71	0.851 ± 0.0010	deV	1.035	0.122 ± 0.006
2285	0.701	22.67	1.066 ± 0.0010	deV	0.928	0.263 ± 0.007
1703	0.634	21.58	1.070 ± 0.0009	Int	5.725	−0.082 ± 0.004
2059	0.904	21.22	1.567 ± 0.0020	deV	1.552	−0.077 ± 0.005
2068	0.573	23.52	0.471 ± 0.0008	Irr	3.032	0.081 ± 0.004
1670	0.518	19.56	1.727 ± 0.0009	deV	5.156	−0.230 ± 0.006
1913	0.573	23.79	0.569 ± 0.0013	Exp	2.346	−0.149 ± 0.007
1733	0.738	22.24	0.729 ± 0.0007	Exp	2.248	−0.139 ± 0.006
1657	0.545	22.74	0.750 ± 0.0009	Exp	1.214	0.024 ± 0.003
1429	0.545	22.84	1.147 ± 0.0020	deV	0.978	0.176 ± 0.006
1368	0.545	23.25	0.933 ± 0.0020	deV	1.626	−0.093 ± 0.010
1348	0.634	23.09	0.903 ± 0.0020	Exp	2.529	0.020 ± 0.005
1112	0.545	20.49	0.713 ± 0.0004	Exp	3.447	0.137 ± 0.007
1276	0.634	23.38	0.755 ± 0.0010	Exp	1.219	0.071 ± 0.003
1212	0.545	23.06	1.052 ± 0.0020	deV	2.731	−0.168 ± 0.006
1171	0.817	22.92	0.713 ± 0.0020	Exp	2.610	0.193 ± 0.010
960	0.573	22.67	1.117 ± 0.0020	deV	3.474	−0.083 ± 0.008
769	0.603	20.90	1.841 ± 0.0010	deV	1.919	−0.109 ± 0.004
933	0.605	23.22	0.874 ± 0.0010	Int	0.655	−0.271 ± 0.040
628	0.738	21.41	2.172 ± 0.0040	deV	4.833	−0.260 ± 0.011
742	0.545	23.56	0.814 ± 0.0009	Exp	1.995	−0.013 ± 0.006
701	0.634	21.76	1.353 ± 0.0030	deV	0.644	−0.057 ± 0.008
416	0.545	22.94	0.812 ± 0.0010	Exp	2.515	0.049 ± 0.003
405	0.518	21.61	1.338 ± 0.0008	deV	1.337	−0.119 ± 0.003
403	0.776	23.34	0.951 ± 0.0020	Exp	2.697	−0.155 ± 0.009
358	0.573	21.46	1.554 ± 0.0010	deV	1.638	−0.030 ± 0.003
306	0.859	23.50	0.849 ± 0.0020	Exp	2.139	−0.155 ± 0.009
36	0.518	24.40	0.609 ± 0.0020	Exp	1.973	−0.057 ± 0.007
2319	0.701	24.54	1.142 ± 0.0060	deV	2.093	0.121 ± 0.012
2071	1.000	24.72	0.450 ± 0.0010	Irr	2.750	−0.024 ± 0.008
1855	0.573	24.33	0.658 ± 0.0009	Exp	1.129	−0.074 ± 0.013
1142	1.000	24.41	0.954 ± 0.0020	deV	1.116	−0.144 ± 0.032
581	0.817	24.59	0.643 ± 0.0020	Exp	2.486	−0.125 ± 0.016

[a] IDs are from Casertano et al. 2000.

[b] Redshifts are from Chen et al. 1998 and Yahata et al. 2000.

[c] F814W AB mag within ~ 26 mag arcsec^{-2}.

[d] Sérsic index in rest-frame B.

[e] (deV) de Vaucouleurs, (Exp) exponential, (Int) intermediate, (Irr) irregular.

[f] I_{814} half-light radius in kiloparsecs.

[g] Rest-frame $(U_{300} - B_{450})_0$ color gradient within $R_{1/2} \sim 4$ kpc.

Table 3–5: $2.0 \leq z \leq 3.6$ galaxies in the HDF-S

ID[a] (1)	z^b (2)	$M_H{}^c$ (3)	$n(H_{160})^d$ (4)	Class[e] (5)	$R(H_{160})^f$ (6)	$\frac{\Delta(U_{300}-B_{450})_0{}^g}{\Delta\log(r)}$ (7)	$\frac{\Delta(B_{450}-V_{606})_0{}^h}{\Delta\log(r)}$ (8)
0273-0801	2.55	25.11	0.924 ± 0.008	...	2.143	-0.043 ± 0.148	...
0343-0957	2.77	25.68	0.744 ± 0.013	...	1.868	-0.237 ± 0.183	...
0440-0353	2.32	24.41	0.759 ± 0.026	Exp	2.572	-0.263 ± 0.070	0.608 ± 0.186
0454-0831	3.58	22.77	...	Irr	5.239	0.093 ± 0.027	-0.143 ± 0.047
0471-0776	2.13	23.76	0.530 ± 0.001	Exp	3.150	-0.038 ± 0.015	0.280 ± 0.051
0498-0826	2.30	24.94	0.629 ± 0.004	...	2.528	-0.014 ± 0.048	0.387 ± 0.262
0501-0899	2.39	23.87	0.674 ± 0.001	Exp	2.606	-0.056 ± 0.031	1.020 ± 0.328
0524-0397	2.83	24.87	...	Irr	4.367	-0.282 ± 0.123	0.875 ± 0.304
0565-0940	2.33	25.14	0.520 ± 0.001	...	2.279	0.003 ± 0.026	...
0632-0916	2.53	24.88	0.523 ± 0.008	...	1.860	0.019 ± 0.092	0.131 ± 0.354
0643-0943	2.05	24.82	0.770 ± 0.005	...	2.474	0.185 ± 0.051	...
0647-0899	2.01	23.29	1.075 ± 0.002	deV	2.927	-0.236 ± 0.035	-0.085 ± 0.071
0648-0382	2.27	23.69	0.710 ± 0.002	Exp	2.436	0.003 ± 0.040	0.269 ± 0.234
0672-0763	2.33	24.97	0.446 ± 0.006	...	2.619	0.006 ± 0.081	0.471 ± 0.275
0748-0511	2.56	24.90	...	Irr	3.140	-0.045 ± 0.083	0.345 ± 0.164
0792-1032	3.60	25.19	0.587 ± 0.005	...	2.074	-0.072 ± 0.088	...
0801-0926	2.68	25.00	0.469 ± 0.004	...	2.496	0.106 ± 0.085	0.690 ± 0.266
0858-0848	3.59	24.10	0.815 ± 0.004	deV	2.509	0.101 ± 0.053	0.344 ± 0.294
0870-0866	2.32	24.42	0.704 ± 0.004	deV	2.718	-0.033 ± 0.051	...
0890-0961	2.39	23.82	0.795 ± 0.002	Exp	2.268	-0.125 ± 0.146	0.640 ± 0.363

[a] IDs are from Gwynn and Hartwick 1996.

[b] Redshifts are from Gwynn and Hartwick 1996.

[c] F160W AB mag within ~ 26 mag arcsec^{-2}.

[d] Sérsic index in rest-frame B.

[e] (deV) de Vaucouleurs, (Exp) exponential, (Int) intermediate, (Irr) irregular.

[f] H_{160} half-light radius in kiloparsecs.

[g] Rest-frame $(U_{300}-B_{450})_0$ color gradient within $\sim$28 mag arcsec^{-2}.

[h] Rest-frame $(B_{450}-V_{606})_0$ color gradient within $\sim$28 mag arcsec^{-2}.

it was only 3.3 σ away from the locus of model spheroids. Or it could also possibly possess an intermediate profile.

Although some galaxies have less than 5 σ deviations from both loci, I assume that their morphological classification is still reliable unless they have less than a 2.5 σ difference between the standard deviation calculated from the de Vaucouleurs loci and the standard deviation calculated from the exponential loci. For example, the classification for galaxy 3-404 is not very robust since the difference between the two standard deviations is only ~ 0.8 σ. In the HDF-N, there is one galaxy in the intermediate redshift sample and one in the high-redshift sample; while in the HDF-S, there are 5 out of a sample of 42 galaxies at intermediate-redshifts and three out of nine galaxies at high-redshifts that represent these borderline cases. Since the misclassification of these borderline galaxies can potentially change the conclusions (especially in the HDF-S), I will present two sets of results and observe

if they differ greatly from each other. One will include all the galaxies that are classified systematically by the magnitude of their deviation from the loci of galaxy types and the other will exclude those galaxies in which there exists less than a 2.5 σ difference between the deviation from the de Vaucouleurs and the deviation from the exponential loci of galaxies. I will term the first set of results "Morphological Classification I" (MC-I) and the second set "Morphological Classification II" (MC-II).

When I classify the morphologies of the galaxies, I do not claim that objects possessing exponential profiles are disks while objects possessing de Vaucouleurs profiles are spheroids; since many dwarf spheroidals have been shown to possess exponential profiles (Koo et al. 1994; Koo et al. 1995). However, for simplicity, when comparing my results with the results from the literature I will assume that galaxies possessing de Vaucouleurs profiles correspond to the spheroidal population while galaxies possessing exponential profiles correspond with the disk population. I naively lump into one category ("Irr") those galaxies which have irregular profiles and do not follow an exponential or $r^{1/4}$ law. Wu (1999) explain that there are actually two types of "irregular" galaxies. One type is the traditional irregular which is the late-type system classified in the Hubble scheme whereas the other type possesses an irregular profile as a result of galaxy-galaxy interactions and mergers. However, it is not within the scope of this study to differentiate between the two types.

At intermediate-redshifts, the morphologies are better constrained since the galaxies are brighter and the distinction between the model spheroids and disks is more apparent. As a further check on the accuracy of the classification system, I visually inspect the images of the intermediate-redshift galaxies since many of them are large enough and bright enough to classify their morphologies by eye. It should be kept in mind that the galaxy classification process is rather crude since it relies

mainly on the galaxy models which should be regarded as highly speculative at small scale lengths and faint magnitudes. Thus, it is evident that my classification scheme represents an oversimplification designed to obtain a sense of the overall trends in the morphologies of the galaxies and should not be taken as a robust classification scheme to constrain the morphologies of individual galaxies.

Column (4) of Tables 3-1, 3-2, 3-4, and 3-5 lists the Sérsic indices in the I_{814} passband for galaxies at intermediate-redshifts and the H_{160} passband for galaxies at high-redshifts. Column (5) of these tables lists the morphological type for the galaxies that were bright enough for their profiles to be classified. Under my scheme, "deV" represents a de Vaucouleurs ($r^{1/4}$) profile, "Exp" represents an exponential profile, "Int" represents an intermediate profile with $1 \leq n \leq 4$ (these galaxies most likely possess both a bulge and disk component), and "Irr" represents galaxies that possess irregular substructure.

3.1.1 Hubble Deep Field-North

Figures 3-1, 3-2, and 3-3 show the surface brightness profiles and the fits to the profiles of all the galaxies in the HDF-N sample. Figures 3-4 and 3-5 represent plots of the half-light radii versus the Sérsic indices ($r_{1/2} - n$) of the model disks and spheroids after they had been convolved with the HDF-N PSF in the I_{814} (with I_{814} = 21, 22, 23, and 24) and H_{160} (with H_{160} = 23 and 24) passband respectively. For the high-redshift sample, the results from the galaxy models are only reliable for $H_{160} \leq 24.5$ since for fainter magnitudes, it is difficult to clearly distinguish the locus of Sérsic indices for the model spheroids from the locus of Sérsic indices for the model disks. For all I_{814} magnitudes and for $H_{160} \leq 24.5$, I also plotted the values of the galaxies in the intermediate and high-redshift sample (represented by squares) to attempt to classify their morphologies by observing where they fall on the diagram. I did not include in these plots those galaxies that could not be fit by

the Sérsic law since their profiles were too irregular. These galaxies were, however, still included in the statistics and were labeled as "Irr" for "irregulars".

Table 3-6 (MC-I) and 3-7 (MC-II) summarizes the results from the morphological classification of the galaxies based on the combination of the results from the fits to the surface brightness profiles of the galaxies in the two redshift bins, $(r_{1/2} - n)$ plots of the galaxy models, and visual inspection. Quoted are the percentages found for each profile with their poissonian error. The number of galaxies possessing that profile is in parenthesis. The tables show that the MC-I and MC-II classfication schemes give similar results. Since the results from the MC-I and MC-II system only differ by a few percentage points in the HDF-N, I will discuss my conclusions from the MC-I system only. Out of the 32 galaxies in the intermediate-redshift sample, I classified 28 $\pm$ 9% as possessing $r^{1/4}$ profiles, 41 $\pm$ 13% as possessing exponential profiles, 25 $\pm$ 9 % as intermediates, and 6 $\pm$ 3% as irregulars. The galaxy that I did not include in the statistics is ID 3-610 in which both an $r^{1/4}$ and an exponential component could be resolved. The Sérsic index for the inner region of this galaxy is 2.32 while for the outer, disk part it is 0.826. This is the only galaxy large enough in the sample to distinguish the two components. In the high-redshift sample only 20 galaxies had $H_{160} \leq 24.5$. Out of these galaxies, I classified 60 $\pm$ 15% as possessing $r^{1/4}$ profiles, 20 $\pm$ 10% as possessing exponential profiles, and 20 $\pm$ 10% as irregulars. In the high-redshift bin, I did not classify any galaxies as possessing intermediate profiles. This does not mean that intermediates do not exist at these redshifts, but rather that since the separation between the locus of model spheroids and model disks is very small, there is not a clearly defined region for the intermediate cases.

These results are limited by small number statistics, especially at high redshifts since I was only able to classify the morphologies of 20 out of a sample of 50 galaxies. Nevertheless, I can still comment on the general trends seen.

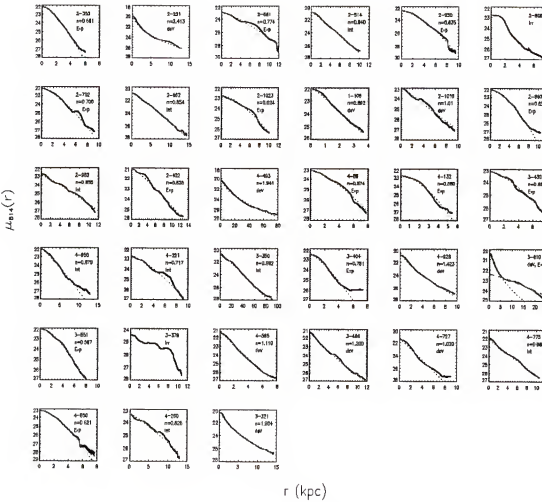

Figure 3–1: I_{814} surface brightness profiles for the intermediate-redshift sample in the HDF-N. The dotted line represents a generalized exponential fit to the profile. Included in the plots are the galaxy IDs from the Williams et al. 1996 catalog, the value of the Sérsic indices (n), and the morphological classification. Those galaxies with no Sérsic index indicated have irregular structure precluding a fit to the profile.

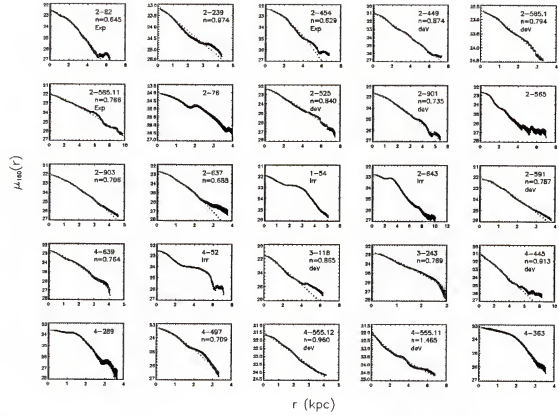

Figure 3–2: H_{160} surface brightness profiles for the high-redshift sample identified by spectroscopic redshifts in the HDF-N. The dotted line represents a generalized exponential fit to the profile. Included in the plots are the galaxy IDs from the Williams et al. 1996 catalog, the value of the Sérsic indices (n), and the morphological classification of galaxies with $H \leq 24.5$. Those galaxies with no Sérsic index indicated have irregular structure precluding a fit to the profile.

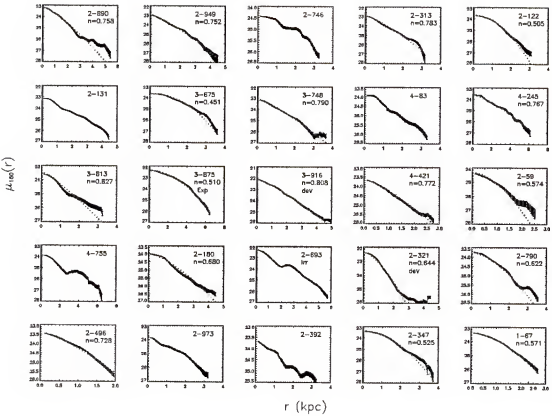

Figure 3–3: H_{160} surface brightness profiles for the high-redshift sample identified by photometric redshifts in the HDF-N. The dotted line represents a generalized exponential fit to the profile. Included in the plots are the galaxy IDs from the Williams et al. 1996 catalog, the value of the Sérsic indices (n), and the morphological classification of galaxies with $H \leq 24.5$. Those galaxies with no Sérsic index indicated have irregular structure precluding a fit to the profile.

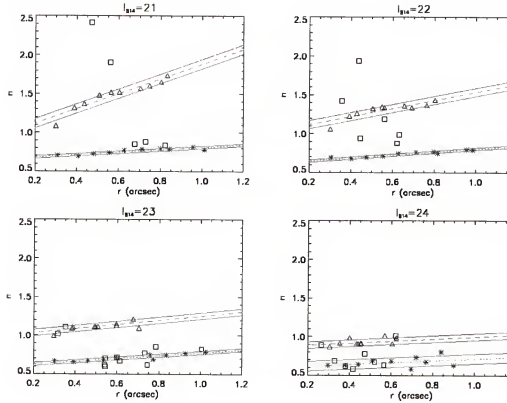

Figure 3–4: Half-light radii versus Sérsic index ($r_{1/2} - n$) for the model disks and spheroids after they were convolved with the I_{814} PSF with I_{814}= 21, 22, 23, and 24. Triangles represent model spheroids, asterisks represent model disks, and squares represent the intermediate-redshift galaxies in the HDF-N sample. The dashed and dotted line are a weighted least-squares fit to the model spheroids and model disks respectively. The solid lines are the 1 σ deviations of the fits.

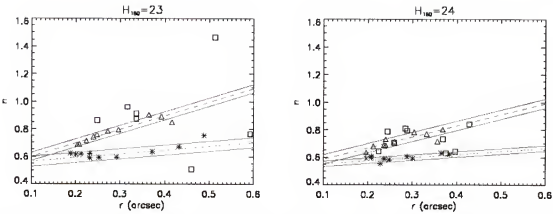

Figure 3–5: Half-light radii versus Sérsic index ($r_{1/2} - n$) for the model disks and spheroids after they were convolved with the H_{160} PSF with H_{160}= 23 and 24. Triangles represent model spheroids, asterisks represent model disks, and squares represent the high-redshift galaxies in the HDf-N sample. The dashed and dotted line are a weighted least-squares fit to the model spheroids and model disks respectively. The solid lines are the 1 σ deviations of the fits.

Table 3-6 reveals that, at higher look-back time, the fraction of the galaxies possessing $r^{1/4}$ profiles increased by 32 $\pm$ 18% whereas the fraction of exponential-type profiles decreased by 21 $\pm$ 16%. These differences are marginally significant since they represent $< 2\ \sigma$ changes in both cases. At high-redshifts, there is a statistically insignificant increase of 14 $\pm$ 10% in the fraction of irregular galaxies.

Table 3–6: Morphological classification I of galaxies in the HDF-N

Redshift	Total	de Vaucouleurs	Exponentials	Intermediates	Irregulars
$0.5 \leq z \leq 1.2$	32	28±9% (9±3)	41±13% (13±4)	25±9% (8±3)	6±3% (2±1)
$2.0 \leq z \leq 3.5$	20	60±15% (12±3)	20±10% (4±2)	0 (0)	20±10% (4±2)

Table 3–7: Morphological classification II of galaxies in the HDF-N

Redshift	Total	de Vaucouleurs	Exponentials	Intermediates	Irregulars
$0.5 \leq z \leq 1.2$	31	26±10% (8±3)	42±13% (13±4)	26±10% (8±3)	6±3% (2±1)
$2.0 \leq z \leq 3.5$	19	63±16% (12±3)	16±11% (3±2)	0 (0)	21±11% (4±2)

3.1.2 Hubble Deep Field-South

In the HDF-S, we are even more limited by small number statistics at high-redshifts since the field of view of the NICMOS field is 1/6th the size of the NICMOS HDF-N field. The sample size of high-redshift galaxies in the HDF-S is less than half that of the HDF-N. Out of the 20 total high-redshift galaxies in the HDF-S, only 9 have $H \leq 24.5$ and are bright enough to be classified. Furthermore,

there are no high-redshift galaxies brighter than H = 23.5. Thus, in this case, the errors in the classification system will be larger than that of the HDF-N sample.

Since galaxy classification would be more robust on the images with higher spatial resolution, I generated surface brightness profiles for all 42 galaxies in the intermediate-redshift sample and 9 of the galaxies in the high-redshift sample on the images before PSF matching was performed to degrade the resolution to that of the adjacent passband. Figures 3-6 and 3-7 show the I_{184} and H_{160} surface brightness profiles and the fits to the profiles for all the galaxies that were classified at intermediate and high-redshift respectively. At these redshifts, the profiles probe approximately their rest-frame B wavelengths. I fit Sérsic profiles to all the galaxies except those with irregular profiles. The galaxy identification numbers, Sérsic indices, and morphological classification are also included in the plots.

Figures 3-8 and 3-9 represent plots of the half-light radii versus the Sérsic indices ($r_{1/2} - n$) of the model disks and spheroids after they had been convolved with the HDF-S PSF in the I_{814} (with I_{814} = 21, 22, 23, and 24) and H_{160} (with H_{160} = 24) passband respectively. For all I_{814} magnitudes and for $H_{160} \leq 24.5$, I overplotted the values of the galaxies in the intermediate and high-redshift sample (represented by squares) to attempt to classify their morphologies by observing where they fall on the diagram. I did not include in these plots those galaxies that could not be fit by the Sérsic law since their profiles were too irregular. These galaxies were, however, still included in the statistics and were labeled as "Irr" for "irregulars".

Table 3-8 (MC-I) and 3-9 (MC-II) summarizes the results from the morphological classification of the galaxies based on the combination of the fits to the surface brightness profiles of the galaxies in the two redshift bins, the ($r_{1/2} - n$) plots of the galaxy models, and visual inspection. Quoted are the percentages found for each profile with their poissonian error. From the tables, it is evident

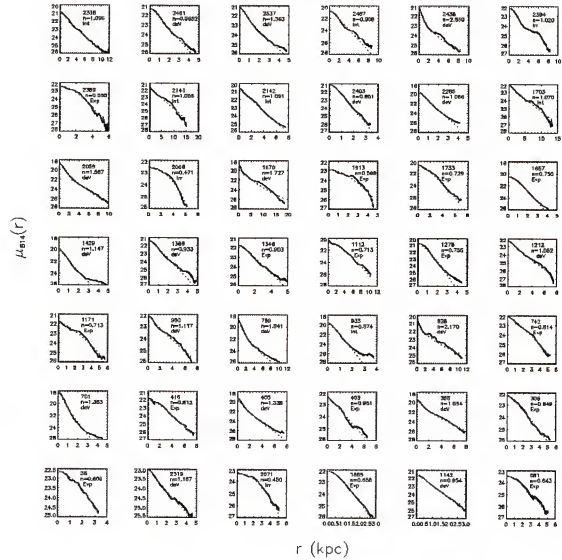

Figure 3–6: I_{814} surface brightness profiles for the 42 intermediate-redshift galaxies with I $\leq$ 24 in the HDF-S. The dotted line represents a generalized exponential fit to the profile. Included in the plots are the galaxy ID from Casertano et al. (2000), the value of the Sérsic index (n) if applicable, and the galaxy classification.

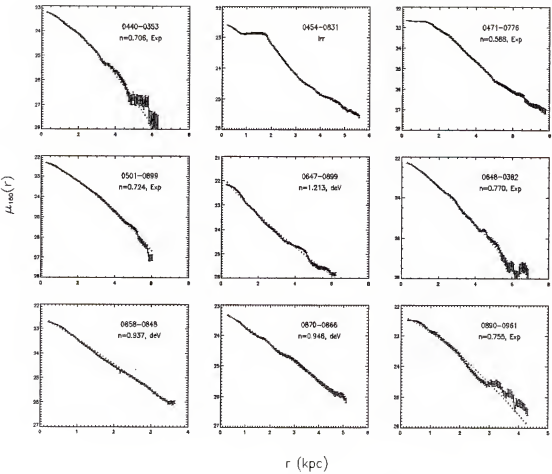

Figure 3–7: H_{160} surface brightness profiles for the 9 LBGS with H $\leq$ 24.5 in the HDF-S before convolution with the K_{222} PSF. The dotted line represents a generalized exponential fit to the profile. Included in the plots are the galaxy ID from the Yahata (2000) catalog, the value of the Sérsic index (n) if applicable, and the galaxy classification.

that, at intermediate-redshifts, the MC-I and MC-II methods give similar results. Using the MC-I method, I classified 43 ± 10% of the galaxies as possessing $r^{1/4}$ profiles, 36 ± 10% as possessing exponential profiles, 14 ± 7% as intermediates, and 7 ± 5% as irregulars. The numbers are not significantly different when I used the MC-II method to classify the galaxies at intermediate-redshifts. However, at high-redshifts, the two different methods produced two slightly different results. Using the MC-I method, I classified 33 ± 22% of the galaxies as possessing $r^{1/4}$ profiles, 55 ± 22% as possessing exponential profiles, and 11 ± 11% possessing irregular profiles. As in the HDF-North sample, I did not classify any galaxies at high-redshifts as possessing intermediate profiles. Again, this does not mean that galaxies possessing intermediate profiles do not exist at high-redshifts, but rather that there is not a clearly defined region for the intermediate cases since the locus of spheroids is not well separated from the locus of disks.

Table 3-8 would lead us to believe that the fraction of galaxies possessing de Vaucouleurs profiles have slightly decreased whereas the fraction of galaxies possessing exponential profiles have slightly increased with look-back time. These results conflict with the results found in the HDF-N. However, the results from Table 3-9 seems to be more in line with what is seen in the HDF-N. Remember that, here, the galaxies were classified under the MC-II system where the borderline cases were excluded from the statistics. Using the MC-II system, 3 galaxies which were all classified as exponentials under the MC-I system were discarded from the statistics. Since there were only 9 galaxies to start with, the exclusion of these 3 galaxies significantly reduced the fraction of galaxies possessing exponential profiles and in turn increased the fraction of galaxies possessing de Vaucouleurs profiles. Under the MC-II classification scheme, we now see that 50 ± 33% of galaxies at high-redshifts possess de Vaucouleurs' profiles and 33 ± 17% possess exponential profiles. Thus, under this scheme, there seems to be an increase with look-back

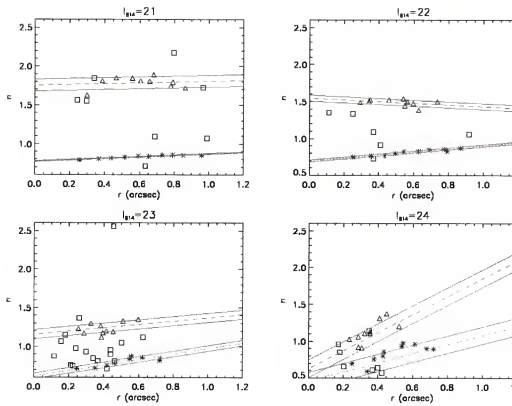

Figure 3–8: Half-light radii versus Sérsic index ($r_{1/2} - n$) for the model disks and spheroids after they were convolved with the I_{814} PSF with I_{814}= 21, 22, 23, and 24. Triangles represent model spheroids, asterisks represent model disks, and squares represent the intermediate-redshift galaxies in the HDF-S sample. The dashed and dotted line are a weighted least-squares fit to the model spheroids and model disks respectively. The solid lines are the 1 σ deviations of the fits.

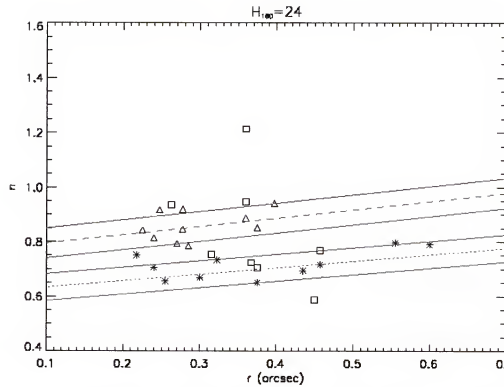

Figure 3–9: Half-light radii versus Sérsic index ($r_{1/2} - n$) for the model disks and spheroids after they were convolved with the H_{160} PSF with H_{160}= 23 and 24. Triangles represent model spheroids, asterisks represent model disks, and squares represent the high-redshift galaxies in the HDF-S sample. The dashed and dotted line are a weighted least-squares fit to the model spheroids and model disks respectively. The solid lines are the 1 σ deviations of the fits.

time in the fraction of galaxies with de Vaucouleurs' profiles and a decrease in the fraction of galaxies with exponential profiles. In the HDF-S, it is difficult to fairly compare the trends at intermediate-redshifts with the trends observed at high-redshifts since there is such a wide gap in the sample size of the two redshift bins. In the HDF-N, however, the sample size of the two redshift bins are more comparable, thus my conclusions there are more robust. To increase the sample size and strengthen my conclusions, I combined the results from the HDF-N and HDF-S profile classification. I present my results in the following section.

Table 3–8: Morphological classification I of galaxies in the HDF-S

Redshift	Total	de Vaucouleurs	Exponentials	Intermediates	Irregulars
$0.5 \leq z \leq 1.2$	42	43±10% (18±4)	36±10% (15±4)	14±7% (6±3)	7±5% (3±2)
$2.0 \leq z \leq 3.6$	9	33±22% (3±2)	55±22% (5±2)	0 (0)	11±11% (1±1)

Table 3–9: Morphological classification II of galaxies in the HDF-S

Redshift	Total	de Vaucouleurs	Exponentials	Intermediates	Irregulars
$0.5 \leq z \leq 1.2$	37	43±11% (16±4)	32±12% (12±3)	16±8% (6±3)	8±5% (3±2)
$2.0 \leq z \leq 3.6$	6	50±33% (3±2)	33±17% (2±1)	0 (0)	17±17% (1±1)

3.1.3 Hubble Deep Field-North vs Hubble Deep Field-South

Given that the galaxies in the HDF-N and HDF-S have similar distributions in redshifts and magnitudes, one can increase the statistics on the morphologies of the galaxies by combining the results from the two fields. In this way, the poissonian errors are reduced. Table 3-10 (MC-I) and 3-11 (MC-II) summarizes the results for the morphological classification of galaxies in both the HDF-N and HDF-S. The percentages are given with their poissonian errors and the total number of galaxies possessing the profiles is given in parenthesis. The results from combining the statistics in both Hubble Deep Fields under both the MC-I and MC-II system gives evidence to an increase in the fraction of galaxies possessing de Vaucouleurs profiles and a decrease in the fraction of galaxies possessing exponential profiles with look-back time. Under the MC-II system, the differences between the intermediate and high-redshift sample are more pronounced. However, given that the increases

Table 3–10: Morphological classification I of galaxies in the HDFs North and South

Redshift	Total	de Vaucouleurs	Exponentials	Intermediates	Irregulars
$0.5 \leq z \leq 1.2$	74	36±7% (27±5)	38±7% (28±5)	19±5% (14±4)	7±3% (5±2)
$2.0 \leq z \leq 3.6$	29	52±14% (15±4)	31±10% (9±3)	0 (0)	17±7% (5±2)

Table 3–11: Morphological classification II of galaxies in the HDFs North and South

Redshift	Total	de Vaucouleurs	Exponentials	Intermediates	Irregulars
$0.5 \leq z \leq 1.2$	68	35±7% (24±5)	37±7% (25±5)	21±6% (14±4)	7±3% (5±2)
$2.0 \leq z \leq 3.6$	25	60±16% (15±4)	20±8% (5±2)	0 (0)	20±8% (5±2)

are on the order of $\sim 1\ \sigma$ in both cases, the differences are not very significant. There is also evidence of an increase on the $1\ \sigma$ level in the fraction of galaxies that possess irregular profiles or that are intrinsically flat (Sérsic indices < 0.5) with look-back time.

These results seem to support the idea that the morphologies of galaxies have evolved with time. In particular, the spheroidal population may have predated the spiral population, at least from the epoch of the LBGs. Since the surface brightness profiles of the LBGs reveal that the majority of them possessed $r^{1/4}$ profiles, they could very well be the direct progenitors of today's luminous ellipticals or spiral bulges. However, in Section 5.3, I will show that my results are also consistent with the idea that these galaxies are starburst systems and depending on their merger history, they can evolve into any of the luminous galaxies we see today. If structure is indeed formed hierarchically, it is likely that mergers will be the major contributor in shaping the final morphologies of galaxies. Although I detected slight changes in morphology between the two redshift bins, these changes may not be solely attributed to evolution. In Section 4.4, I discuss the possibility that the trends in morphology may be influenced by observational selection effects. However, if there were indeed more galaxies possessing de Vaucouleurs and irregular profiles in the past than there are now, this could lead to interesting implications in merger and galaxy formation theories. In Chapters 5 and 6, I

compare my results with predictions from merger and galaxy formation simulations to explore these implications.

3.1.4 Discussion

Given the high degree of difficulty in the classification of the morphologies of these small, faint galaxies (which are severely affected by the PSF) and the limitation of small number statistics, the morphological evolution of galaxies still represents a new and relatively unexplored terrain. Most studies of galaxy morphology have been conducted at redshifts less than 1. There have been some fledgling attempts to include the high-redshift population, but many of those studies did not attempt to separate morphological types into specific redshift bins since the redshifts of LBGs were not readily available at the time. Albeit, there is a paucity of information on the morphologies of galaxies, it is still useful to compare the results from this study with the results that are currently available. To consistently compare my results with other observations, I eliminate the "intermediates" category in my classification scheme since these studies did not include that class in their scheme. Instead, I divide the galaxies originally classified as "intermediates' into those possessing $r^{1/4}$ and those possessing exponential profiles according to their deviations from the loci of the model galaxies. For simplicity, I assume that the galaxies possessing $r^{1/4}$ profiles are spheroids while galaxies possessing exponential profiles are spirals.

I compare my results using the MC-I system at intermediate-redshifts with Van Den Bergh et al. (1996, 2000) (Van96) who visually classified galaxies in the HDF-N and Aguerri and Trujillo (2002) (AT02) who used an automated scheme to classify galaxies up to a redshift of 0.8 in the Hawaiian Deep Fields SSA13 and SSA22. Table 3-12 lists the results from my profile classification of the intermediate-redshift galaxies and the results from the two classification schemes from the literature. By subdividing the "Intermediates" class, the percentages of

Table 3–12: Comparisons between different morphological classification schemes at intermediate-redshifts

Classification Scheme	Spheroids	Spirals	Unclassified
MC-I	47%	46%	7%
Van96	30%	31%	39%
AT02	33%	41%	26%

spheroids and spirals increase in my classification scheme. Under my classification scheme, 47% of the galaxies are spheroids, 46% are spirals, and 7% are unclassified. Van Den Bergh et al. (1996, 2000) found similar fractions in galaxy morphologies in their visual classification of the galaxies in the HDF-N. They visually classified 30% of the galaxies as spheroids, 31% as spirals, and 39% as unclassified. My results are also in broad agreement with AT02. They found that 33% of the galaxies are spheroidal type objects (E/S0), 41% are spirals, and 26% are mergers and unclassified objects.

Aguerri and Trujillo (2002) applied a more sophisticated method to classify the galaxies than the one used in this study. They took into account the intrinsic ellipticities of the galaxies by fitting both the observed 2-dimensional surface brightness and ellipticity profiles with convolved profiles of their model surface brightness distributions. They also defined a limit in absolute magnitudes for the sample whereas I applied a limit in apparent magnitudes. Applying a cutoff in absolute magnitudes is preferable since applying a cutoff in apparent magnitudes potentially biases the selection of galaxies to those that are intrinsically brighter at higher redshifts. Despite the simplifications used in this study, the results are consistent with the more refined classification system used by AT02. This provides confidence that the classification scheme applied in this study is fairly robust, at least when used to classify intermediate-redshift galaxies.

Although my results are more consistent with those published by AT02 and Van96, there are some differences that must be taken under consideration. I found a much lower fraction of "irregular" galaxies compared to AT02 and Van96. However, many of the galaxies in my HDF sample that possessed smooth profiles

and were thus classified as "de Vaucouleurs" or "exponential" under my scheme, appeared to be actually irregular upon visual inspection. The irregularities that are apparent in the images do not seem to manifest themselves in the 1-dimensional, azimuthally averaged surface brightness profiles. Since AT02 analyzed the surface brightness distribution in 2 dimensions rather than 1 dimension, inhomogenieties in the galaxy structure will be more apparent. Irregular substructure will also be more apparent in the visual classification method used by Van96. Thus, under their schemes, more galaxies in my sample would be classified as "irregular" and "unclassified" types.

The results in this study differ from the morphological study of galaxies in the HDF-N conducted by Marleau and Simard (1998) (MS98). By using a profile decomposition method on 522 galaxies down to $I_{814}(\mathrm{AB}) < 26$, MS98 found that the majority of HDF-N galaxies are disk-dominated with only 8% having dominant bulge fractions. My profile classification scheme revealed a much higher fraction of galaxies possessing spheroidal profiles in the Hubble Deep Fields at both intermediate and high-redshifts. Whereas, they classified only 8% of the galaxies as possessing dominant bulge fractions, I found that $\sim 47\%$ of the galaxies in the intermediate-redshift sample and $\sim 52\%$ of the galaxies in the high-redshift sample possess spheroidal profiles. Their results also showed a decrease in the number of bulge-dominated galaxies as a function of look-back time whereas I observed a marginal increase in the population of these galaxies.

Figure 3-10 compares the results from my morphological classification with the bulge fractions (B/T) determined by MS98 for the galaxies at intermediate and high-redshifts which were included in this sample and in the MS98 sample. Under their system, all the galaxies with $B/T > 0.5$ were defined as bulge-dominated, whereas all the galaxies with $B/T \leq 0.5$ were defined as disk-dominated. In the total sample of 62 galaxies, 7 (11%) galaxies would be considered as bulge-dominated

by MS98 according to the values of their bulge fractions. At intermediate-redshifts 27% (7 out of 26) of the galaxies do not compare well with the bulge fractions determined by MS98. In all the discrepant cases, the galaxies that were classified as possessing spheroidal structure in this study were found to possess $B/T < 0.5$ by MS98. At high-redshifts, the results seem to be even more different. Here, 50% (8 out of 16) galaxies possessed discrepant bulge fractions compared to their classification. In all 8 cases, the galaxies that I classified as spheroids all possessed $B/T < 0.5$. This discrepancy is larger than the errors in the classification in this study. In their simulations to test the robustness of their method, MS98 found that their method underestimated the B/T of the galaxies with high input B/T, i.e., galaxies possessing spheroidal profiles. Furthermore the difference between the input B/T and observed B/T was higher for galaxies with small apparent half-light radii than for larger galaxies. This may explain why we see a discrepancy between this study and the study conducted by MS98, especially at high-redshifts where galaxies typically possess smaller apparent angular sizes.

Other attempts at morphological classification relied upon quantifying the central concentration and asymmetry (Abraham et al. 1996 [Abra96]; Corbin et al. 2001 [Corb01]) of galaxies in the Hubble Deep Fields. In this classification scheme, late-type and irregular systems are assumed to possess higher asymmetry and lower concentration indices than early-type systems. In their studies, Abra96 and Corb01 detected a steady increase in the asymmetry of galaxies with look-back time. This corresponds to an increase in the fraction of late-type galaxies and irregular galaxies. At first inspection, their results seem to differ from what is observed in my study, which found a decrease in the fraction of galaxies possessing exponential profiles (late-types) and an increase in the fraction of galaxies possessing $r^{1/4}$ profiles (early-types) with look-back time. However, since high asymmetry is indicative of both late-type and irregular galaxies, it is difficult to assess whether

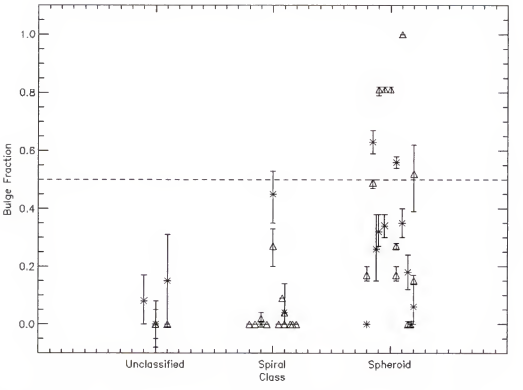

Figure 3–10: Comparison of the morphological classification of galaxies in the HDF-N with the value of the bulge fraction in Marleau & Simard (1998). Triangles represent the intermediate-redshift sample and asterisks represent the high-redshift sample. The horizontal dashed line represents the cut off between bulge-dominated and disk-dominated galaxies.

the increase in asymmetry with redshift is due to an increase in the late-type population, irregular population, or both populations. A decrease in the late-type population with redshift cannot be ruled out in their paper since it might well be the case that the increase in asymmetry with redshift may be caused by an increase in the fraction of irregular galaxies with look-back time. This seems plausible since I also detect an increase in this population with redshift.

However, since these studies classify galaxies in terms of low and high asymmetry instead of the standard morphological types (e.g., ellipticals, spirals, irregulars), it is difficult to fairly compare results. Thus, in order to consistently compare my results with theirs, I re-classifed the galaxies in this study. Those galaxies that were formally classifed as possessing de Vaucouleurs profiles are now classified as

Table 3–13: Rebinned morphologies of galaxies in the HDFs North and South

Redshift	Early-Type	Late-Type
$0.5 \leq z \leq 1.2$	47±8%	53±8%
$2.0 \leq z \leq 3.6$	52±14%	48±13%

early-types and are assumed to correlate with low asymmetry objects; and those that were classfied as exponentials and irregulars are now classified as late-types and are assumed to correlate with high asymmetry objects. Table 3-13 lists the results from the morphological classification of galaxies rebinned into the early-type and late-type classes.

Even after rebinning the galaxies, my results do not seem to agree with the results in Corb01 and Abra96. Table 3-13 shows that, within the errors, the fraction of early-type and late-type objects do not change much with time. This difference, however, could be due to certain biases in the observations. Corb01 state that the increase seen in the asymmetry with redshift may be an artifact due to angular resolution. They suggested that the galaxies that were classified as early-types using the poorer resolution NICMOS images seem to possess higher assymetry than the galaxies which were classified using WFPC-2. Wu (1999) also demonstrated that the increase of galaxies with high asymmetries at high-redshifts can be naturally explained by observational selection effects (Section 4.4). If this is true, then they may be systematically under classifying the fraction of early-type galaxies and, consequently, over classifying the fraction of late-type and irregular galaxies at high-redshifts since these galaxies were classified using the poorer resolution NICMOS images.

Despite the differences detected, most of the recent studies (including this one) concur that galaxies at intermediate and high-redshifts possess profiles that are more disturbed than local galaxies. Many believe that mergers are responsible for causing these disturbed morphologies. If this is found to be true, it would give support to the picture of a universe in which structure forms in a hierarchical manner. Although there is a general consensus reached, caution must be applied

in this interpretation since it has been shown that, at high-redshifts, we may be systematically observing the brightest galaxies, which may be biased to irregular systems (Wu 1999). Since there has not been much work performed on the morphologies of galaxies at high-redshifts and the few studies that have been done are still filled with a high level of uncertainty, it is still difficult to constrain the morphologies of these Lyman-break galaxies.

3.2 Color Profiles

The color profiles of galaxies are useful for determining whether significant color gradients exists in galaxies and whether these gradients evolve over time. The sign of the gradient give us an idea of the locations of the star forming regions if the color gradient is caused by an age gradient alone. If the galaxy possesses a *positive* gradient, this would indicate a blueing towards the center which might be explained by star formation that is centrally concentrated. If the galaxy possesses a *negative* gradient, this would point to a reddening in the center which would imply that an older stellar population exists there. If, however, there is no significant gradient in the galaxy, then the star formation regions are uniformly dispersed throughout the galaxy. Because of the $(1+z)^4$ fall off in the surface brightness, the color profiles of the high-redshift sample do not extend to the low surface brightness levels of the intermediate-redshift sample. For example, the profiles of the high-redshift galaxies might reach depths of up to 28 mag arcsec^{-2}, but because of the surface brightness fading, this would translate to a depth of only ~ 24.5 mag arcsec^{-2} in the intermediate-redshift sample. To consistently compare the results for the two redshift bins, one must sample over approximately the same surface brightness range; thus, a cutoff in surface brightness in the intermediate- redshift sample needs to be applied. Applying a cutoff in the radial range is approximately the same as applying the cutoff in surface brightness. Thus, I have chosen to fit the color profiles of the intermediate-redshift sample only out to a radius of 4 kpc.

This radius cutoff represents approximately twice the mean half-light radius of the high-redshift sample which was determined by summing up all the light within approximately 28 mag arcsec^{-2}.

3.2.1 Hubble Deep Field-North

I generated $(B_{450} - V_{606})$ and $(V_{606} - I_{814})$ color profiles for the 33 intermediate-redshift galaxies and $(I_{814} - J_{110})$ and $(J_{110} - H_{160})$ color profiles for the 50 LBGs in the HDF-N. K-corrections were applied to convert these color profiles into their rest-frame colors. I have chosen the filters such that they probe approximately the same rest-frame wavelengths at all redshifts. At their respective redshifts, the filters probe the galaxy's rest-frame $(UV_{218} - U_{300})_0$ and $(U_{300} - B_{450})_0$ color profiles. Since I will be comparing the color gradients of the intermediate-redshift galaxies with their high-redshift counterparts, from now on, I will refer to the gradients of the galaxies in the Hubble Deep Fields by their rest-frame colors. Figures 3-11 and 3-12 represent the rest-frame $(UV_{218} - U_{300})_0$ and $(U_{300} - B_{450})_0$ color profiles of the intermediate-redshift galaxies in the HDF-N, while Figures 3-13 to 3-16 represent the same rest-frame color profiles but for the high-redshift galaxies.

Figure 3-17 represents a plot of the redshift versus the $(UV_{218} - U_{300})_0$ and $(U_{300} - B_{450})_0$ color gradients of the galaxies in the two redshift bins. Table 3-14 lists their rest-frame median color gradients. Both the figure and the table show that the intermediate-redshift galaxies possess predominantly negative color gradients. The negative color gradients may indicate that the centers of these galaxies consist of older stellar populations and/or higher metallicities than the outer regions. The median color gradient is -0.123 ± 0.073 mag/dex in $(UV_{218} - U_{300})_0$ and -0.060 ± 0.063 mag/dex in $(U_{300} - B_{450})_0$. Over 60% of the galaxies at intermediate-redshifts possess negative gradients. Out of the galaxies that possess negative gradients, only $\sim 30\%$ of them possess gradients larger than -0.20 mag/dex. Since the medians of the color gradients of all the galaxies at

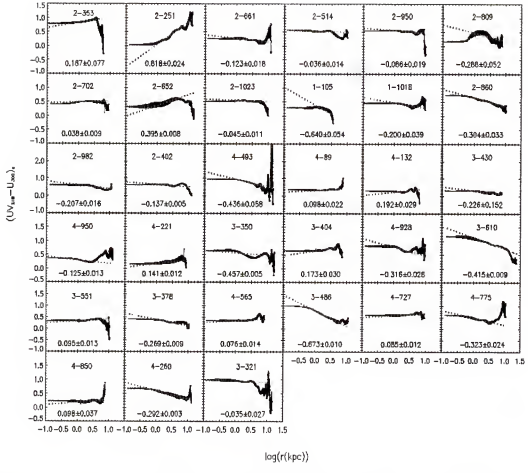

Figure 3–11: Rest-frame $(UV_{218} - U_{300})_0$ logarithmic color profiles for the intermediate-redshift sample in the HDF-N. The thickness of the line represents the correlated statistical errors. The dotted line represents a weighted least-squares fit to the profile starting from 0.14 arcseconds outwards. Included are the galaxy IDs and the value of the color gradients determined from the least-squares fit with their associated errors. The errors include the uncertainties from the fits and the 1 σ uncertainty due to the systematic background subtraction

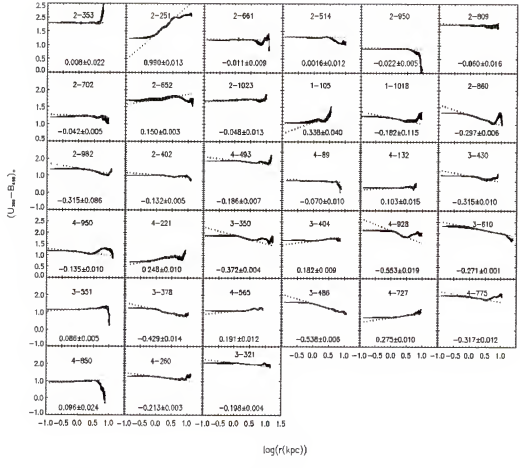

Figure 3–12: Rest-frame $(U_{300} - B_{450})_0$ logarithmic color profiles for the intermediate-redshift sample in the HDF-N. The thickness of the line represents the correlated statistical errors. The dotted line represents a weighted least-squares fit to the profile starting from 0.14 arcseconds outwards. Included are the galaxy IDs and the value of the color gradients determined from the least-squares fit with their associated errors. The errors include the uncertainties from the fits and the 1 σ uncertainty due to the systematic background subtraction

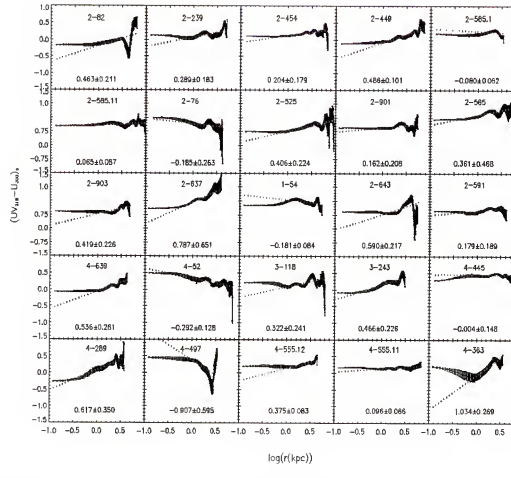

Figure 3–13: Rest-frame $(UV_{218} - U_{300})_0$ logarithmic color profiles for the high redshift sample with spectroscopic redshifts in the HDF-N. The thickness of the line represents the correlated statistical errors. The dotted line represents a weighted least-squares fit to the profile starting from 0.14 arcseconds outwards. Included are the galaxy IDs and the value of the color gradients determined from the least-squares fit with their associated errors. The errors include the uncertainties from the fits and the 1 σ uncertainty due to the systematic background subtraction.

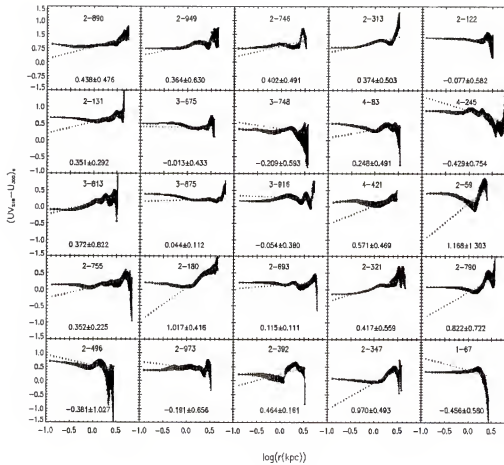

Figure 3–14: Rest-frame $(UV_{218} - U_{300})_0$ logarithmic color profiles for the high redshift sample with photometric redshifts in the HDF-N. The thickness of the line represents the correlated statistical errors. The dotted line represents a weighted least-squares fit to the profile starting from 0.14 arcseconds outwards. Included are the galaxy IDs and the value of the color gradients determined from the least-squares fit with their associated errors. The errors include the uncertainties from the fits and the 1 σ uncertainty due to the systematic background subtraction.

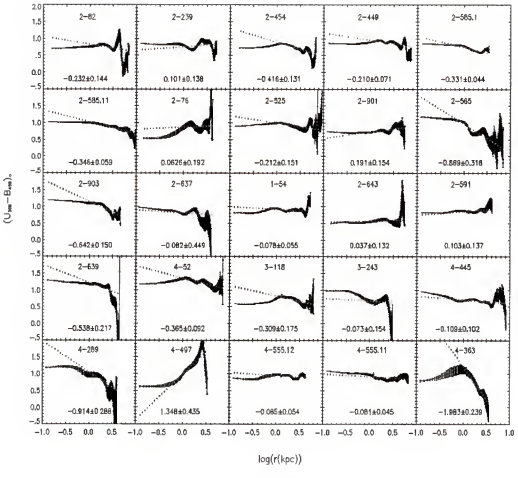

Figure 3-15: Rest-frame $(U_{300} - B_{450})_0$ logarithmic color profiles for the high redshift sample identified by spectroscopic redshifts in the HDF-N. The thickness of the line represents the correlated statistical errors. The dotted line represents a weighted least-squares fit to the profile starting from 0.14 arcseconds outwards. Included are the galaxy IDs and the value of the color gradients determined from the least-squares fit with their associated errors. The errors include the uncertainties from the fits and the 1 σ uncertainty due to the systematic background subtraction

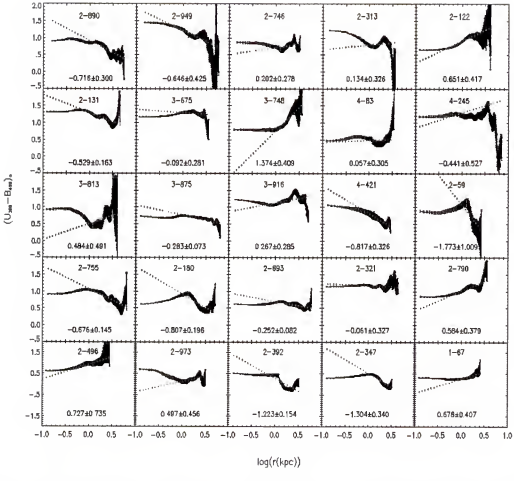

Figure 3–16: Rest-frame $(U_{300} - B_{450})_0$ logarithmic color profiles for the high redshift sample identified by photometric redshifts in the HDF-N. The thickness of the line represents the correlated statistical errors. The dotted line represents a weighted least-squares fit to the profile starting from 0.14 arcseconds outwards. Included are the galaxy IDs and the value of the color gradients determined from the least-squares fit with their associated errors. The errors include the uncertainties from the fits and the 1 σ uncertainty due to the systematic background subtraction

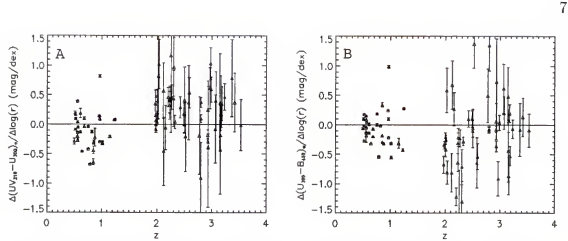

Figure 3–17: Redshift versus rest-frame color gradients of galaxies in the HDF-N. A) Redshift versus rest-frame $(UV_{218} - U_{300})_0$ color gradients of galaxies in the HDF-N. Error bars indicate the correlated statistical errors from the least-squares fit and the 1 σ uncertainty due to the systematic background subtraction for all the galaxies. B) Redshift versus rest-frame $(U_{300} - B_{450})_0$ color gradients with error bars indicating the correlated statistical errors from the least-squares fit and 1 σ uncertainty due to the systematic background subtraction for all the galaxies.

intermediate-redshifts are relatively shallow, the color changes are gradual across the galaxies. It is worth noting that the gradient in the $(U_{300} - B_{450})_0$ filter is somewhat more shallow than it is in the $(UV_{218} - U_{300})_0$ filter. One possible explanation for the slight difference in slopes seen in the two filter set may be due to the presence of dust. If the centers of galaxies are more obscurred by dust than their outer parts, then the colors will be more red in the center. This might contribute, in part, to the negative color gradients seen in the galaxies. If this is the case, since the $(U_{300} - B_{450})_0$ color profiles will be somewhat less affected by the presence of dust, the gradients should be shallower than those seen in the $(UV_{218} - U_{300})_0$ filter set.

In the case of the high-redshift galaxies, the trends in the $(UV_{218} - U_{300})_0$ color gradients are opposite to what is seen in the $(U_{300} - B_{450})_0$ color gradients. Whereas the $(UV_{218} - U_{300})_0$ color gradients of the majority of the high-redshift galaxies (72%) are positive with a median of 0.351 ± 0.062 mag/dex, the $(U_{300} - B_{450})_0$ color gradients are predominantly negative (66%) with a median of -0.159 ± 0.088 mag/dex. Out of the 36 galaxies that have positive $(UV_{218} - U_{300})_0$ gradients,

mag/dex. Out of the 36 galaxies that have positive $(UV_{218} - U_{300})_0$ gradients, 83% of them have gradients greater than 0.200 mag/dex indicating that there are significant color changes across these galaxies. If these color gradients are due to an age gradient alone, then the blueing seen in the color profiles may be indicative of centrally concentrated star formation. That is, if most of the young stars are born in the central regions of these galaxies, the colors would in general be bluer there. Numerous analyses showed that both present-day disks and spheroids have metallicity gradients with higher metallicities toward the galaxy centers. Such a metal gradient would only strengthen the age gradient needed to make the centers bluer.

Table 3–14: Median rest-frame color gradients of galaxies in the HDF-N

Redshift	$(UV_{218} - U_{300})_0$ (mag/dex)	$(U_{300} - B_{450})_0$ (mag/dex)
$0.5 \leq z \leq 1.2$	-0.123 ± 0.073	-0.060 ± 0.063
$2.0 \leq z \leq 3.5$	0.351 ± 0.062	-0.159 ± 0.088

Albeit there is more scatter in the points at high-redshifts than there are at intermediate-redshifts, the plot of the redshifts versus $(U_{300} - B_{450})_0$ color gradients for both redshift bins are similar to each other. However, the predominantly negative gradients detected may occur for different reasons in the two redshift bins. Since the $(UV_{218} - U_{300})_0$ color profiles of the intermediate-redshift sample are also negative, it is reasonable to say that these gradients are intrinsic to the galaxy and that emission lines do not play a significant role at intermediate-redshifts. At high-redshifts, the predominantly negative color gradients seen in the $(U_{300} - B_{450})_0$ color profiles may indicate the presence of strong emission lnes in the B_{450} passband that are consistent with strong star formation in the central regions of the galaxies. Nebular emission lines such as Hβ λ4861, [OII] λ3727 and [OIII] $\lambda\lambda$ 4959,5007 have been detected in the near-IR spectra of the LBGs (Pettini et al. 1998, 2001; Teplitz et al. 2000a). The spectroscopy revealed that the [OIII] λ5007 line is the strongest with typical values of rest-frame equivalent widths $\sim$ 70-260 Å. At low-redshift,

these emission lines are observed to occur predominantly in the central parts of star forming galaxies. If the same can be said of the galaxies at high-redshifts, then the combination of all the emission lines that show up in the B_{450} band can be strong enough that they dominate the light and cause a reddening of color profiles in the central regions. Thus, although the $(U_{300} - B_{450})_0$ gradients are negative, this does not rule out the presence of a centrally concentrated star forming region since the emission lines that are responsible for the reddening of the profiles in the center of these galaxies would be an indicator of strong star formation there. I will show more evidence of the presence of these emission lines in the HDF-S field since there is rest-frame $(B_{450} - V_{606})_0$ color profiles available. If these emission lines play a significant role in the color profiles of galaxies at high redshifts, then the $(B_{450} - V_{606})_0$ gradients should show opposite trends from the $(U_{300} - B_{450})_0$ gradients.

Since the trends seen in the color profiles of galaxies at intermediate and high-redshifts are different, there is convincing evidence that the color gradients of galaxies evolve over time. Whereas both the $(UV_{218} - U_{300})_0$ and the $(U_{300} - B_{450})_0$ color gradients for the intermediate-redshift sample are predominantly negative, the sign flips from positive to negative between these filter sets in the high-redshift population. In the intermediate-redshift sample, the negative color gradients imply that their star formation regions may be located generally in the outer disks of the galaxies or that the older stellar populations may be located towards the center. At high-redshifts, the $(UV_{218} - U_{300})_0$ color gradients of galaxies are positive while the $(U_{300} - B_{450})_0$ color gradients are negative. Although these two passbands show opposing trends, they can still be consistent with each other. Since the $(UV_{218} - U_{300})_0$ color gradients are relatively free of emission lines, they most likely reflect intrinsic color changes in the continuum across the galaxies. The positive color gradients seen in these passbands indicate that these galaxies have centrally

concentrated star formation. The negative color gradients that are seen in the $(U_{300} - B_{450})_0$ may occur because of the presence of emission lines in the B_{450} filter. Since the emission lines, which are probably located in the centers of these galaxies, are the product of strong star formation there, the conclusion that high-redshift galaxies possess centrally concentrated star formation still holds. Thus, from my analysis, I concluded that there is evolution in the color profiles of galaxies in the HDF-N. When we look further back in time, the star formation regions of the galaxies were more centrally concentrated than they are now.

3.2.2 Hubble Deep Field-South

Since the HDF-N represents only one line of sight, the results could be biased. Thus, to reduce the bias and increase the statistics, I studied the color profiles of galaxies in the southern analog of the HDF-N. One advantage that the HDF-S field has over the HDF-N is the availability of the K_{222} band data which allows for the comparison of color profiles of the low-redshift galaxies with the high-redshift galaxies at longer rest-frame wavelengths. However, since the K_{222} band only reaches depths of ~ 24, I could only reliably fit isophotes to the brightest of the high-redshift galaxies. This limited the sample to 14 high-redshift galaxies that could be studied using this passband. I generated $(V_{606} - I_{814})$ color profiles for 20 low-redshift galaxies and 42 intermediate-redshift galaxies. I generated $(J_{110} - H_{160})$ color profiles for all 20 high-redshift galaxies and $(H_{160} - K_{222})$ color profiles for 14 out of the 20 high-redshift galaxies. At the respective redshifts of the galaxies, these colors translate to the rest-frame $(U_{300} - B_{450})_0$ and $(B_{450} - V_{814})_0$. As in the previous section, I will, from now on, refer to the rest-frame color gradients of the galaxies to avoid confusion. Figures 3-18 and 3-19 show the rest-frame $(B_{450} - V_{814})_0$ and $(U_{300} - B_{450})_0$ color profiles of galaxies in the low and intermediate-redshift sample respectively while Figures 3-20 and 3-21 show the rest-frame $(U_{300} - B_{450})_0$ and $(B_{450} - V_{814})_0$ color profiles of the high redshift sample.

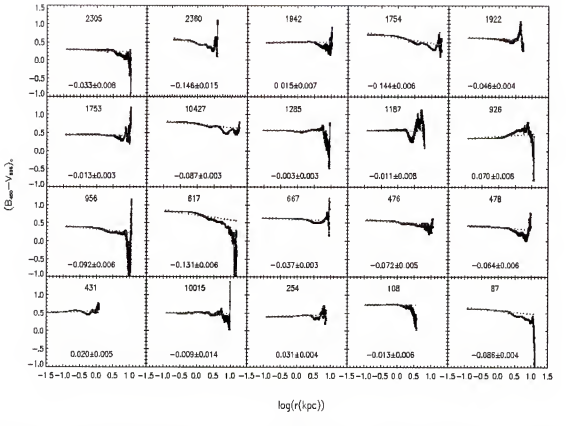

Figure 3–18: Rest-frame $(B_{450} - V_{606})_0$ logarithmic color profiles for the low redshift sample in the HDF-S. The thickness of the line represents the correlated statistical errors. The dotted line represents a weighted least-squares fit to the profile. Included in the plots are the galaxy IDs and the value of the color gradient determined from the least-squares fit with their associated errors. The errors include the uncertainties from the fits and 1 σ uncertainty due to the systematic background subtraction

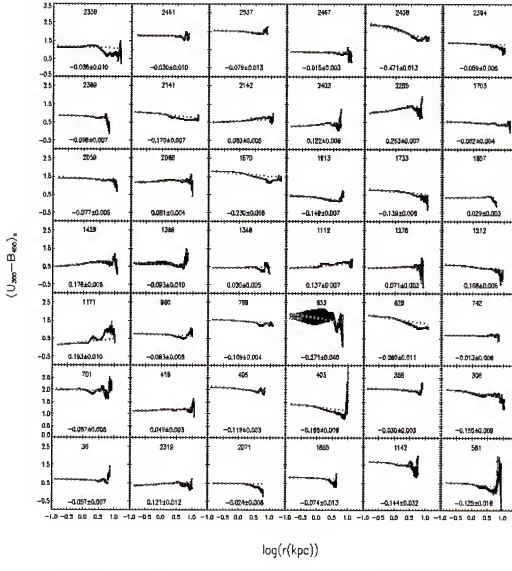

Figure 3–19: Rest-frame $(U_{300} - B_{450})_0$ logarithmic color profiles for the intermediate-redshift sample in the HDF-S. The thickness of the line represents the correlated statistical errors. The dotted line represents a weighted least-squares fit to the profile. Included in the plots are the galaxy IDs and the value of the color gradient determined from the least-squares fit with their associated errors. The errors include the uncertainties from the fits and the 1 σ uncertainty due to the systematic background subtraction

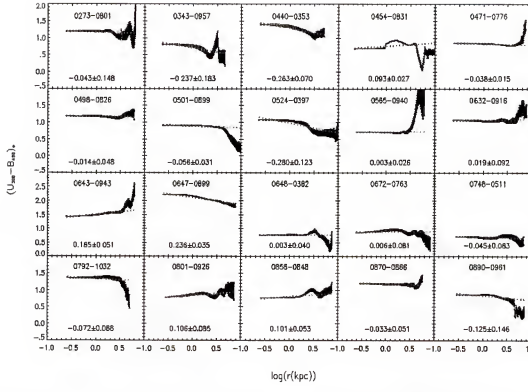

Figure 3–20: Rest-frame $(U_{300} - B_{450})_0$ logarithmic color profiles for the high redshift sample in the HDF-S. The thickness of the line represents the correlated statistical errors. The dotted line represents a weighted least-squares fit to the profile. Included in the plots are the galaxy IDs and the value of the color gradient determined from the least-squares fit with their associated errors. The errors include the uncertainties from the fits and the 1 σ uncertainty due to the systematic background subtraction

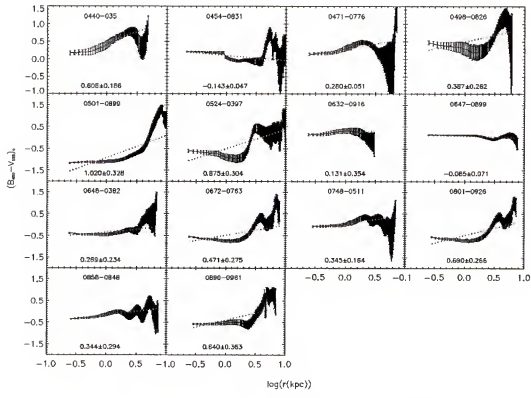

Figure 3–21: Rest-frame $(B_{450} - V_{606})_0$ logarithmic color profiles for the high redshift sample in the HDF-S. The thickness of the line represents the correlated statistical errors. The dotted line represents a weighted least-squares fit to the profile. Included in the plots are the galaxy IDs and the value of the color gradient determined from the least-squares fit with their associated errors. The errors include the uncertainties from the fits and the 1 σ uncertainty due to the systematic background subtraction

Table 3–15: Median rest-frame color gradients of galaxies in the HDF-S

Redshift	$(U_{300} - B_{450})_0$ (mag/dex)	$(B_{450} - V_{606})_0$ mag/dex
$0.5 \leq z < 0.5$	N/A	-0.035 ± 0.020
$0.5 \leq z \leq 1.2$	-0.066 ± 0.021	N/A
$2.0 \leq z \leq 3.6$	-0.035 ± 0.023	0.366 ± 0.103

Figure 3-22 represents a plot of the redshift versus the $(U_{300} - B_{450})_0$ and $(B_{450} - V_{606})_0$ color gradients of the galaxies. Table 3-13 lists their rest-frame median color gradients. The figure and table show that, at low and intermediate-redshifts, the galaxies possess negative color gradients in both these filter sets indicating that the colors are redder towards the center of the galaxy than they are in the outer parts. The median of the gradient in the $(B_{450} - V_{606})_0$ color profiles of the low-redshift sample is -0.035 ± 0.020 mag/dex while the median of the gradients in the $(U_{300} - B_{450})_0$ color profiles of the intermediate-redshift galaxies is -0.066 ± 0.021 mag/dex. As was the case in the HDF-N, the median color gradients in the filters that correlate with longer wavelengths ($(B_{450} - V_{606})_0$ in this case) are shallower than they are at shorter wavelengths. This, again, could be due to the presence of dust. Since extinction would be less at longer wavelengths, the gradients would be shallower there. At high-redshifts, the gradients in the $(U_{300} - B_{450})_0$ color profiles are, in general, opposite in sign to the gradients in the $(B_{450} - V_{606})_0$ profiles. A majority of high-redshift galaxies (60%) possess negative gradients in the $(U_{300} - B_{450})_0$ color profiles with a median of -0.035 ± 0.023 mag/dex, whereas, all but two of the galaxies (86%) possess strong positive gradients in $(B_{450} - V_{606})_0$ with a median of 0.366 ± 0.103 mag/dex.

Whereas the $(U_{300} - B_{450})_0$ and $(B_{450} - V_{606})_0$ color gradients show similar trends at intermediate and low-redshifts respectively, at high-redshifts the trends in these color gradients differ from each other remarkably. In the rest-frame $(U_{300} - B_{450})_0$, the color gradients are predominantly negative, whereas in the rest-frame $(B_{450} - V_{606})_0$, the color gradients are predominantly positive. In the HDF-N, I mentioned that the presence of nebular emission lines may be responsible

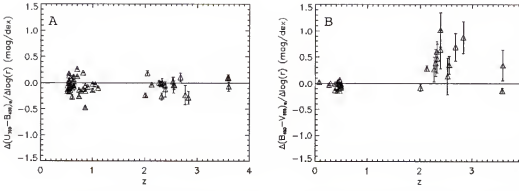

Figure 3–22: Redshift versus rest-frame color gradients of galaxies in the HDF-S. A) Redshift versus rest-frame $(U_{300} - B_{450})_0$ color gradients with error bars indicating the correlated statistical errors from the least-squares fit and the 1 σ uncertainty due to the systematic background subtraction for all the galaxies. B) Redshift versus rest-frame $(B_{450} - V_{606})_0$ color gradients with error bars indicating the correlated statistical errors from the least-squares fit and the 1 σ uncertainty due to the systematic background subtraction for all the galaxies.

for the negative gradients seen in the $(U_{300} - B_{450})_0$ color profiles at high-redshifts. In the HDF-S, one notices similar trends in the $(U_{300} - B_{450})_0$ color profiles of galaxies at high-redshifts. As I mentioned in the Section 3.2.1, if emission lines really contribute significantly to the color profiles, then their effects should be apparent in the $(B_{450} - V_{606})_0$ color profiles. If they are responsible for the reddening seen in the centers of the $(U_{300} - B_{450})_0$ profiles, then they should be partly responsible for the blueing seen in the centers of the $(B_{450} - V_{606})_0$ profiles. As predicted, the $(B_{450} - V_{606})_0$ profiles show very strong positive gradients in the high-redshift sample. Although some emission lines such as Hβ and [OIII] $\lambda\lambda$ 4959,5007 will appear in the V_{606} rest-frame passband at some redshifts, apparently they are not as dominant as those appearing in the B_{450} rest-frame passband or the galaxies may possess strong, intrinsic positive color gradients. I believe it to be a combination of the two. I have demonstrated that the high-redshift galaxies in the HDF-N possess intrinsic positive gradients in their $(UV_{218} - U_{300})_0$ color profiles which are relatively unbiased by emission lines. Thus, it is not surprising to observe the strong gradients in an overwhelming majority of the $(B_{450} - V_{606})_0$

profiles. The typical gradients seen in the $(B_{450} - V_{606})_0$ profiles (0.366 mag/dex) are slightly stronger than the typical gradients seen in the $(UV_{218} - U_{300})_0$ (0.352 mag/dex) color profiles. If the LBGs do possess inherent positive gradients which is due to centrally concentrated star formation, then the presence of emission lines in the B_{450} passband will act to enhance the positive gradients further. Given the occurrence of these two phenomena, it is not surprising that such strong gradients are detected in the $(B_{450} - V_{606})_0$ profiles.

3.2.3 Hubble Deep Field-North vs. Hubble Deep Field-South

Unfortunately, an ideal comparison of the color gradients of high-redshift galaxies in the HDF-N and HDF-S cannot be made since the filter sets of the two fields do not overlap completely. Ideally it would have been useful to compare the $(I_{814} - J_{110})$ (rest-frame $(UV_{218} - U_{300})_0$) color gradients since strong emission lines, that can potentially introduce bias to the results, do not show up in these filter sets. I was able to generate $(I_{814} - J_{110})$ color profiles for galaxies in the HDF-N since there was complementary NICMOS data to go with the WFPC-2 data, but I was not able to generate $(I_{814} - J_{110})$ color for galaxies in the HDF-S since the NICMOS data was taken in parallel mode with WFPC-2 and, consequently, was not at the same pointing as WFPC-2. Furthermore, I could not compare the $(H_{160} - K_{222})$ (rest-frame $(B_{450} - V_{606})_0$) color profiles since they were only generated for the HDF-S. The only color profiles that were generated for both the HDF-N and HDF-S fields were $(J_{110} - H_{160})$ profiles, which translate to rest-frame $(U_{300} - B_{450})_0$ at the redshifts of the Lyman-break galaxies. Thus, the direct comparisons that I am able to make between the HDF-N and HDF-S will involve the rest-frame $(U_{300} - B_{450})_0$ color profiles.

Figure 3-23 shows the plot of the redshifts versus the rest-frame $(U_{300} - B_{450})_0$ gradients of galaxies in the intermediate and high-redshift sample in the HDF-N (asterisks) and HDF-S (triangles). In the high-redshift sample, the median

$(U_{300} - B_{450})_0$ gradient is -0.159 mag/dex for the HDF-N and -0.0352 mag/dex for the HDF-S. At intermediate-redshifts, the scatter of points in the plot as well as the medians (~ 0.06 mag/dex) are remarkably similar in the HDF-N and HDF-S. Although the $(U_{300} - B_{450})_0$ gradients of the high-redshift galaxies are predominantly negative in both the HDF-N and HDF-S, there seems to be a systematic difference. The scatter in the points for the HDF-N is much higher than it is in the HDF-S. This is probably caused by the uncertainty in the background subtraction in the two datasets. Since the galaxies are fainter at higher redshifts, the differences are more noticeable in the color gradients at high-redshifts. Also, since the NICMOS data from the HDF-S was about one magnitude deeper than the data for the HDF-N, the errors in the background subtraction for the HDF-S will be less in the rest-frame $(U_{300} - B_{450})_0$. This could explain the smaller scatter seen in the color gradients of galaxies in the HDF-S.

Although different filter sets were probed in the HDF-N and HDF-S, it is reassuring that the trends seen in the two fields are consistent with each other. This helps to validate the conclusions. In both the HDF-N and HDF-S, we saw that galaxies at low and intermediate-redshifts typically possess negative gradients in all the filter sets and that the sign of the color gradients of galaxies at high-redshifts flipped from one filter set to the next. Since these trends applied to all galaxy types, they show that there may be evolution in the distribution of the star formation regions in the entire population of galaxies. At high-redshifts, the star formation regions are probably located near the centers of the galaxies; while at low and intermediate-redshifts, the star formation regions are predominantly located in the outer parts of the galaxies.

3.2.4 Discussion

Not much is currently known about the ultraviolet color gradients of galaxies in the local universe. The few studies of this kind were conducted using the

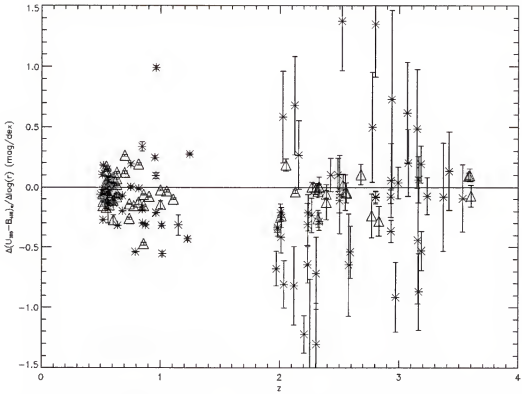

Figure 3–23: Redshift versus rest-frame $(U_{300} - B_{450})_0$ of the intermediate-redshift and high-redshift galaxies in the HDF-N (asterisks) and HDF-S (triangles). Error bars indicate the correlated statistical errors from the least-squares fit and the 1 σ uncertainty due to the systematic background subtraction for all the galaxies.

information from the images taken with the Ultraviolet Imaging Telescope during the Astro-1 and 2 missions (O'Connell et al. 1992; Ohl et al. 1998). From the Astro-1 mission, O'Connell et al.(1992) analized the (152-249) color profiles of two Sb bulges and two E galaxies that were generated from the images taken with the 152 nm and 249 nm filters. They concluded that all but M32 exhibited prominent positive gradients in their profiles. In their study of the $FUV(1500\text{Å}) - B$ color profiles for eight early-type galaxies, Ohl et al. (1998) found, again, that all but M32 exhibited large positive color gradients, with differences in color greater than 1.0 mag over the entire profile. These large ultraviolet color gradients are reflective of the "UV upturn" or "UVX" population that have been observed in the far-UV (1200 Å $< \lambda <$ 2000 Å) imaging of local spiral bulges and early-type galaxies

(Code 1979; de Boer 1982). They propose that a combination of an increase in metallicity combined with the existence of older stellar populations may contribute in producing these color gradients. The trends in the far-UV color gradients of these galaxies are in the opposite sense to what is observed in the rest-frame near-UV for the majority of the low and intermediate-redshift galaxies in the HDF-N sample that have been observed in the optical and near-IR. However, since the study of the far-UV color profiles of local galaxies were conducted at shorter wavelengths; and given that the sample sizes were much smaller and limited only to early-type systems and spiral bulges, it is difficult to compare their results with this study. Thus, more observations of local galaxies in the ultraviolet are needed to fairly compare with the sample of galaxies at intermediate and high-redshifts in this study.

In general early-type galaxies at low and intermediate-redshifts have been found to exhibit negative gradients in the rest-frame optical color profiles; i.e., they have redder colors in the center and gradually become bluer outwards (Franx et al. 1989; Peletier et al. 1990; Tamura & Ohta 2000; Tamura et al. 2000; Vader et al. 1988). In their study of the $(V_{606} - I_{814})$ color profiles of 10 elliptical galaxies in the HDF-N from $z = 0.1 - 1.0$, Tamura et al. (2000) observed the same trends. They found that all but two (one of them being galaxy 2-251 in our sample) exhibited redder colors towards the centers. At $z = 0$, both an age and a metallicity gradient in the stellar populations can be responsible for producing the negative color gradients observed in the galaxies; i.e., the galaxy colors are redder in the center than in the outer parts because they either have older stellar populations or higher metallicities there. This age-metallicity degeneracy makes it difficult to determine the cause of the color gradient. To break the degeneracy, they generated two model gradients that reproduced typical color gradients of elliptical galaxies at $z = 0$: one that was caused by a metallicity gradient of old stars, and the other that was

caused by an age gradient of stars with the same metallicity. They then evolved these models to the redshifts of their observed galaxy sample. By comparing the model gradients with the observed gradients, they concluded that the model involving the metallicity gradient agreed well with observations at all redshifts whereas the model involving the age gradient was only in good agreement up to a redshift of $z \sim 0.3$. The $(V_{606} - I_{814})$ (rest-frame $(U_{300} - B_{450})_0$) color profiles for the galaxies in my intermediate-redshift sample also revealed the same trends in the color gradients. Over half (17/27 in the HDF-N and HDF-S) of the intermediate-redshift galaxies possessing $r^{1/4}$ profiles exhibit negative color gradients. Thus, one may interpret the central reddening in the color profiles of the elliptical galaxies in the intermediate-redshift sample in the Hubble Deep Fields as being due primarily to a metallicity gradient; the centers of the galaxies have higher metallicities than in the outer parts.

I observed the same negative trend in the color gradients for the majority (18/32 in the HDF-N and HDF-S) of the intermediate-redshift galaxies that I classified as having exponential profiles. In the study of the near-IR and optical color profiles of 86 face-on disk dominated galaxies, de Jong et al. (1996) concluded that their negative color gradients were best reproduced by models involving both stellar age and metallicity gradients. Therefore, I interpret the gradients seen in the late-type galaxies as arising because of age and metallicity effects; the central parts of the galaxies in general have older stars and higher metallicity than the outer parts causing them to have redder colors towards the centers.

Whereas the trends seen in the color profiles of the intermediate-redshift sample are well understood, one cannot say the same for the high-redshift sample. Since this is the first study of its kind to be conducted on galaxies with $z \geq 2.0$, there are no other high-redshift observations of color profiles to compare the results with. Thus, I attempt to account for the positive gradients seen in the high-redshift

sample by understanding what is responsible for producing similar trends in the color profiles seen at intermediate and low-redshifts.

Guzmán et al. (1998) generated rest-frame $(B - V)$ color profiles for five compact narrow emission line galaxies (CNELGs), which are low mass ($M \leq 10^{10}$ $M_{\odot}$) starburst systems seen at $z \leq 1.0$ and are similar to nearby HII galaxies. They noticed that, although the gradients were not significant, there was a slight trend for the bluest color to occur in the central regions. On average, they found that the color inside the half-light radius was 0.14 ± 0.05 mag bluer than it was outside the half-light radius. Guzmán et al. (1998) described CNELGs as having either compact cores, fans and tails, or several small compact regions. These morphologies are along the lines of what is observed in the HDF high-redshift sample. Furthermore, they determined that their half-light radii span from $1 - 5$ kpc ($H_0 = 50 kms^{-1}Mpc^{-1}$, $q_o = 0.1$). This matches the range seen in the half-light radii of the galaxies in my high-redshift sample. Given that the morphologies, half-light radii, and color profiles of LBGs are similar to what is observed in the CNELG sample, it is not unreasonable to believe that LBGS could be the high-redshift, high-luminosity analogs of the lower redshift CNELGs.

In their study of the dispersion in the internal colors of faint spheroidals with $0 \leq z \leq 1$ in the HDF-N and HDF-S, Menanteau et al. (2001) found that over 30 per cent of the galaxies show significant dispersions in their $(V_{606} - I_{814})$ colors. For the majority of the cases, the inhomogenieties seen in the galaxies of the HDF-N are such that bluer colors are detected in the core. They suggested that these inhomogeneities are due to a recent burst of star formation. Furthermore, by using a spectral synthesis model and maximum likelihood method developed by Abraham et al. (1999), they found that the burst of star formation happened during short timescales, lasting less than 1 Gyr.

These studies showed that the blue colors detected in the cores of the intermediate and low-redshift galaxies may be caused by a recent starburst. If the same can be said of galaxies at high-redshifts, then the strong positive color gradients detected in this study may also be caused by a centrally concentrated starburst. From an analysis of broadband optical and IR spectral energy distributions for 17 LBGs, Sawicki and Yee (1998) also found that star formation is episodic rather than continuous in these systems, and that their stellar population is very young, with a median age of $\sim$ 25 Myr. The high star formation rates that have been detected in these Lyman-break galaxies (Pettini et al. 1998, 2001; Sawicki and Yee 1998; Steidel et al. 1995) further support the idea of a central starburst. Starbursts can be triggered by several mechanisms including mergers and interactions (Barnes and Herquist 1996; Hernquist and Mihos 1995; Mihos and Hernquist 1994a, 1996; Somerville et al. 2000), bar instabilities (Shlosman et al. 1990), and SNe and stellar winds (Heckman et al. 1990). Since the volume of the high-redshift universe is smaller than it is now, mergers have been implied to be the cause of the enhanced star formation. In Chapters 5 and 6, I argue that these starbursts are likely a byproduct of galaxies that are in the final stages of merging.

CHAPTER 4
SOURCES OF UNCERTAINTIES

Whenever the faint, high-redshift population are analyzed, sources of uncertainties must be discussed to give a fair representation of the robustness of the trends observed before they can be generalized to the universe as a whole. These uncertainties included the correlation of the pixels, the determination of the sky background, the role of dust, and observational selection effects.

4.1 Correlation of Pixels

Since the images have been drizzled, convolved to recover approximately the same resolution as the image with the poorest resolution, and fitted with ellipses at 0.1 pixel increments, the errors that are obtained from the photometry will be correlated because of the oversampled pixels. These photometric errors will be underestimated since correlation tends to reduce the errors. Thus, when I performed a weighted least-squares fit to the color profiles and fits to the surface brightness profiles, the error bars used in the determination of the weights were correlated. Consequently, the parameters that were obtained from the fits may differ from what would be measured if the errors had been independent. To understand how the correlated errors in the photometry affect the fit to the surface brightness profiles and the least-squares fitting to a straight line, I obtained weight images for the HDF-S and rms images for the HDF-N (Dickinson, 2003 private communication) in the passbands of interest. For the HDF-S fields, I obtained the value of the rms by taking the inverse square root of the weight images. Since the weight maps for the HDF-S NICMOS field quantify the noise in a single input pixel, I multiplied the rms values by scale^2 (where scale= 0.36974) to obtain the noise in a single output pixel produced by the "drizzling" method. The scale

parameter in DRIZZLE was set to create an output pixel size of 0.″075 for the HDF-S NICMOS field. The resulting rms values from these images quantify the uncertainty of the noise in the background (sky + readout noise + dark current) before any processes were performed to cause interpixel correlations. I re-analyzed the sample of galaxies from the low, intermediate, and high-redshift sample using these images. With the same set of ellipses that I used in the surface photometry, I replaced the correlated errors with the "true" uncorrelated errors for each galaxy. In doing so, I have chosen to neglect the poisson noise from the galaxies themselves since they are so faint that it would be insignificant compared to the background noise. I then repeated the surface brightness and color analysis on the galaxies and compared the results from the fits weighted by independent errors to those weighted by correlated errors.

From the comparisons, I found that, the results from the surface brightness profiles and color gradients remain approximately the same in the HDF-N. The errors in the estimation of the Sérsic indices were higher in the profiles that were fitted using independent error bars, but this did not affect the results from the fits significantly. At high-redshifts, these errors were ~ 7 times higher whereas at intermediate-redshifts, these errors were ~ 2 times higher. At all redshifts, both the value of and the errors in the color gradients obtained from the fits weighted by independent errors were (on average) very similar to those weighted by correlated errors. In the HDF-S, the results from the fits to the surface brightness profiles at all redshifts did not differ significantly. However, the errors from the fits were higher in the profiles weighted by independent errors. The errors in the Sérsic indices were ~ 1.7 times higher in the intermediate-redshift sample and ~ 3.5 times higher in the high-redshift sample. The color gradients estimated using the independent errors were somewhat larger in magnitude than those estimated using the correlated errors. The magnitude of the color gradients changed by at most, an

average factor of ~ 2.5 at low-redshifts, ~ 1.3 at intermediate-redshifts, and ~ 1.8 at high-redshifts. The errors in the color gradients were a factor of ~ 1.3 higher at low and intermediate-redshifts and ~ 1.6 at high-redshifts. However, despite the differences, the results did not change much since the signs of the color gradients remain the same. Given that the signs of the color gradients and the values of the Sérsic indices remained (approximately) the same after accounting for noise correlation, I conclude that the results from the surface photometry of galaxies in the HDF-N and HDF-S still hold.

4.2 Uncertainties due to Background Subtraction

While statistical errors dominating the inner parts of the color profiles and PSF effects contribute to the uncertainty in the least-squares fit, the systematic errors due to sky subtraction dominate in the outer parts of the profile especially at high-redshifts. To understand how the value of the color gradients are affected by sky subtraction, I determined both a lower and upper limit in the estimation of the sky background for the galaxies in the HDF-N and HDF-S by subtracting and adding 1 σ to the background values. I then repeated the color analysis to determine the color gradients for the four possible combinations of sky subtraction. For example, to determine the scatter in the $(I_{814} - J_{110})$ color gradient due to the uncertainty in the background, I would calculate the gradients that resulted from subtracting off: (1) the upper limit in I_{814} and the upper limit in J_{110} (I+, J+), (2) the upper limit in I_{814} and the lower limit in (I+, J−), (3) the lower limit in I_{814} and the upper limit in J_{110} (I−, J+), and (4) the lower limit in I_{814} and the lower limit in J_{110} (I−, J−). I then calculated the error in the background subtraction by determining the rms deviation between the color gradients obtained by subtracting off the four possible combination of sky subtraction and the color gradients obtained by subtracting off the original background value. The 1 σ errors in the sky background subtraction were added in quadrature to the errors in the

color gradients reported for all the galaxies in both the HDF-N and HDF-S sample. The average error in the color gradients due to the background subtraction in the HDF-N and HDF-S are listed in Tables 4-1 and 4-2 respectively.

Table 4–1: Average background subtraction errors in the HDF-N

Redshift	$\mathrm{err}(UV_{218} - U_{300})_0$	$\mathrm{err}(U_{300} - B_{450})_0$
$0.5 \leq z \leq 1.2$	0.024	0.013
$2.0 \leq z \leq 3.5$	0.373	0.253

Table 4–2: Average background subtraction errors in the HDF-S

Redshift	$\mathrm{err}(U_{300} - B_{450})_0$	$\mathrm{err}(B_{450} - V_{606})_0$
$0.5 \leq z < 0.5$	N/A	0.005
$0.5 \leq z \leq 1.2$	0.004	N/A
$2.0 \leq z \leq 3.6$	0.073	0.225

For the intermediate-redshift sample in the HDF-N, the average 1 σ deviation was ~ 0.024 mag/dex in the $(UV_{218} - U_{300})_0$ color gradients and ~ 0.013 mag/dex in the $(U_{300} - B_{450})_0$ color gradients. In the HDF-S, the average 1 σ deviation was ~ 0.004 mag/dex in the $(B_{450} - V_{606})_0$ color gradients at low-redshifts and ~ 0.005 mag/dex in the $(U_{300} - B_{450})_0$ color gradients at intermediate-redshifts. The median color gradients for the four different sky subtraction combinations were all negative. This shows that the results from the intermediate and low-redshift sample are robust. The same cannot be said for the high-redshift sample which are much fainter and, consequently, more prone to high fluctuations in the color gradients due to the errors in sky subtraction. As expected, the errors in the background subtraction in the high-redshift sample were much higher than they were in the intermediate and low-redshift samples. In the HDF-N, the average 1 σ deviation was ~ 0.373 mag/dex in the $(UV_{218} - U_{300})_0$ passband and ~ 0.253 mag/dex in the $(U_{300} - B_{450})_0$ passband. Although the errors are high, in general, the sign in the median color gradients obtained by applying the different combinations of sky subtraction remain the same. In both filter sets, the sign in the median color gradients changes for only one combination.

Since the HDF-S NICMOS field was 1 magnitude deeper than the HDF-N field, the errors in the background subtraction of the rest-frame $(U_{300} - B_{450})_0$ color gradients were less than in the HDF-N. In the HDF-S, the average 1 σ deviation was ~ 0.073 mag/dex in the $(U_{300} - B_{450})_0$ passband and ~ 0.225 mag/dex in the $(V_{606} - I_{814})_0$ passband. Although the errors in the background subtraction in the $(U_{300} - B_{450})_0$ filter set were relatively small, the sign changed in the median color gradients of two out of the four combinations of background subtraction. However, since the median in the color gradients was small (-0.035 mag/dex), it is not too surprising to have the sign fluctuating around zero. Despite the high errors detected in the $(V_{606} - I_{814})_0$ passband, the conclusion that positive gradients dominate in this filter set is robust since the sign in the median color gradients obtained by applying all four combinations of sky background do not change.

The analysis of the uncertainties in the background subtraction showed that the results from the color gradient analysis for the galaxies at low and intermediate-redshifts are robust. As to be expected, the results for the galaxies at high-redshifts have higher uncertainties and are less robust. However, I have demonstrated that these errors do not change the results significantly.

4.3 Dust Obscuration

In theory, dust can cause the color profiles of galaxies to be redder towards the center if we assume that the dust would be more concentrated at the center and would produce more extinction there (Byun et al. 1994; de Jong et al. 1996; Evans 1994). De Jong (1996) conducted Monte Carlo simulations of light rays traveling through a dusty medium to understand to what extent dust can affect color gradients in late-type systems. They concluded that although a fraction of the color gradients could be attributed to dust, an additional explanation is needed to account for the total reddening in the system. Wise et al. (1996) produced color profiles extincted by dust for a set of model ellipticals from the U to the

K passband and compared them with 52 early-type galaxies from the literature. They concluded that if dust is the primary cause of color gradients in the early-type sytems, then the dust must be spatially extended ($\rho_d \propto r^{-1}$) implying high dust masses comparable to the dust masses inferred by the IRAS data. Thus, the presence of dust may be partly responsible for producing the negative color gradients seen in the intermediate-redshift sample for both early-type and late-type systems; however, given that the total mass of the dust and its spatial distribution are not well constrained, it is not presently known to what degree dust affects the color distribution in the galaxies. On the other hand, even though dust might play a role in the high-redshift sample, there is no reason why its presence would cause the color profiles to be bluer towards the center. As previously mentioned, dust would tend to cause extinction and, thus, reddening towards the center, not the outer parts of early-type galaxies. If dust played a role in the positive color gradients detected in the majority of galaxies with $r^{1/4}$ profiles at high-redshifts, it would be to suppress the intrinsic color gradients, not to enhance them. Thus, although dust may be partly responsible for the trends in the color gradients seen at intermediate-redshifts, it cannot explain the trends seen at high-redshifts.

4.4 Selection Effects

Anytime we compare observations of galaxies in two different redshift ranges, we must take into account the effect of observational selection. At high redshifts, only those galaxies with the highest luminosities and surface brightnesses can be detected and studied; thus, any trends that are detected in the surface brightness and color profiles may potentially be affected by this bias. I have tried to minimize some selection effects by observing the galaxies at different redshifts in the same rest-frame wavelengths. Furthermore, at high-redshifts I sample not only galaxies with spectroscopic redshifts, but also galaxies with photometric redshifts which are, in general, fainter than those galaxies that can be detected spectroscopically. Thus,

I am including in my sample, the fainter population at high-redshifts and not just the UV luminous galaxies.

Wu (1999) performed simulations on galaxies in the HDF-N to understand the selection effects that may arise when studying galaxies at different redshifts. She takes the galaxies with $0.75 \leq z \leq 1.2$ in the F814W band and simulates their appearance at $z = 1.5$ and $z = 2.3$ by using the corresponding images in F606W and F450W filters respectively to minimize K-corrections. She found that at $z = 1.5$ only 33% of the original objects can still be detected and by $z = 2.3$, only 3% of them remain. To further understand the sampling of the galaxy population as a function of redshift, she defines a concentration versus asymmetry index ($A_W - C_W$). She plots the $A_W - C_W$ relation for galaxies in the HDF-N separating them into five redshift bins with redshifts ranging from $z \leq 0.6$ to redshifts $z > 3.0$. From these plots, she concluded that the range of A_W and C_W values remain constant for $z < 1.2$, but that at higher redshifts, the number of high C_W objects seem to decrease while the number of high A_W objects seem to increase. Since high concentration is associated with early-type systems such as ellipticals and early-type spirals and high asymmetry is associated with late-type and merging systems, it seems from her plots that at $z > 1.2$, there is a decrease in the early-type systems and an increase in the late-type and merging systems. However, she shows in her work, that these trends can naturally be explained by selection effects. In her simulations she has shown that, by $z = 2.3$ most of these galaxies with high concentration have faded so much that they "disappear" into the noise and can no longer be detected.

From Wu's (1999) discussion it is quite possible that the trends that are seen in the surface brightness profiles may be influenced by these selection effects. These selection effects may have been responsible for the increase in A_W objects with redshift detected by Abraham et al. (1996) and Corbin et al. (2001). If I had

not taken into account the smearing due to the PSF, I would have seen the same decrease in early-type systems in my study. For example if I had only inspected the Sérsic indices of the galaxies in the HDF-N and ignored the effect of PSF smearing, I would naively classify 5 out of a total of 32 (16 $\pm$ 7%) of the galaxies in the intermediate-redshift sample and only 1 out of the 20 (5 $\pm$ 5%) galaxies with H $\leq$ 24.5 in the high-redshift sample as possessing an $r^{1/4}$ profile. Thus, it would seem that the number of early-type systems had decreased with redshift. However, since I have corrected for the effect of the PSF, I was able to recover the number of galaxies with $r^{1/4}$ profiles (i.e., 28 $\pm$ 9% for the intermediate-redshift sample and 60 $\pm$ 15% in the high-redshift sample). Thus, by correcting for the PSF, I took care of one selection effect. However, at $z > 2$, we are still sampling only the tip of the surface brightness function where asymmetries are more evident. Consequently, it is not surprising that there is a slightly higher fraction of irregular galaxies in the high-redshift sample, 20 $\pm$ 10% as opposed to 6 $\pm$ 3% in the intermediate-redshift sample. Although the selection effects may partly be responsible for some of the trends seen in the morphological classification of galaxies, they cannot explain the trends that exist in the color profiles. They cannot explain why, at high-redshifts, there exists a significant population of galaxies possessing large positive color gradients but at lower redshifts, they seem to "disappear".

CHAPTER 5
COMPARISONS WITH THEORETICAL MODELS

In the last several years, much advancement has been made in the observational regime since many have used the Lyman-break technique (Steidel and Hamilton 1993) to reliably detect galaxies at high-redshift in large numbers. With the detection of numerous high-redshift galaxies at high resolution and sensitivities, it is now feasible to compare observations with theoretical predictions. In this study, I probed the surface brightness profiles and color profiles of galaxies spanning a wide range of redshifts to place constraints on galaxy formation and evolution. From the surface brightness analysis of the galaxies in the HDF-N, I found that the majority of Lyman-break galaxies possess $r^{1/4}$ profiles and may harbor starbursts in their central regions. Although the results may be affected by uncertainties and selection effects, it is still useful to compare the observations with models to test for consistency and determine the driving force behind the trends seen if they are at the very least attributed to galaxy evolution.

N-body simulations and semi-analytic modeling of dark matter halos demonstrated that structure builds up into larger and larger units through continual accretion and merger (Baugh et al. 1998; Cole at al. 1994; Kauffmann et al. 1997; Roukema et al. 1997; White and Frenk 1991). These models gave support to the "hierarchical clustering" scenario pioneered by Peebles (1970), which is a less restricted version of the standard cold dark matter (CDM) model since it allows for the assumption of different cosmologies. Currently, this model represents the popular framework for how structure formed and evolved in the universe. To understand how my results fit in the overall picture of galaxy formation and evolution, I compared my observations of galaxies in the Hubble Deep Fields with

the predictions from the models of galaxy formation and evolution within the hierarchical clustering scenario explored by BCFL98 and SPF01.

5.1 Comparisons with the BCFL98 Model

In their model, BCFL98 used a Monte Carlo simulation to generate binary merger trees, which essentially describe the merging histories for dark matter halos with predetermined final masses. They generated the mock high-redshift progenitors by applying the selection criteria for Lyman-break candidates described in Steidel and Hamilton (1993) and quantified the amount of cold gas available by measuring the rate at which cold gas in thin shells can cool to form stars. They chose values for the star formation timescale, the feedback parameter, the shape of the initial mass function (IMF), the overall luminosity normalization, and the merger timescale for galaxies which would best reproduce the local B and K band luminosity functions. Lastly, they fixed the threshold mass for a galaxy merger causing a disk to become a spheroid to match the relative population of ellipticals, S0's, and spirals locally. They produced their model for three different cosmologies: the standard CDM model ($\Omega_0 = 1$, $h = 0.5$, $\sigma_8 = 0.67$), the flat CDM model ($\Omega_0 = 0.3$, $\Lambda_0 = 0.7$, $h = 0.6$, $\sigma_8 = 0.97$), and the open CDM model ($\Omega_0 = 0.4$, $h = 0.6$, $\sigma_8 = 0.68$).

From their simulations, BCFL98 showed that present-day galaxies that make up the bright end of the luminosity function have at least one Lyman-break progenitor at $z \sim 3$. Furthermore, depending on their merging histories, these Lyman-break progenitors can end up as a $L > L*$ galaxy with any morphological type. If they experienced major mergers at recent epochs they may evolve to become ellipticals and S0s. If they grew by the quiescent accretion of cooling gas, the gas might form a disk around a bulge that was created by an earlier merger event. And if they experienced minor mergers which are too weak to destroy the disk, they might accumulate more stars in the central bulge. They expected the

Lyman-break galaxies to be rotating disks with typical half-light radii $\sim 0.5h^{-1}$ kpc and predicted that the stars of the progenitors will congregate primarily in the central regions. Baugh et al. (1998) additionally concluded that the star formation of galaxies at all redshifts occurs quiescently with star formation rates that never obtain a value higher than a few solar masses per year.

Their conclusions match the observations of LBGs only if internal dust extinction is ignored. However, in reality, the effect of dust is probably non-negligible, although how much of a role it plays is still presently uncertain. Pettini et al. (1997) measured the extinction to be a factor of ~ 3 at 1500Å , whereas Meurer et al. (1997) and Sawicki and Yee (1998) reported values closer to $15 - 20$. Now the general consensus is to use an extinction correction of ~ 5 (Meurer et al. 1999; Steidel et al. 1998). The conclusion reached by BCFL98 that LBGs are forming their stars quiescently in an extended disk is not consistent with the results from this study since the strong positive color gradients seen in the rest-frame $(UV_{218} - U_{300})_0$ profiles seems more indicative of a strong central starburst. Furthermore, the results from the morphological classification in this study showed that the majority of these galaxies possess $r^{1/4}$ profiles rather than disk profiles.

5.2 Comparisons with the SPF01 Model

The results from SPF01 are in better agreement with the trends that were observed in the color profiles in this study and with the high star formation rates detected in the LBGs. Instead of undergoing quiescent star formation, they favor the idea that LBGs are experiencing what they term as "collisional starbursts", which describe starbursts that are induced by galaxy-galaxy mergers. Somerville et al. (2001) explained that they obtain different results from BCFL98 because of the different assumptions made in the two models. The assumptions made in BCFL98 for supernovae feedback, gas cooling, and types of mergers were such that, taken in combination, would act to suppress star formation at early epochs. Also they

claimed that the BCFL98 models only agree with observations if dust extinction is not taken into account in their modeling.

Somerville et al. (2000) used a semi-analytic modeling of galaxies in the CDM hierarchical clustering framework adopting the ΛCDM cosmology ($\Omega_0 = 0.3$, $\Omega_\Lambda = 0.7$, $h = H_0/(100 kms^{-1} Mpc^{-1}) = 0.7$, $\sigma_8 = 1.0$) to understand the nature of Lyman-break galaxies. Their models took into account the effects of the cooling rate of gas, supernovae feedback, galaxy-galaxy mergers, and star formation and subsequent evolution. They addressed the effects of dust extinction by following the recipe described in Wang and Heckman (1996) for nearby starbursts which returns the optical depth for a given extinguished UV luminosity, intrinsic UV luminosity, and face-on optical depth. They generated Monte-Carlo based merger trees in which each branch in the tree is associated with a merger. Within this framework, they considered three different models to represent the variety of star formation events. The "collisional starburst" model is one in which star formation occurs quiescently with additional star formation occurring in bursts. The "constant efficiency quiescent" model only involves quiescent star formation with no bursts. And the "accelerated quiescent" model involves quiescent star formation but with the star formation rate increasing with look-back time.

They concluded that among the three models, the "collisional starburst" model best reproduces the observations of the LBGs including comoving number density, star formation rates, internal velocity dispersions and the observed luminosity function, global star formation rate density, and cold gas and metallicity abundances in the Universe. Thus, they advocated that star formation occurred at a higher rate in the high redshift universe and that mergers were responsible for increasing the star formation rate by triggering gas inflow to the central regions. According to this scenario, LBGs are not yet fully assembled and are experiencing mergers that ignite starbursts in their central regions. And because

they are experiencing mergers, they should possess highly disturbed morphologies. The strong positive color gradients that are detected in this study are consistent with the view that these galaxies are forming their stars via a burst triggered by galaxy mergers. However, I detected a lower fraction of galaxies with irregular morphologies than is predicted by this theory. Thus, it is still difficult to determine whether LBGs represent star forming clumps that could grow more massive by experiencing more mergers or whether they are the fully assembled direct progenitors of today's $L*$ galaxies.

CHAPTER 6
THE NATURE OF LYMAN-BREAK GALAXIES REVISITED

Now that I have analyzed the data and compared my observations with results from previous studies and theoretical predictions, I return to the original questions. What is the nature of these Lyman-break galaxies and how will they evolve with time? In a universe where structure is probably formed in a hierarchical fashion, the answer seems to be linked to the important role of mergers and interactions in the formation and evolution of galaxies. Mergers and interactions are most likely responsible for the nature of all galaxies, especially in the high density environment at high-redshifts; and will probably govern how they will look and behave during their lifetime. Most of the evidence from the observations and modeling not only showed that Lyman-break galaxies are experiencing mergers and are forming stars at a high rate, but that these two phenomena are probably related to each other. From their N-body codes of star formation via mergers and interactions, Mihos et al. (1992) found that mergers tend to increase the global star formation rates especially in the central regions of the merging galaxies since they effectively trigger the flow of gas towards the inner parts. Furthermore, numerical simulations (Barnes 1992; Mihos et al.1992; Negroponte and White 1983) demonstrated that galaxies that are in the late stages of merging have light profiles that resemble ellipticals. These results gave rise to the belief that elliptical galaxies were formed by the merger of galaxies.

Mergers and interactions may also explain the evolution in the color gradients of galaxies. That is, they may be responsible for the "migration" of the star formation regions from the central regions at early times to the spiral arms where we see most of the star formation today. Thus, a plausible galaxy evolution

scenario may be one in which mergers govern not only the morphologies of galaxies, but also the locations of their star formations regions as well. When galaxies are first formed, their stars would tend to be born in the dense central regions. Then some galaxies may undergo major mergers which funnel gas to the central regions causing a burst of star formation. After awhile, the gas will be depleted and dispersed such that during the late stages of merger, the central light profiles evolve to follow the $r^{1/4}$ law (Barnes 1992; Mihos et al. 1992; Negroponte 1983). At this time, the presence of a central bulge might suppress the inflow of gas and consequently reduce the star formation efficiency (Mihos and Hernquist 1994). Then if the galaxy experiences further interactions with another galaxy, material can rain in on the outer parts causing the gas to collapse to form stars and eventually settle into a disk around the spheroid.

Since the majority of LBGs tend to possess light profiles that follow the $r^{1/4}$ law, it seems that they may be experiencing the late stages of mergers. However, the positive color gradients that are seen in these galaxies seem to indicate the existence of nuclear starbursts which ignite during the early stages of mergers. It is then difficult to reconcile the trend seen in the morphologies with the trend seen in the color gradients. Furthermore, the typical lifetimes of starbursts (50-150 Myr) (Mihos and Hernquist 1994a, 1996) is about an order of a magnitude less than the typical timescales over which mergers are thought to be completed (400 Myr to 1 Gyr), after which the light from the galaxy follows an $r^{1/4}$ profile (Mihos and Hernquist 1995). One possible explanation for these conflicting trends may be that the $r^{1/4}$ nature of these galaxies is highly suspect due to the large uncertainties in the galaxy classification. As was discussed in Section 3.1.4, I detected a higher fraction of galaxies possessing smooth profiles and a lower fraction of galaxies possessing irregular substructure than was detected in other studies. Another explanation may be that we are witnessing the remnants of starbursts rather than

active starbursts. In their study of the effects of a central starburst in merging systems, Mihos and Hernquist (1994b) suggest that a galaxy can exhibit blue colors in the core for several Gyrs after a merger event if the starburst population is characterized by solar metallicity. In this scenario, the galaxy's light profile will follow the $r^{1/4}$ law. This could also explain the blue cores detected in 30% of the intermediate-redshift faint spheroidals in the HDF by Menanteau et al. (2001).

If the trends are real, at redshifts between $2.0 \leq z \leq 3.6$, we may be witnessing the epoch at which many galaxies may be experiencing the late stages of merger when their star formation is enhanced and centrally concentrated. At this time, galaxies are starting to develop a spheroidal structure and forming their stars through intense, short-lived bursts. Any model that simulates galaxy formation and evolution must then allow for the possibility of the early formation of these systems with $r^{1/4}$ profiles. Although these high-redshift galaxies typically possess $r^{1/4}$ profiles, it is still unknown whether they are fully assembled and are the direct progenitors of the luminous ellipticals and bulges of spirals we see today or whether they are the progenitors of the sub-$L*$ galaxies. It is also quite possible that the morphologies of these galaxies will change several times over the course of their lifetime depending on whether they undergo more mergers and what type of mergers they experience. Despite the fact that the majority of them are forming their stars through bursts, we cannot rule out the possibility that (after the gas is depleted) they will evolve quiescently over time; nor that they can experience further mergers which ignite more starbursts in their lifetime. At this point, it is still difficult to rule out any scenario. Perhaps a more realistic explanation of the nature of LBGs is that they may represent different stages in galaxy formation and evolution and cannot be described by any one simple scenario. To find the answer to this question, we need accurate determinations of their total masses. If we can obtain robust estimations of the masses of these high-redshift galaxies, then we will

be able to constrain the epoch of formation of the first massive galaxies and predict how they will subsequently evolve.

CHAPTER 7
CONCLUSIONS AND SUGGESTIONS FOR FUTURE WORK

7.1 Conclusions

From the surface brightness and color analysis of galaxies at a range of redshifts probed at the same rest-frame wavelengths in the Hubble Deep Fields North and South, I concluded:

1). From the galaxy models, I demonstrated the importance of correcting for PSF effects before attempting to classify morphologies. Since the galaxies in the HDF are faint, their profiles can be smoothed out significantly; so much so that it is difficult to distinguish between an $r^{1/4}$ profile and an exponential profile if the PSF is not taken into account. After correcting for the PSF effects in the surface brightness profiles, I found that the population of galaxies possessing $r^{1/4}$ profiles have increased with look-back time while those with exponential profiles have decreased. However, given that these changes are only on the order of ~ 1 σ, they are only marginally significant. My results also suggested a statistically insignificant increase in the fraction of galaxies with peculiar/irregular structure at higher redshifts. These results should be viewed with a note of caution, however, because of the small sample size and large uncertainties in the galaxy models especially at small scale lengths and faint magnitudes.

2). As in local samples of galaxies, the color gradients of intermediate-redshift galaxies in all filter sets are negative, revealing central regions that are reddened because of the combined effects of age, metallicity, and dust gradients. At earlier epochs, the galaxies possess predominantly positive color gradients in the rest-frame $(UV_{218} - U_{300})_0$ and $(B_{450} - V_{606})_0$ filter sets and predominantly negative color gradients in the rest-frame $(U_{300} - B_{450})_0$ filter sets. The $(UV_{218} - U_{300})_0$

gradients are most likely ascribed to the stellar population since they are not biased by the presence of emission lines. Since age gradients are the only plausible explanation for the central blueing seen in this filter set, I concluded that the majority of high-redshift galaxies contain centrally concentrated star formation. In the $(U_{300} - B_{450})_0$ and $(B_{450} - V_{606})_0$ filter sets, the presence of nebular emission lines in the B_{450} passband are probably responsible for the reddening in the former and the blueing in the latter filter set seen in the centers of the profiles. Given that emission lines are associated with strong star formation, the conclusion that LBGs possess centrally concentrated star formation still holds. Since the results from the color gradients differ between the different redshift bins, I concluded that there is evolution in the distribution of the stellar populations. At high-redshifts, the star formation regions were concentrated in the centers of galaxies, whereas at intermediate and low-redshifts, they are located primarily in the outer disks of galaxies.

3). My results do not agree with BCFL98 who found that the dominant mode of star formation in LBGs is quiescent. The strong positive color gradients that are indicative of centrally concentrated starbursts is in better agreement with the "collisional starburst" model favored by SPF00. Thus, I concluded that starbursts that occur in the centers of LBGs are most likely ignited by galaxy mergers.

4). By comparing my results with previous observations and theoretical predictions, I concluded that mergers and interactions play an important role in galaxy evolution. That is to say that they shape the morphologies and govern how and where star formation will occur over the course of a galaxy's lifetime. They are most likely responsible for the starbursts that occur in the centers of LBGs and for their $r^{1/4}$ light profiles. Over time, mergers and interactions might cause the location of the dominant star formation regions to shift from the central to the outer regions of galaxies. The LBGs will either merge to form more luminous

galaxies or fade quiescently with time to become either the $L*$ or sub-$L*$ ellipticals and bulges of spirals that we see today. At this point, no scenario can be ruled out. An estimation of their masses is needed to further constrain their nature.

7.2 Suggestions for Future Work

Since the Hubble Deep Fields represent only a small volume of space, caution must be taken before generalizing the results to the universe as a whole. The results from this study, as well as from previous studies, represent only pencil sketches of information. Here I offer several suggestions that can help to increase our understanding of the nature of Lyman-break galaxies and galaxy evolution in general:

1). To confirm the spheroidal nature of these galaxies, more observations of their morphologies, which take into account the role of the PSF needs to be obtained.

2). More observations of the color gradients of LBGs at different areas of the sky need to be conducted to establish the validity of the existence of centrally concentrated starbursts in these systems.

3). Perhaps the most crucial missing piece of information in the successful determination of the nature of galaxies at high-redshifts is the robust measurement of the masses of a large sample LBGs. This will allow us to discover whether these galaxies are fully assembled or will later merge to form more massive galaxies. These mass measurements will also help to link observations with theoretical predictions and, thus, allow us to formulate a plausible galaxy evolution scenario.

4). Since LBGs may be the high-redshift analogs of the CNELGs, it will be very useful to compare the properties of these two groups of galaxies. If they are found to be similar, then the observations of CNELGs, which are more easily obtained than their higher redshift counterparts, can provide valuable insights into the nature of LBGs.

5). It is important to determine the cause of the high star formation rates seen in the high-redshift galaxies. A good way to test whether SPF00's "collisional starburst" model holds is to apply the color-asymmetry diagram developed by Conselice et al. (2000) to distinguish between starbursts that are driven by mergers and interactions from starbursts that were ignited by some other methods.

6). The properties of galaxies with redshifts between 1 and 2 need to be explored. During this epoch, it is thought that mergers were most dominant and played a dominant role in changing the morphologies of galaxies. For these reasons, observations of galaxies at this critical epoch will help to bridge the gap between the properties of high-redshift and low-redshift galaxies. To study these galaxies, however, robust determinations of their redshifts must be made available.

7). To produce a credible galaxy evolution scenario, it is important to better understand how and to what degree observational selection and dust comes into play when we compare galaxies at different redshifts.

Given that we are now detecting fainter galaxies at higher redshifts than before and that instruments with multi-object spectroscopic capabilities in the near-IR and 8-m class telescopes are now readily available; much information will undoubtedly be unraveled in the near future concerning the nature of LBGs, which will ultimately allow us to formulate a more robust theory on the formation and evolution of galaxies.

APPENDIX
K-CORRECTION AND COLOR TABLES

In this appendix, I present the K-corrections and colors that were generated for 16 model SEDs from Devriendt et al. (1999) up to redshifts in which the rest-frame wavelengths are greater than 1300 Angstroms. The K-corrections are for the HST WFPC-2 and NICMOS filters. The colors are in the AB magnitude system. The zero-points were obtained from the HST pipeline.

Table A-1: K-corrections for VCC 0836

z	K(UV_{218})	K(U_{300})	K(B_{450})	K(V_{606})	K(I_{814})	K(J_{110})	K(H_{160})	K(K_{222})
0.02	-0.017	0.073	0.055	0.022	0.016	0.003	-0.008	-0.056
0.04	-0.039	0.143	0.116	0.050	0.034	0.007	-0.013	-0.103
0.06	-0.067	0.209	0.181	0.077	0.054	0.010	-0.015	-0.149
0.08	-0.098	0.272	0.254	0.106	0.072	0.014	-0.014	-0.194
0.10	-0.133	0.331	0.333	0.137	0.087	0.018	-0.011	-0.238
0.12	-0.170	0.385	0.415	0.171	0.103	0.025	-0.007	-0.282
0.14	-0.206	0.436	0.502	0.206	0.123	0.032	-0.005	-0.326
0.16	-0.241	0.481	0.588	0.239	0.141	0.038	-0.002	-0.370
0.18	-0.273	0.521	0.667	0.273	0.156	0.045	0.001	-0.413
0.20	-0.303	0.554	0.731	0.313	0.173	0.052	0.002	-0.455
0.22	-0.330	0.582	0.798	0.352	0.188	0.059	0.001	-0.495
0.24	-0.355	0.604	0.876	0.394	0.203	0.065	0.000	-0.533
0.26	-0.378	0.620	0.960	0.440	0.220	0.073	-0.001	-0.568
0.28	-0.399	0.631	1.058	0.484	0.239	0.082	-0.002	-0.601
0.30	-0.418	0.636	1.130	0.530	0.258	0.091	-0.004	-0.629
0.32	-0.436	0.636	1.185	0.574	0.276	0.100	-0.005	-0.652
0.34	-0.455	0.632	1.236	0.618	0.294	0.110	-0.005	-0.668
0.36	-0.473	0.623	1.293	0.667	0.318	0.121	-0.006	-0.675
0.38	-0.491	0.610	1.342	0.715	0.347	0.132	-0.007	-0.678
0.40	...	0.594	1.394	0.761	0.372	0.143	-0.007	-0.678
0.42	...	0.577	1.446	0.812	0.397	0.155	-0.007	-0.673
0.44	...	0.559	1.491	0.861	0.418	0.166	-0.006	-0.665
0.46	...	0.539	1.543	0.915	0.441	0.178	-0.005	-0.655
0.48	...	0.519	1.597	0.969	0.462	0.190	-0.004	-0.644
0.50	...	0.499	1.646	1.027	0.483	0.202	-0.003	-0.634
0.54	...	0.460	1.737	1.145	0.524	0.230	-0.002	-0.621
0.58	...	0.423	1.848	1.262	0.567	0.259	0.000	-0.624
0.62	...	0.388	1.936	1.376	0.625	0.286	0.004	-0.631
0.66	...	0.353	2.028	1.487	0.697	0.311	0.010	-0.638
0.70	...	0.318	2.113	1.590	0.762	0.337	0.019	-0.641
0.80	...	...	2.295	1.855	0.939	0.406	0.049	-0.648
0.90	...	...	2.345	2.050	1.159	0.489	0.083	-0.640
1.00	...	...	2.394	2.233	1.385	0.561	0.132	-0.634
1.10	...	...	2.366	2.411	1.606	0.646	0.179	-0.647
1.20	...	...	2.305	2.573	1.802	0.745	0.220	-0.647
1.30	...	...	2.244	2.710	1.983	0.843	0.266	-0.635
1.40	...	...	2.174	2.818	2.160	0.952	0.309	-0.625
1.50	...	...	2.103	2.880	2.315	1.064	0.353	-0.600
1.60	...	...	2.035	2.900	2.485	1.186	0.390	-0.557
1.70	...	...	1.975	2.893	2.617	1.305	0.439	-0.533
1.80	...	...	...	2.871	2.763	1.420	0.497	-0.492
1.90	...	...	...	2.830	2.888	1.554	0.549	-0.477
2.00	...	...	...	2.786	3.005	1.698	0.604	-0.439
2.20	...	...	...	2.694	3.161	1.998	0.731	-0.352
2.40	...	...	...	2.591	3.249	2.260	0.888	-0.316
2.60	...	...	...	...	3.249	2.500	1.035	-0.246
2.80	...	...	...	...	3.197	2.675	1.247	-0.197
3.00	...	...	...	...	3.099	2.841	1.494	-0.116
3.20	...	...	...	...	3.009	2.981	1.711	0.015
3.40	...	...	...	...	2.936	3.105	1.935	0.115
3.60	...	...	...	...	2.888	3.188	2.142	0.142
3.80	...	...	...	...	2.827	3.248	2.285	0.218
4.00	...	...	...	...	2.760	3.261	2.435	0.411

Table A-2: Colors for VCC 0836

z	$(UV-U)$	$(U-B)$	$(B-V)$	$(V-I)$	$(I-J)$	$(J-H)$	$(H-K)$
0.02	0.615	1.737	0.573	0.322	0.055	0.022	-0.584
0.04	0.523	1.746	0.606	0.332	0.069	0.031	-0.542
0.06	0.429	1.748	0.644	0.340	0.085	0.036	-0.498
0.08	0.335	1.738	0.687	0.351	0.100	0.039	-0.452
0.10	0.241	1.718	0.735	0.366	0.110	0.040	-0.405
0.12	0.150	1.691	0.784	0.384	0.119	0.043	-0.357
0.14	0.062	1.655	0.835	0.400	0.132	0.047	-0.310
0.16	-0.018	1.615	0.888	0.414	0.144	0.051	-0.264
0.18	-0.091	1.576	0.933	0.434	0.152	0.056	-0.218
0.20	-0.154	1.545	0.959	0.456	0.162	0.062	-0.175
0.22	-0.209	1.505	0.986	0.479	0.171	0.069	-0.136
0.24	-0.257	1.450	1.022	0.507	0.180	0.076	-0.099
0.26	-0.296	1.383	1.060	0.535	0.189	0.085	-0.064
0.28	-0.328	1.297	1.112	0.561	0.199	0.095	-0.032
0.30	-0.352	1.229	1.140	0.587	0.208	0.106	-0.006
0.32	-0.372	1.174	1.152	0.613	0.217	0.116	0.017
0.34	-0.386	1.118	1.159	0.639	0.226	0.126	0.032
0.36	-0.395	1.052	1.167	0.664	0.239	0.138	0.039
0.38	-0.401	0.991	1.168	0.684	0.256	0.150	0.041
0.40	-2.292	0.923	1.174	0.705	0.270	0.161	0.041
0.42	...	0.854	1.176	0.731	0.283	0.172	0.037
0.44	...	0.790	1.172	0.759	0.293	0.183	0.029
0.46	...	0.719	1.170	0.789	0.304	0.195	0.021
0.48	...	0.646	1.169	0.822	0.314	0.205	0.011
0.50	...	0.577	1.160	0.859	0.323	0.216	0.001
0.54	...	0.446	1.134	0.936	0.336	0.242	-0.010
0.58	...	0.299	1.127	1.010	0.350	0.269	-0.006
0.62	...	0.174	1.103	1.066	0.380	0.293	0.005
0.66	...	0.048	1.083	1.105	0.427	0.312	0.018
0.70	...	-0.072	1.065	1.143	0.466	0.329	0.030
0.80	...	-1.098	0.983	1.233	0.573	0.368	0.067
0.90	...	...	0.839	1.208	0.711	0.417	0.093
1.00	...	...	0.704	1.165	0.865	0.440	0.135
1.10	...	...	0.499	1.122	1.001	0.478	0.196
1.20	...	...	0.276	1.088	1.098	0.536	0.237
1.30	...	...	0.078	1.044	1.181	0.588	0.270
1.40	...	...	-0.101	0.976	1.250	0.653	0.304
1.50	...	...	-0.234	0.883	1.292	0.722	0.324
1.60	...	...	-0.322	0.733	1.340	0.807	0.318
1.70	...	...	-0.376	0.594	1.354	0.876	0.342
1.80	...	...	...	0.426	1.385	0.933	0.360
1.90	...	...	...	0.260	1.376	1.016	0.396
2.00	...	...	...	0.100	1.349	1.104	0.413
2.20	...	...	...	-0.148	1.205	1.278	0.453
2.40	...	...	...	-0.341	1.031	1.383	0.573
2.60	...	...	...	0.872	0.792	1.476	0.651
2.80	...	...	...	...	0.565	1.440	0.814
3.00	...	...	...	...	0.301	1.359	0.980
3.20	...	...	...	...	0.071	1.281	1.066
3.40	...	...	...	...	-0.126	1.182	1.189
3.60	...	...	...	...	-0.258	1.058	1.370
3.80	...	...	...	...	-0.378	0.975	1.437
4.00	...	...	...	...	-0.459	0.838	1.395

Table A-3: K-corrections for VCC 1003

z	$K(UV_{218})$	$K(U_{300})$	$K(B_{450})$	$K(V_{606})$	$K(I_{814})$	$K(J_{110})$	$K(H_{160})$	$K(K_{222})$
0.02	-0.020	0.081	0.061	0.021	0.014	0.000	-0.012	-0.056
0.04	-0.041	0.158	0.129	0.049	0.030	0.001	-0.020	-0.104
0.06	-0.062	0.231	0.206	0.077	0.049	0.002	-0.024	-0.150
0.08	-0.084	0.298	0.293	0.107	0.064	0.002	-0.026	-0.195
0.10	-0.105	0.359	0.386	0.139	0.076	0.004	-0.027	-0.240
0.12	-0.127	0.413	0.484	0.175	0.090	0.008	-0.026	-0.286
0.14	-0.150	0.461	0.590	0.213	0.109	0.013	-0.027	-0.332
0.16	-0.171	0.502	0.694	0.248	0.126	0.017	-0.028	-0.377
0.18	-0.191	0.536	0.789	0.286	0.140	0.022	-0.028	-0.422
0.20	-0.211	0.562	0.865	0.329	0.156	0.027	-0.030	-0.467
0.22	-0.230	0.582	0.939	0.372	0.170	0.031	-0.034	-0.510
0.24	-0.248	0.596	1.026	0.419	0.184	0.035	-0.039	-0.552
0.26	-0.266	0.605	1.126	0.470	0.201	0.041	-0.043	-0.592
0.28	-0.282	0.610	1.241	0.520	0.219	0.049	-0.048	-0.630
0.30	-0.299	0.611	1.324	0.570	0.238	0.057	-0.052	-0.660
0.32	-0.316	0.609	1.381	0.619	0.256	0.064	-0.056	-0.685
0.34	-0.334	0.603	1.426	0.669	0.275	0.073	-0.060	-0.702
0.36	-0.353	0.594	1.481	0.724	0.299	0.083	-0.064	-0.710
0.38	-0.371	0.583	1.531	0.779	0.330	0.092	-0.067	-0.715
0.40	...	0.570	1.593	0.831	0.356	0.102	-0.070	-0.717
0.42	...	0.557	1.656	0.890	0.381	0.113	-0.072	-0.714
0.44	...	0.542	1.707	0.946	0.402	0.123	-0.074	-0.707
0.46	...	0.528	1.766	1.009	0.424	0.134	-0.076	-0.700
0.48	...	0.513	1.828	1.073	0.446	0.144	-0.077	-0.691
0.50	...	0.497	1.880	1.141	0.466	0.155	-0.079	-0.683
0.54	...	0.467	1.975	1.282	0.508	0.181	-0.082	-0.675
0.58	...	0.440	2.107	1.421	0.554	0.208	-0.083	-0.684
0.62	...	0.414	2.208	1.554	0.618	0.233	-0.082	-0.697
0.66	...	0.387	2.312	1.683	0.699	0.256	-0.078	-0.710
0.70	...	0.359	2.400	1.801	0.776	0.280	-0.072	-0.720
0.80	...	...	2.575	2.097	0.981	0.347	-0.046	-0.732
0.90	...	...	2.587	2.304	1.243	0.433	-0.019	-0.734
1.00	...	...	2.617	2.511	1.500	0.507	0.024	-0.744
1.10	...	...	2.571	2.708	1.759	0.596	0.065	-0.767
1.20	...	...	2.509	2.883	1.980	0.702	0.100	-0.773
1.30	...	...	2.459	3.019	2.181	0.807	0.142	-0.763
1.40	...	...	2.414	3.120	2.384	0.927	0.182	-0.755
1.50	...	...	2.371	3.169	2.553	1.050	0.225	-0.730
1.60	...	...	2.323	3.174	2.743	1.184	0.261	-0.693
1.70	...	...	2.274	3.160	2.894	1.317	0.309	-0.679
1.80	...	...	...	3.134	3.057	1.446	0.369	-0.640
1.90	...	...	...	3.092	3.196	1.605	0.420	-0.636
2.00	...	...	...	3.054	3.322	1.774	0.477	-0.603
2.20	...	...	...	2.986	3.455	2.130	0.612	-0.512
2.40	...	...	...	2.911	3.484	2.428	0.786	-0.485
2.60	...	...	...	...	3.460	2.694	0.954	-0.416
2.80	...	...	...	...	3.418	2.870	1.206	-0.370
3.00	...	...	...	...	3.351	3.056	1.502	-0.284
3.20	...	...	...	...	3.288	3.202	1.762	-0.143
3.40	...	...	...	...	3.235	3.340	2.016	-0.041
3.60	...	...	...	...	3.204	3.429	2.246	-0.027
3.80	...	...	...	...	3.150	3.489	2.382	0.063
4.00	...	...	...	...	3.086	3.496	2.561	0.292

Table A-4: Colors for VCC 1003

z	$(UV-U)$	$(U-B)$	$(B-V)$	$(V-I)$	$(I-J)$	$(J-H)$	$(H-K)$
0.02	0.546	1.980	0.621	0.306	0.011	-0.044	-0.626
0.04	0.447	1.989	0.661	0.318	0.027	-0.035	-0.586
0.06	0.353	1.986	0.710	0.327	0.045	-0.030	-0.545
0.08	0.264	1.967	0.766	0.341	0.060	-0.027	-0.502
0.10	0.182	1.935	0.827	0.361	0.070	-0.024	-0.457
0.12	0.105	1.892	0.890	0.382	0.080	-0.021	-0.411
0.14	0.034	1.835	0.957	0.402	0.094	-0.015	-0.366
0.16	-0.028	1.773	1.026	0.420	0.107	-0.011	-0.321
0.18	-0.083	1.711	1.084	0.444	0.116	-0.005	-0.276
0.20	-0.129	1.660	1.118	0.471	0.127	0.002	-0.234
0.22	-0.168	1.606	1.149	0.500	0.137	0.010	-0.195
0.24	-0.201	1.534	1.188	0.533	0.147	0.018	-0.157
0.26	-0.228	1.445	1.237	0.567	0.157	0.029	-0.121
0.28	-0.250	1.336	1.301	0.598	0.169	0.041	-0.088
0.30	-0.267	1.252	1.336	0.629	0.180	0.053	-0.061
0.32	-0.282	1.192	1.345	0.660	0.190	0.065	-0.041
0.34	-0.295	1.140	1.341	0.692	0.200	0.077	-0.027
0.36	-0.305	1.077	1.340	0.722	0.215	0.091	-0.022
0.38	-0.312	1.016	1.336	0.747	0.235	0.104	-0.021
0.40	-2.288	0.942	1.345	0.773	0.252	0.116	-0.022
0.42	...	0.865	1.350	0.806	0.266	0.129	-0.027
0.44	...	0.800	1.344	0.842	0.278	0.141	-0.035
0.46	...	0.726	1.341	0.882	0.288	0.154	-0.044
0.48	...	0.649	1.339	0.924	0.299	0.166	-0.054
0.50	...	0.581	1.323	0.972	0.310	0.178	-0.064
0.54	...	0.457	1.277	1.070	0.325	0.207	-0.075
0.58	...	0.298	1.269	1.164	0.344	0.235	-0.068
0.62	...	0.170	1.238	1.234	0.382	0.260	-0.054
0.66	...	0.039	1.212	1.282	0.440	0.278	-0.036
0.70	...	-0.078	1.184	1.322	0.494	0.296	-0.021
0.80	...	-1.098	1.063	1.414	0.631	0.338	0.017
0.90	...	...	0.868	1.361	0.807	0.396	0.046
1.00	...	...	0.691	1.312	0.990	0.427	0.099
1.10	...	...	0.450	1.249	1.160	0.475	0.163
1.20	...	...	0.213	1.202	1.275	0.547	0.204
1.30	...	...	0.024	1.138	1.372	0.610	0.236
1.40	...	...	-0.121	1.037	1.455	0.689	0.268
1.50	...	...	-0.214	0.917	1.501	0.768	0.287
1.60	...	...	-0.267	0.731	1.557	0.868	0.285
1.70	...	...	-0.302	0.566	1.575	0.953	0.319
1.80	...	...	...	0.377	1.609	1.021	0.341
1.90	...	...	...	0.197	1.591	1.128	0.388
2.00	...	...	...	0.033	1.547	1.241	0.412
2.20	...	...	...	-0.169	1.325	1.462	0.455
2.40	...	...	...	-0.274	1.056	1.586	0.602
2.60	...	...	...	0.877	0.766	1.685	0.701
2.80	...	...	...	...	0.547	1.610	0.906
3.00	...	...	...	...	0.295	1.499	1.116
3.20	...	...	...	...	0.086	1.385	1.236
3.40	...	...	...	...	-0.106	1.270	1.387
3.60	...	...	...	...	-0.226	1.128	1.605
3.80	...	...	...	...	-0.339	1.052	1.651
4.00	...	...	...	...	-0.412	0.881	1.601

Table A-5: K-corrections for VCC 1043

z	K(UV_{218})	K(U_{300})	K(B_{450})	K(V_{606})	K(I_{814})	K(J_{110})	K(H_{160})	K(K_{222})
0.02	-0.020	0.079	0.060	0.021	0.014	0.001	-0.011	-0.056
0.04	-0.042	0.155	0.129	0.049	0.030	0.001	-0.019	-0.103
0.06	-0.063	0.227	0.206	0.077	0.049	0.002	-0.024	-0.149
0.08	-0.085	0.293	0.292	0.107	0.064	0.002	-0.026	-0.194
0.10	-0.108	0.352	0.385	0.139	0.077	0.005	-0.026	-0.239
0.12	-0.131	0.406	0.483	0.174	0.091	0.009	-0.026	-0.286
0.14	-0.154	0.453	0.588	0.213	0.109	0.013	-0.027	-0.331
0.16	-0.176	0.493	0.691	0.248	0.126	0.017	-0.027	-0.376
0.18	-0.198	0.526	0.786	0.285	0.140	0.022	-0.027	-0.422
0.20	-0.218	0.551	0.861	0.328	0.156	0.027	-0.030	-0.466
0.22	-0.238	0.570	0.935	0.371	0.170	0.031	-0.034	-0.509
0.24	-0.256	0.584	1.022	0.418	0.184	0.035	-0.038	-0.551
0.26	-0.274	0.593	1.120	0.469	0.201	0.042	-0.042	-0.591
0.28	-0.291	0.597	1.235	0.519	0.219	0.049	-0.047	-0.628
0.30	-0.308	0.598	1.318	0.569	0.238	0.057	-0.051	-0.659
0.32	-0.326	0.595	1.374	0.618	0.256	0.065	-0.055	-0.684
0.34	-0.344	0.589	1.418	0.668	0.275	0.073	-0.059	-0.701
0.36	-0.363	0.580	1.473	0.722	0.299	0.083	-0.063	-0.709
0.38	-0.381	0.568	1.522	0.777	0.330	0.093	-0.066	-0.713
0.40	...	0.555	1.583	0.829	0.356	0.103	-0.069	-0.715
0.42	...	0.541	1.646	0.888	0.381	0.113	-0.071	-0.712
0.44	...	0.526	1.696	0.944	0.402	0.123	-0.073	-0.706
0.46	...	0.511	1.755	1.007	0.424	0.135	-0.075	-0.698
0.48	...	0.496	1.815	1.070	0.445	0.145	-0.076	-0.689
0.50	...	0.480	1.867	1.138	0.466	0.155	-0.077	-0.681
0.54	...	0.449	1.960	1.278	0.508	0.182	-0.081	-0.673
0.58	...	0.421	2.090	1.416	0.553	0.208	-0.082	-0.682
0.62	...	0.394	2.190	1.549	0.617	0.234	-0.081	-0.695
0.66	...	0.367	2.291	1.677	0.698	0.256	-0.076	-0.708
0.70	...	0.338	2.378	1.794	0.776	0.281	-0.070	-0.717
0.80	...	...	2.548	2.088	0.980	0.348	-0.044	-0.730
0.90	...	...	2.560	2.293	1.241	0.434	-0.017	-0.731
1.00	...	...	2.588	2.497	1.496	0.507	0.026	-0.741
1.10	...	...	2.543	2.690	1.754	0.596	0.067	-0.764
1.20	...	...	2.480	2.861	1.974	0.702	0.102	-0.770
1.30	...	...	2.428	2.995	2.174	0.807	0.144	-0.760
1.40	...	...	2.382	3.093	2.374	0.926	0.184	-0.752
1.50	...	...	2.338	3.141	2.541	1.049	0.227	-0.726
1.60	...	...	2.288	3.145	2.730	1.183	0.263	-0.690
1.70	...	...	2.237	3.130	2.878	1.316	0.311	-0.676
1.80	...	...	...	3.103	3.038	1.445	0.371	-0.636
1.90	...	...	...	3.061	3.174	1.602	0.422	-0.632
2.00	...	...	...	3.022	3.297	1.770	0.478	-0.600
2.20	...	...	...	2.952	3.427	2.124	0.613	-0.508
2.40	...	...	...	2.875	3.456	2.420	0.788	-0.481
2.60	...	...	...	...	3.432	2.683	0.955	-0.412
2.80	...	...	...	...	3.389	2.857	1.206	-0.366
3.00	...	...	...	...	3.319	3.039	1.501	-0.280
3.20	...	...	...	...	3.254	3.183	1.760	-0.139
3.40	...	...	...	...	3.199	3.317	2.012	-0.038
3.60	...	...	...	...	3.167	3.403	2.241	-0.024
3.80	...	...	...	...	3.113	3.460	2.375	0.065
4.00	...	...	...	...	3.048	3.466	2.552	0.295

Table A-6: Colors for VCC 1043

z	$(UV-U)$	$(U-B)$	$(B-V)$	$(V-I)$	$(I-J)$	$(J-H)$	$(H-K)$
0.02	0.534	1.964	0.620	0.306	0.012	-0.043	-0.624
0.04	0.437	1.973	0.660	0.318	0.028	-0.034	-0.585
0.06	0.343	1.968	0.708	0.327	0.045	-0.028	-0.543
0.08	0.255	1.948	0.765	0.341	0.060	-0.026	-0.500
0.10	0.173	1.916	0.825	0.361	0.071	-0.023	-0.456
0.12	0.096	1.872	0.888	0.382	0.081	-0.020	-0.409
0.14	0.026	1.814	0.954	0.401	0.095	-0.014	-0.364
0.16	-0.037	1.751	1.022	0.420	0.108	-0.010	-0.320
0.18	-0.092	1.689	1.080	0.443	0.116	-0.004	-0.275
0.20	-0.138	1.639	1.114	0.470	0.127	0.003	-0.233
0.22	-0.177	1.584	1.145	0.499	0.137	0.011	-0.193
0.24	-0.210	1.513	1.184	0.532	0.147	0.019	-0.155
0.26	-0.238	1.424	1.231	0.566	0.158	0.029	-0.120
0.28	-0.259	1.315	1.295	0.597	0.169	0.042	-0.087
0.30	-0.277	1.231	1.329	0.628	0.180	0.054	-0.060
0.32	-0.292	1.171	1.338	0.659	0.190	0.066	-0.039
0.34	-0.304	1.120	1.333	0.690	0.200	0.078	-0.026
0.36	-0.314	1.057	1.333	0.721	0.215	0.092	-0.021
0.38	-0.321	0.996	1.328	0.745	0.235	0.104	-0.020
0.40	-2.288	0.922	1.336	0.771	0.252	0.117	-0.020
0.42	...	0.845	1.341	0.804	0.266	0.130	-0.025
0.44	...	0.780	1.335	0.840	0.277	0.142	-0.034
0.46	...	0.707	1.331	0.879	0.288	0.155	-0.043
0.48	...	0.631	1.328	0.922	0.299	0.166	-0.053
0.50	...	0.563	1.312	0.969	0.309	0.178	-0.063
0.54	...	0.439	1.266	1.067	0.325	0.208	-0.074
0.58	...	0.282	1.256	1.160	0.344	0.236	-0.067
0.62	...	0.154	1.224	1.229	0.382	0.260	-0.053
0.66	...	0.025	1.197	1.277	0.440	0.278	-0.035
0.70	...	-0.090	1.167	1.316	0.493	0.297	-0.020
0.80	...	-1.098	1.045	1.406	0.629	0.338	0.018
0.90	...	...	0.852	1.351	0.805	0.397	0.047
1.00	...	...	0.676	1.300	0.987	0.427	0.100
1.10	...	...	0.438	1.235	1.156	0.475	0.164
1.20	...	...	0.204	1.187	1.270	0.546	0.204
1.30	...	...	0.017	1.122	1.365	0.609	0.237
1.40	...	...	-0.128	1.019	1.447	0.688	0.268
1.50	...	...	-0.220	0.900	1.491	0.767	0.287
1.60	...	...	-0.274	0.716	1.545	0.866	0.285
1.70	...	...	-0.310	0.552	1.561	0.951	0.320
1.80	...	...	...	0.366	1.593	1.018	0.341
1.90	...	...	...	0.188	1.572	1.125	0.388
2.00	...	...	...	0.026	1.527	1.237	0.411
2.20	...	...	...	-0.175	1.303	1.456	0.454
2.40	...	...	...	-0.282	1.037	1.578	0.601
2.60	...	...	...	0.876	0.750	1.674	0.699
2.80	...	...	...	...	0.532	1.597	0.904
3.00	...	...	...	...	0.281	1.485	1.113
3.20	...	...	...	...	0.072	1.369	1.232
3.40	...	...	...	...	-0.118	1.253	1.381
3.60	...	...	...	...	-0.236	1.109	1.597
3.80	...	...	...	...	-0.347	1.032	1.643
4.00	...	...	...	...	-0.419	0.861	1.591

Table A-7: K-corrections for VCC 1544

z	K(UV_{218})	K(U_{300})	K(B_{450})	K(V_{606})	K(I_{814})	K(J_{110})	K(H_{160})	K(K_{222})
0.02	-0.002	0.024	0.020	0.000	-0.002	-0.009	-0.018	-0.055
0.04	-0.005	0.045	0.045	0.001	-0.004	-0.017	-0.032	-0.105
0.06	-0.011	0.065	0.070	0.002	-0.006	-0.025	-0.044	-0.153
0.08	-0.018	0.082	0.102	0.005	-0.005	-0.032	-0.053	-0.200
0.10	-0.026	0.099	0.137	0.009	-0.005	-0.039	-0.059	-0.245
0.12	-0.034	0.115	0.177	0.013	-0.007	-0.044	-0.065	-0.289
0.14	-0.041	0.131	0.219	0.018	-0.008	-0.050	-0.071	-0.333
0.16	-0.046	0.145	0.262	0.022	-0.010	-0.055	-0.078	-0.376
0.18	-0.048	0.158	0.299	0.027	-0.013	-0.060	-0.084	-0.420
0.20	-0.049	0.168	0.331	0.034	-0.015	-0.066	-0.091	-0.463
0.22	-0.047	0.177	0.374	0.042	-0.017	-0.070	-0.099	-0.505
0.24	-0.043	0.185	0.425	0.052	-0.019	-0.074	-0.107	-0.545
0.26	-0.039	0.191	0.472	0.064	-0.021	-0.078	-0.115	-0.583
0.28	-0.032	0.196	0.532	0.077	-0.022	-0.082	-0.123	-0.619
0.30	-0.024	0.199	0.582	0.094	-0.022	-0.085	-0.130	-0.652
0.32	-0.016	0.202	0.630	0.111	-0.022	-0.088	-0.139	-0.682
0.34	-0.009	0.203	0.680	0.129	-0.021	-0.091	-0.147	-0.706
0.36	-0.002	0.203	0.727	0.150	-0.018	-0.094	-0.155	-0.723
0.38	0.005	0.201	0.760	0.170	-0.013	-0.095	-0.163	-0.735
0.40	...	0.199	0.780	0.190	-0.010	-0.097	-0.171	-0.743
0.42	...	0.197	0.794	0.212	-0.008	-0.099	-0.179	-0.746
0.44	...	0.195	0.807	0.236	-0.005	-0.100	-0.187	-0.748
0.46	...	0.193	0.822	0.262	0.001	-0.101	-0.194	-0.750
0.48	...	0.191	0.837	0.287	0.003	-0.102	-0.201	-0.750
0.50	...	0.189	0.850	0.315	0.004	-0.103	-0.207	-0.750
0.54	...	0.188	0.877	0.373	0.003	-0.102	-0.221	-0.755
0.58	...	0.189	0.906	0.433	0.005	-0.102	-0.233	-0.764
0.62	...	0.193	0.930	0.495	0.017	-0.102	-0.243	-0.775
0.66	...	0.198	0.955	0.557	0.037	-0.103	-0.252	-0.787
0.70	...	0.203	0.979	0.619	0.043	-0.105	-0.259	-0.799
0.80	...	...	1.031	0.781	0.080	-0.105	-0.272	-0.836
0.90	...	...	1.053	0.891	0.164	-0.096	-0.279	-0.862
1.00	...	...	1.078	0.951	0.313	-0.090	-0.279	-0.884
1.10	...	...	1.082	1.001	0.454	-0.075	-0.283	-0.915
1.20	...	...	1.073	1.046	0.578	-0.046	-0.287	-0.942
1.30	...	...	1.067	1.085	0.687	-0.013	-0.290	-0.965
1.40	...	...	1.058	1.115	0.782	0.023	-0.294	-0.982
1.50	...	...	1.056	1.136	0.859	0.066	-0.298	-0.981
1.60	...	...	1.060	1.149	0.922	0.118	-0.300	-0.969
1.70	...	...	1.065	1.154	0.954	0.171	-0.296	-0.976
1.80	...	...	...	1.157	0.994	0.224	-0.295	-0.984
1.90	...	...	...	1.155	1.027	0.279	-0.289	-0.990
2.00	...	...	...	1.153	1.062	0.342	-0.285	-0.989
2.20	...	...	...	1.154	1.114	0.487	-0.267	-0.996
2.40	...	...	...	1.150	1.153	0.629	-0.237	-0.992
2.60	...	...	...	...	1.156	0.766	-0.209	-1.005
2.80	...	...	...	...	1.153	0.857	-0.133	-1.015
3.00	...	...	...	...	1.129	0.901	-0.069	-1.006
3.20	...	...	...	...	1.117	0.939	0.109	-0.974
3.40	...	...	...	...	1.119	0.972	0.255	-0.955
3.60	...	...	...	...	1.146	0.995	0.414	-0.962
3.80	...	...	...	...	1.161	1.016	0.534	-0.977
4.00	...	...	...	...	1.165	1.030	0.584	-0.906

Table A-8: Colors for VCC 1544

z	$(UV-U)$	$(U-B)$	$(B-V)$	$(V-I)$	$(I-J)$	$(J-H)$	$(H-K)$
0.02	0.215	0.874	0.098	0.001	-0.184	-0.171	-0.660
0.04	0.190	0.870	0.122	0.004	-0.178	-0.165	-0.625
0.06	0.165	0.865	0.146	0.007	-0.172	-0.161	-0.588
0.08	0.140	0.852	0.175	0.008	-0.164	-0.159	-0.550
0.10	0.115	0.833	0.207	0.012	-0.157	-0.159	-0.511
0.12	0.091	0.810	0.242	0.018	-0.153	-0.159	-0.473
0.14	0.068	0.783	0.279	0.024	-0.149	-0.158	-0.436
0.16	0.049	0.755	0.317	0.030	-0.145	-0.157	-0.399
0.18	0.034	0.730	0.350	0.038	-0.142	-0.156	-0.361
0.20	0.023	0.708	0.376	0.046	-0.139	-0.154	-0.326
0.22	0.015	0.675	0.410	0.057	-0.137	-0.151	-0.291
0.24	0.011	0.633	0.450	0.069	-0.135	-0.147	-0.259
0.26	0.009	0.591	0.486	0.082	-0.133	-0.143	-0.229
0.28	0.011	0.537	0.532	0.097	-0.130	-0.139	-0.201
0.30	0.015	0.490	0.565	0.114	-0.127	-0.134	-0.175
0.32	0.021	0.444	0.597	0.130	-0.124	-0.129	-0.154
0.34	0.027	0.396	0.629	0.147	-0.120	-0.124	-0.138
0.36	0.035	0.348	0.656	0.165	-0.115	-0.118	-0.129
0.38	0.043	0.313	0.669	0.181	-0.108	-0.112	-0.124
0.40	-2.270	0.291	0.669	0.198	-0.103	-0.106	-0.124
0.42	...	0.273	0.662	0.217	-0.099	-0.100	-0.128
0.44	...	0.258	0.651	0.239	-0.096	-0.093	-0.134
0.46	...	0.242	0.639	0.259	-0.089	-0.087	-0.139
0.48	...	0.225	0.630	0.281	-0.085	-0.081	-0.146
0.50	...	0.210	0.615	0.309	-0.084	-0.075	-0.152
0.54	...	0.181	0.584	0.367	-0.085	-0.061	-0.161
0.58	...	0.154	0.553	0.425	-0.083	-0.048	-0.165
0.62	...	0.134	0.516	0.476	-0.071	-0.039	-0.163
0.66	...	0.114	0.479	0.517	-0.051	-0.031	-0.160
0.70	...	0.095	0.441	0.573	-0.043	-0.025	-0.155
0.80	...	-1.080	0.330	0.698	-0.006	-0.012	-0.132
0.90	...	...	0.242	0.726	0.068	0.003	-0.112
1.00	...	...	0.207	0.638	0.212	0.009	-0.091
1.10	...	...	0.161	0.546	0.338	0.028	-0.064
1.20	...	...	0.107	0.467	0.433	0.060	-0.041
1.30	...	...	0.062	0.397	0.509	0.097	-0.021
1.40	...	...	0.022	0.333	0.568	0.137	-0.007
1.50	...	...	-0.001	0.276	0.603	0.184	-0.012
1.60	...	...	-0.010	0.226	0.613	0.238	-0.026
1.70	...	...	-0.010	0.198	0.594	0.287	-0.016
1.80	...	...	...	0.162	0.580	0.339	-0.007
1.90	...	...	...	0.126	0.559	0.387	0.005
2.00	...	...	...	0.089	0.530	0.447	0.009
2.20	...	...	...	0.038	0.437	0.574	0.034
2.40	...	...	...	-0.005	0.334	0.686	0.059
2.60	...	...	...	0.893	0.200	0.795	0.101
2.80	...	...	...	...	0.106	0.811	0.186
3.00	...	...	...	...	0.038	0.731	0.302
3.20	...	...	...	...	-0.013	0.651	0.387
3.40	...	...	...	...	-0.043	0.538	0.515
3.60	...	...	...	...	-0.040	0.402	0.680
3.80	...	...	...	...	-0.045	0.303	0.816
4.00	...	...	...	...	-0.055	0.266	0.795

Table A-9: K-corrections for VCC 1690

z	$K(UV_{218})$	$K(U_{300})$	$K(B_{450})$	$K(V_{606})$	$K(I_{814})$	$K(J_{110})$	$K(H_{160})$	$K(K_{222})$
0.02	-0.017	0.077	0.057	0.020	0.014	0.001	-0.010	-0.057
0.04	-0.038	0.152	0.121	0.048	0.030	0.003	-0.017	-0.105
0.06	-0.061	0.223	0.193	0.075	0.049	0.004	-0.020	-0.152
0.08	-0.087	0.289	0.272	0.104	0.064	0.006	-0.021	-0.197
0.10	-0.114	0.350	0.357	0.135	0.077	0.008	-0.020	-0.242
0.12	-0.143	0.406	0.447	0.169	0.091	0.013	-0.018	-0.288
0.14	-0.172	0.457	0.542	0.206	0.109	0.018	-0.018	-0.334
0.16	-0.200	0.502	0.637	0.239	0.126	0.022	-0.017	-0.379
0.18	-0.226	0.541	0.723	0.275	0.140	0.028	-0.016	-0.423
0.20	-0.251	0.573	0.792	0.315	0.156	0.033	-0.017	-0.466
0.22	-0.274	0.598	0.862	0.356	0.170	0.038	-0.019	-0.509
0.24	-0.295	0.619	0.944	0.401	0.183	0.042	-0.022	-0.548
0.26	-0.316	0.633	1.034	0.448	0.200	0.049	-0.025	-0.586
0.28	-0.334	0.643	1.139	0.495	0.218	0.056	-0.028	-0.621
0.30	-0.352	0.647	1.215	0.543	0.237	0.064	-0.031	-0.651
0.32	-0.370	0.648	1.270	0.589	0.254	0.072	-0.034	-0.674
0.34	-0.389	0.644	1.318	0.636	0.272	0.081	-0.037	-0.691
0.36	-0.407	0.636	1.373	0.687	0.296	0.091	-0.040	-0.699
0.38	-0.426	0.625	1.423	0.738	0.326	0.100	-0.042	-0.703
0.40	...	0.612	1.479	0.787	0.351	0.110	-0.044	-0.704
0.42	...	0.597	1.537	0.842	0.375	0.121	-0.046	-0.701
0.44	...	0.581	1.584	0.894	0.396	0.131	-0.047	-0.694
0.46	...	0.565	1.640	0.952	0.418	0.142	-0.048	-0.686
0.48	...	0.548	1.697	1.010	0.438	0.152	-0.048	-0.676
0.50	...	0.531	1.748	1.073	0.459	0.163	-0.049	-0.666
0.54	...	0.497	1.841	1.202	0.499	0.189	-0.051	-0.656
0.58	...	0.465	1.963	1.328	0.543	0.215	-0.051	-0.662
0.62	...	0.435	2.058	1.450	0.604	0.241	-0.050	-0.673
0.66	...	0.404	2.157	1.569	0.679	0.264	-0.045	-0.683
0.70	...	0.373	2.247	1.678	0.750	0.288	-0.039	-0.689
0.80	...	...	2.436	1.956	0.940	0.354	-0.013	-0.700
0.90	...	...	2.472	2.156	1.180	0.436	0.014	-0.699
1.00	...	...	2.518	2.351	1.419	0.507	0.058	-0.702
1.10	...	...	2.484	2.539	1.657	0.593	0.100	-0.723
1.20	...	...	2.425	2.710	1.863	0.695	0.135	-0.727
1.30	...	...	2.371	2.851	2.051	0.795	0.177	-0.717
1.40	...	...	2.315	2.962	2.238	0.908	0.217	-0.709
1.50	...	...	2.258	3.023	2.398	1.025	0.259	-0.686
1.60	...	...	2.200	3.039	2.579	1.152	0.294	-0.649
1.70	...	...	2.145	3.032	2.721	1.277	0.342	-0.632
1.80	...	...	...	3.010	2.878	1.398	0.400	-0.593
1.90	...	...	...	2.971	3.012	1.544	0.450	-0.586
2.00	...	...	...	2.931	3.137	1.699	0.505	-0.552
2.20	...	...	...	2.853	3.289	2.024	0.634	-0.466
2.40	...	...	...	2.763	3.356	2.302	0.798	-0.437
2.60	...	...	...	...	3.349	2.553	0.954	-0.370
2.80	...	...	...	...	3.305	2.729	1.185	-0.324
3.00	...	...	...	...	3.225	2.906	1.455	-0.241
3.20	...	...	...	...	3.150	3.052	1.691	-0.107
3.40	...	...	...	...	3.087	3.186	1.927	-0.008
3.60	...	...	...	...	3.047	3.277	2.142	0.011
3.80	...	...	...	...	2.989	3.343	2.279	0.093
4.00	...	...	...	...	2.924	3.357	2.443	0.304

Table A-10: Colors for VCC 1690

z	$(UV-U)$	$(U-B)$	$(B-V)$	$(V-I)$	$(I-J)$	$(J-H)$	$(H-K)$
0.02	0.609	1.846	0.590	0.302	0.020	-0.018	-0.611
0.04	0.514	1.857	0.626	0.313	0.034	-0.010	-0.570
0.06	0.420	1.857	0.670	0.322	0.051	-0.005	-0.527
0.08	0.328	1.844	0.720	0.335	0.065	-0.003	-0.482
0.10	0.239	1.820	0.774	0.353	0.076	-0.001	-0.436
0.12	0.154	1.788	0.830	0.373	0.085	0.002	-0.388
0.14	0.074	1.744	0.889	0.391	0.098	0.006	-0.342
0.16	0.000	1.695	0.949	0.408	0.111	0.010	-0.296
0.18	-0.065	1.648	1.000	0.430	0.119	0.014	-0.251
0.20	-0.122	1.609	1.030	0.455	0.129	0.020	-0.208
0.22	-0.171	1.565	1.059	0.481	0.139	0.028	-0.169
0.24	-0.213	1.505	1.096	0.512	0.148	0.035	-0.131
0.26	-0.248	1.430	1.138	0.543	0.158	0.044	-0.096
0.28	-0.277	1.335	1.196	0.571	0.169	0.055	-0.065
0.30	-0.299	1.262	1.226	0.601	0.179	0.066	-0.038
0.32	-0.318	1.207	1.236	0.629	0.189	0.077	-0.017
0.34	-0.333	1.155	1.237	0.658	0.199	0.088	-0.003
0.36	-0.344	1.093	1.241	0.685	0.213	0.100	0.003
0.38	-0.351	1.032	1.239	0.708	0.232	0.112	0.005
0.40	-2.290	0.963	1.246	0.731	0.247	0.124	0.004
0.42	...	0.890	1.250	0.761	0.261	0.136	0.000
0.44	...	0.827	1.245	0.793	0.272	0.148	-0.008
0.46	...	0.756	1.243	0.829	0.283	0.160	-0.017
0.48	...	0.681	1.242	0.866	0.293	0.171	-0.027
0.50	...	0.613	1.230	0.909	0.303	0.182	-0.038
0.54	...	0.485	1.195	0.996	0.318	0.210	-0.050
0.58	...	0.333	1.189	1.079	0.335	0.237	-0.045
0.62	...	0.206	1.164	1.141	0.369	0.261	-0.033
0.66	...	0.077	1.144	1.185	0.422	0.279	-0.018
0.70	...	-0.045	1.124	1.223	0.469	0.297	-0.006
0.80	...	-1.097	1.036	1.311	0.592	0.337	0.030
0.90	...	...	0.873	1.272	0.749	0.392	0.057
1.00	...	...	0.723	1.229	0.917	0.420	0.104
1.10	...	...	0.502	1.179	1.069	0.464	0.166
1.20	...	...	0.272	1.144	1.174	0.530	0.206
1.30	...	...	0.077	1.096	1.263	0.588	0.238
1.40	...	...	-0.091	1.021	1.336	0.661	0.270
1.50	...	...	-0.209	0.923	1.379	0.736	0.290
1.60	...	...	-0.284	0.758	1.434	0.828	0.287
1.70	...	...	-0.332	0.609	1.451	0.905	0.317
1.80	...	...	...	0.431	1.487	0.969	0.337
1.90	...	...	...	0.256	1.476	1.063	0.380
2.00	...	...	...	0.093	1.446	1.164	0.401
2.20	...	...	...	-0.139	1.273	1.360	0.443
2.40	...	...	...	-0.296	1.062	1.475	0.578
2.60	...	...	...	0.875	0.805	1.570	0.667
2.80	...	...	...	...	0.584	1.515	0.852
3.00	...	...	...	...	0.327	1.423	1.039
3.20	...	...	...	...	0.106	1.332	1.142
3.40	...	...	...	...	-0.091	1.231	1.278
3.60	...	...	...	...	-0.222	1.106	1.475
3.80	...	...	...	...	-0.345	1.035	1.530
4.00	...	...	...	...	-0.426	0.886	1.484

Table A-11: K-corrections for VCC 1727

z	K(UV_{218})	K(U_{300})	K(B_{450})	K(V_{606})	K(I_{814})	K(J_{110})	K(H_{160})	K(K_{222})
0.02	-0.018	0.078	0.058	0.020	0.013	0.001	-0.011	-0.057
0.04	-0.038	0.154	0.124	0.048	0.029	0.001	-0.019	-0.105
0.06	-0.059	0.225	0.198	0.075	0.047	0.002	-0.023	-0.151
0.08	-0.082	0.291	0.280	0.104	0.062	0.003	-0.024	-0.197
0.10	-0.106	0.352	0.369	0.135	0.074	0.005	-0.024	-0.242
0.12	-0.131	0.407	0.462	0.170	0.087	0.009	-0.023	-0.288
0.14	-0.156	0.456	0.562	0.207	0.105	0.014	-0.024	-0.334
0.16	-0.180	0.499	0.660	0.241	0.122	0.018	-0.024	-0.379
0.18	-0.203	0.536	0.750	0.277	0.135	0.023	-0.024	-0.424
0.20	-0.225	0.565	0.821	0.318	0.150	0.027	-0.025	-0.468
0.22	-0.245	0.588	0.893	0.360	0.164	0.032	-0.029	-0.510
0.24	-0.265	0.605	0.976	0.406	0.177	0.035	-0.032	-0.551
0.26	-0.283	0.618	1.070	0.455	0.193	0.041	-0.036	-0.590
0.28	-0.301	0.625	1.179	0.502	0.212	0.049	-0.040	-0.626
0.30	-0.318	0.629	1.258	0.551	0.230	0.056	-0.044	-0.656
0.32	-0.335	0.628	1.313	0.598	0.247	0.064	-0.047	-0.680
0.34	-0.354	0.624	1.359	0.646	0.265	0.072	-0.051	-0.697
0.36	-0.372	0.616	1.414	0.699	0.289	0.081	-0.054	-0.705
0.38	-0.391	0.606	1.463	0.752	0.319	0.091	-0.057	-0.710
0.40	...	0.593	1.522	0.802	0.344	0.100	-0.059	-0.712
0.42	...	0.580	1.581	0.858	0.369	0.110	-0.062	-0.709
0.44	...	0.565	1.630	0.912	0.389	0.120	-0.064	-0.703
0.46	...	0.550	1.687	0.972	0.411	0.131	-0.065	-0.695
0.48	...	0.535	1.745	1.032	0.432	0.141	-0.066	-0.686
0.50	...	0.519	1.796	1.098	0.452	0.151	-0.067	-0.677
0.54	...	0.487	1.889	1.231	0.493	0.177	-0.070	-0.669
0.58	...	0.459	2.014	1.363	0.537	0.203	-0.071	-0.676
0.62	...	0.431	2.112	1.489	0.599	0.227	-0.071	-0.688
0.66	...	0.403	2.212	1.611	0.677	0.249	-0.066	-0.700
0.70	...	0.373	2.301	1.724	0.750	0.273	-0.061	-0.708
0.80	...	...	2.484	2.007	0.946	0.338	-0.036	-0.719
0.90	...	...	2.509	2.209	1.195	0.421	-0.010	-0.720
1.00	...	...	2.549	2.408	1.441	0.492	0.032	-0.727
1.10	...	...	2.511	2.598	1.687	0.579	0.072	-0.750
1.20	...	...	2.452	2.769	1.899	0.682	0.106	-0.756
1.30	...	...	2.401	2.908	2.091	0.784	0.146	-0.746
1.40	...	...	2.352	3.014	2.283	0.899	0.185	-0.739
1.50	...	...	2.303	3.071	2.445	1.018	0.226	-0.715
1.60	...	...	2.251	3.082	2.630	1.148	0.261	-0.679
1.70	...	...	2.199	3.073	2.774	1.276	0.308	-0.665
1.80	...	...	...	3.050	2.933	1.400	0.367	-0.627
1.90	...	...	...	3.011	3.069	1.551	0.416	-0.623
2.00	...	...	...	2.973	3.193	1.711	0.471	-0.591
2.20	...	...	...	2.902	3.336	2.049	0.603	-0.505
2.40	...	...	...	2.821	3.386	2.334	0.770	-0.477
2.60	...	...	...	...	3.373	2.589	0.931	-0.411
2.80	...	...	...	...	3.332	2.764	1.170	-0.366
3.00	...	...	...	...	3.261	2.943	1.451	-0.282
3.20	...	...	...	...	3.193	3.088	1.697	-0.146
3.40	...	...	...	...	3.136	3.223	1.939	-0.047
3.60	...	...	...	...	3.101	3.314	2.160	-0.031
3.80	...	...	...	...	3.046	3.378	2.295	0.054
4.00	...	...	...	...	2.981	3.390	2.464	0.273

Table A-12: Colors for VCC 1727

z	$(UV-U)$	$(U-B)$	$(B-V)$	$(V-I)$	$(I-J)$	$(J-H)$	$(H-K)$
0.02	0.579	1.894	0.600	0.296	0.010	-0.034	-0.620
0.04	0.484	1.905	0.638	0.308	0.024	-0.026	-0.579
0.06	0.391	1.903	0.684	0.318	0.041	-0.021	-0.537
0.08	0.302	1.887	0.737	0.331	0.055	-0.018	-0.493
0.10	0.217	1.860	0.794	0.350	0.065	-0.016	-0.448
0.12	0.137	1.822	0.853	0.371	0.075	-0.013	-0.401
0.14	0.063	1.773	0.915	0.390	0.088	-0.008	-0.356
0.16	-0.005	1.718	0.979	0.408	0.101	-0.004	-0.311
0.18	-0.065	1.664	1.033	0.431	0.109	0.001	-0.265
0.20	-0.116	1.621	1.065	0.457	0.119	0.007	-0.223
0.22	-0.160	1.573	1.094	0.485	0.129	0.014	-0.184
0.24	-0.198	1.508	1.132	0.517	0.139	0.022	-0.147
0.26	-0.229	1.427	1.177	0.549	0.149	0.031	-0.111
0.28	-0.254	1.327	1.237	0.579	0.160	0.043	-0.079
0.30	-0.275	1.250	1.268	0.609	0.170	0.054	-0.053
0.32	-0.292	1.194	1.277	0.639	0.181	0.065	-0.032
0.34	-0.306	1.143	1.276	0.669	0.191	0.077	-0.018
0.36	-0.317	1.081	1.278	0.698	0.205	0.089	-0.013
0.38	-0.325	1.021	1.275	0.721	0.225	0.102	-0.011
0.40	-2.289	0.951	1.283	0.746	0.241	0.114	-0.012
0.42	...	0.877	1.287	0.777	0.255	0.126	-0.016
0.44	...	0.814	1.281	0.811	0.266	0.138	-0.024
0.46	...	0.743	1.278	0.848	0.277	0.150	-0.033
0.48	...	0.669	1.276	0.888	0.287	0.161	-0.043
0.50	...	0.601	1.263	0.933	0.298	0.172	-0.053
0.54	...	0.477	1.223	1.025	0.313	0.200	-0.065
0.58	...	0.324	1.215	1.113	0.331	0.228	-0.059
0.62	...	0.198	1.187	1.178	0.368	0.252	-0.046
0.66	...	0.070	1.164	1.223	0.423	0.270	-0.030
0.70	...	-0.049	1.141	1.262	0.474	0.288	-0.017
0.80	...	-1.096	1.042	1.350	0.603	0.328	0.020
0.90	...	...	0.866	1.304	0.770	0.384	0.047
1.00	...	...	0.707	1.257	0.944	0.414	0.096
1.10	...	...	0.479	1.201	1.104	0.461	0.158
1.20	...	...	0.248	1.160	1.213	0.530	0.197
1.30	...	...	0.059	1.107	1.304	0.591	0.229
1.40	...	...	-0.097	1.022	1.380	0.668	0.260
1.50	...	...	-0.203	0.916	1.424	0.746	0.278
1.60	...	...	-0.268	0.744	1.479	0.841	0.276
1.70	...	...	-0.310	0.590	1.495	0.922	0.309
1.80	...	...	...	0.409	1.530	0.987	0.330
1.90	...	...	...	0.233	1.516	1.087	0.375
2.00	...	...	...	0.071	1.480	1.193	0.398
2.20	...	...	...	-0.144	1.286	1.400	0.443
2.40	...	...	...	-0.276	1.051	1.518	0.583
2.60	...	...	...	0.876	0.783	1.613	0.678
2.80	...	...	...	...	0.566	1.549	0.872
3.00	...	...	...	...	0.316	1.448	1.069
3.20	...	...	...	...	0.103	1.346	1.179
3.40	...	...	...	...	-0.089	1.240	1.321
3.60	...	...	...	...	-0.215	1.109	1.526
3.80	...	...	...	...	-0.334	1.038	1.577
4.00	...	...	...	...	-0.412	0.882	1.528

Table A-13: K-corrections for VCC 1972

z	K(UV_{218})	K(U_{300})	K(B_{450})	K(V_{606})	K(I_{814})	K(J_{110})	K(H_{160})	K(K_{222})
0.02	-0.001	0.026	0.021	0.002	-0.001	-0.008	-0.017	-0.055
0.04	-0.005	0.050	0.048	0.005	-0.002	-0.015	-0.031	-0.105
0.06	-0.010	0.071	0.075	0.008	-0.002	-0.022	-0.042	-0.154
0.08	-0.017	0.091	0.108	0.012	0.000	-0.028	-0.050	-0.201
0.10	-0.025	0.110	0.146	0.018	0.001	-0.034	-0.056	-0.245
0.12	-0.033	0.128	0.187	0.024	0.001	-0.039	-0.061	-0.290
0.14	-0.040	0.145	0.231	0.030	0.001	-0.044	-0.067	-0.333
0.16	-0.045	0.161	0.275	0.037	0.001	-0.048	-0.073	-0.376
0.18	-0.047	0.175	0.314	0.043	-0.001	-0.052	-0.078	-0.420
0.20	-0.047	0.186	0.347	0.052	-0.001	-0.056	-0.085	-0.463
0.22	-0.045	0.197	0.391	0.062	-0.002	-0.060	-0.092	-0.505
0.24	-0.041	0.205	0.442	0.074	-0.003	-0.063	-0.099	-0.545
0.26	-0.036	0.212	0.492	0.087	-0.003	-0.066	-0.107	-0.583
0.28	-0.030	0.218	0.553	0.102	-0.003	-0.069	-0.114	-0.619
0.30	-0.022	0.222	0.604	0.120	-0.002	-0.071	-0.121	-0.651
0.32	-0.013	0.225	0.654	0.137	-0.001	-0.073	-0.129	-0.681
0.34	-0.006	0.227	0.705	0.157	0.002	-0.076	-0.136	-0.705
0.36	0.002	0.227	0.755	0.179	0.006	-0.077	-0.144	-0.722
0.38	0.009	0.226	0.791	0.201	0.013	-0.078	-0.151	-0.733
0.40	...	0.224	0.813	0.222	0.017	-0.079	-0.159	-0.741
0.42	...	0.222	0.829	0.245	0.021	-0.080	-0.166	-0.744
0.44	...	0.220	0.843	0.270	0.025	-0.080	-0.173	-0.745
0.46	...	0.218	0.859	0.298	0.032	-0.080	-0.179	-0.746
0.48	...	0.216	0.876	0.324	0.036	-0.080	-0.185	-0.746
0.50	...	0.215	0.891	0.353	0.037	-0.079	-0.192	-0.746
0.54	...	0.214	0.921	0.413	0.040	-0.077	-0.204	-0.750
0.58	...	0.216	0.953	0.476	0.045	-0.075	-0.215	-0.757
0.62	...	0.220	0.980	0.540	0.059	-0.073	-0.224	-0.768
0.66	...	0.226	1.007	0.604	0.082	-0.072	-0.231	-0.779
0.70	...	0.231	1.034	0.668	0.091	-0.072	-0.237	-0.790
0.80	...	...	1.091	0.837	0.134	-0.067	-0.247	-0.825
0.90	...	...	1.116	0.954	0.221	-0.053	-0.251	-0.849
1.00	...	...	1.145	1.020	0.374	-0.043	-0.248	-0.868
1.10	...	...	1.150	1.075	0.519	-0.024	-0.248	-0.896
1.20	...	...	1.142	1.126	0.647	0.009	-0.249	-0.922
1.30	...	...	1.136	1.169	0.761	0.047	-0.249	-0.942
1.40	...	...	1.127	1.203	0.861	0.086	-0.249	-0.958
1.50	...	...	1.126	1.226	0.943	0.133	-0.250	-0.955
1.60	...	...	1.130	1.241	1.011	0.189	-0.249	-0.940
1.70	...	...	1.136	1.248	1.048	0.244	-0.242	-0.944
1.80	...	...	...	1.252	1.092	0.300	-0.237	-0.949
1.90	...	...	...	1.250	1.129	0.359	-0.228	-0.953
2.00	...	...	...	1.249	1.168	0.426	-0.220	-0.950
2.20	...	...	...	1.250	1.225	0.577	-0.195	-0.952
2.40	...	...	...	1.247	1.268	0.725	-0.158	-0.944
2.60	...	...	...	...	1.273	0.869	-0.125	-0.952
2.80	...	...	...	...	1.271	0.966	-0.044	-0.958
3.00	...	...	...	...	1.248	1.016	0.085	-0.944
3.20	...	...	...	...	1.236	1.059	0.206	-0.905
3.40	...	...	...	...	1.239	1.096	0.356	-0.882
3.60	...	...	...	...	1.266	1.122	0.519	-0.886
3.80	...	...	...	...	1.282	1.146	0.645	-0.895
4.00	...	...	...	...	1.286	1.162	0.701	-0.818

Table A-14: Colors for VCC 1972

z	$(UV-U)$	$(U-B)$	$(B-V)$	$(V-I)$	$(I-J)$	$(J-H)$	$(H-K)$
0.02	0.238	0.918	0.125	0.024	-0.167	-0.156	-0.657
0.04	0.211	0.915	0.149	0.028	-0.160	-0.149	-0.622
0.06	0.184	0.909	0.173	0.031	-0.153	-0.145	-0.584
0.08	0.158	0.896	0.201	0.033	-0.145	-0.143	-0.545
0.10	0.131	0.878	0.233	0.037	-0.138	-0.143	-0.506
0.12	0.105	0.855	0.268	0.044	-0.134	-0.143	-0.467
0.14	0.081	0.828	0.305	0.050	-0.129	-0.141	-0.429
0.16	0.060	0.800	0.343	0.057	-0.124	-0.140	-0.392
0.18	0.044	0.775	0.375	0.065	-0.121	-0.139	-0.353
0.20	0.031	0.753	0.400	0.074	-0.118	-0.137	-0.317
0.22	0.023	0.720	0.434	0.085	-0.116	-0.133	-0.281
0.24	0.018	0.678	0.474	0.097	-0.113	-0.129	-0.249
0.26	0.016	0.635	0.510	0.110	-0.110	-0.125	-0.218
0.28	0.017	0.580	0.556	0.125	-0.107	-0.120	-0.190
0.30	0.020	0.533	0.589	0.142	-0.104	-0.115	-0.164
0.32	0.026	0.486	0.621	0.158	-0.100	-0.110	-0.142
0.34	0.032	0.437	0.653	0.176	-0.096	-0.104	-0.125
0.36	0.039	0.387	0.681	0.193	-0.090	-0.098	-0.116
0.38	0.047	0.350	0.696	0.208	-0.083	-0.092	-0.111
0.40	-2.270	0.325	0.697	0.225	-0.077	-0.086	-0.111
0.42	...	0.307	0.690	0.245	-0.072	-0.079	-0.115
0.44	...	0.291	0.680	0.266	-0.069	-0.072	-0.120
0.46	...	0.273	0.669	0.286	-0.061	-0.066	-0.126
0.48	...	0.254	0.659	0.308	-0.058	-0.059	-0.132
0.50	...	0.238	0.645	0.336	-0.056	-0.053	-0.139
0.54	...	0.207	0.615	0.393	-0.056	-0.038	-0.148
0.58	...	0.177	0.585	0.451	-0.054	-0.024	-0.151
0.62	...	0.154	0.548	0.501	-0.041	-0.014	-0.150
0.66	...	0.132	0.511	0.542	-0.020	-0.006	-0.146
0.70	...	0.110	0.473	0.597	-0.011	0.001	-0.140
0.80	...	-1.079	0.362	0.723	0.027	0.015	-0.116
0.90	...	...	0.270	0.754	0.100	0.033	-0.096
1.00	...	...	0.231	0.669	0.243	0.039	-0.073
1.10	...	...	0.182	0.578	0.369	0.059	-0.045
1.20	...	...	0.123	0.500	0.465	0.093	-0.021
1.30	...	...	0.074	0.430	0.541	0.130	0.000
1.40	...	...	0.031	0.364	0.601	0.170	0.016
1.50	...	...	0.006	0.305	0.637	0.217	0.012
1.60	...	...	-0.005	0.251	0.650	0.272	-0.002
1.70	...	...	-0.006	0.221	0.631	0.321	0.009
1.80	...	...	...	0.182	0.619	0.372	0.019
1.90	...	...	...	0.142	0.598	0.421	0.032
2.00	...	...	...	0.102	0.570	0.480	0.036
2.20	...	...	...	0.047	0.475	0.607	0.064
2.40	...	...	...	0.000	0.370	0.718	0.092
2.60	...	...	...	0.893	0.231	0.828	0.133
2.80	...	...	...	...	0.132	0.846	0.219
3.00	...	...	...	...	0.059	0.767	0.334
3.20	...	...	...	...	0.004	0.689	0.417
3.40	...	...	...	...	-0.031	0.576	0.543
3.60	...	...	...	...	-0.029	0.439	0.710
3.80	...	...	...	...	-0.037	0.337	0.846
4.00	...	...	...	...	-0.050	0.297	0.826

Table A-15: K-corrections for VCC 1987

z	$K(UV_{218})$	$K(U_{300})$	$K(B_{450})$	$K(V_{606})$	$K(I_{814})$	$K(J_{110})$	$K(H_{160})$	$K(K_{222})$
0.02	-0.001	0.025	0.020	0.001	-0.002	-0.008	-0.018	-0.055
0.04	-0.005	0.048	0.047	0.003	-0.003	-0.016	-0.032	-0.105
0.06	-0.010	0.068	0.073	0.005	-0.004	-0.024	-0.043	-0.154
0.08	-0.016	0.087	0.105	0.009	-0.002	-0.030	-0.052	-0.201
0.10	-0.024	0.105	0.142	0.013	-0.002	-0.037	-0.058	-0.246
0.12	-0.032	0.123	0.182	0.019	-0.004	-0.042	-0.064	-0.290
0.14	-0.039	0.139	0.225	0.024	-0.004	-0.047	-0.070	-0.334
0.16	-0.044	0.154	0.269	0.030	-0.004	-0.052	-0.076	-0.377
0.18	-0.046	0.168	0.307	0.035	-0.007	-0.057	-0.082	-0.421
0.20	-0.046	0.179	0.340	0.043	-0.008	-0.061	-0.089	-0.464
0.22	-0.044	0.189	0.383	0.052	-0.010	-0.065	-0.096	-0.507
0.24	-0.040	0.197	0.434	0.063	-0.011	-0.069	-0.104	-0.546
0.26	-0.035	0.204	0.483	0.075	-0.012	-0.073	-0.112	-0.584
0.28	-0.028	0.209	0.544	0.090	-0.012	-0.076	-0.119	-0.620
0.30	-0.020	0.213	0.594	0.107	-0.012	-0.079	-0.127	-0.653
0.32	-0.011	0.216	0.643	0.124	-0.011	-0.081	-0.135	-0.683
0.34	-0.003	0.218	0.694	0.143	-0.010	-0.084	-0.143	-0.707
0.36	0.004	0.218	0.743	0.165	-0.006	-0.086	-0.151	-0.724
0.38	0.011	0.217	0.778	0.186	0.000	-0.087	-0.158	-0.736
0.40	...	0.215	0.798	0.206	0.003	-0.089	-0.166	-0.744
0.42	...	0.213	0.814	0.229	0.007	-0.090	-0.174	-0.747
0.44	...	0.211	0.827	0.253	0.009	-0.091	-0.181	-0.749
0.46	...	0.209	0.843	0.280	0.016	-0.091	-0.188	-0.750
0.48	...	0.207	0.859	0.306	0.019	-0.091	-0.194	-0.751
0.50	...	0.206	0.874	0.335	0.020	-0.092	-0.201	-0.751
0.54	...	0.205	0.902	0.394	0.021	-0.090	-0.214	-0.755
0.58	...	0.208	0.933	0.455	0.025	-0.089	-0.226	-0.763
0.62	...	0.212	0.959	0.518	0.038	-0.089	-0.235	-0.774
0.66	...	0.217	0.985	0.581	0.059	-0.088	-0.243	-0.786
0.70	...	0.223	1.010	0.645	0.067	-0.089	-0.250	-0.798
0.80	...	...	1.065	0.811	0.107	-0.086	-0.261	-0.833
0.90	...	...	1.089	0.925	0.193	-0.075	-0.267	-0.859
1.00	...	...	1.117	0.989	0.344	-0.067	-0.265	-0.879
1.10	...	...	1.122	1.042	0.488	-0.050	-0.267	-0.909
1.20	...	...	1.114	1.090	0.614	-0.019	-0.270	-0.936
1.30	...	...	1.109	1.131	0.726	0.016	-0.271	-0.957
1.40	...	...	1.100	1.164	0.823	0.054	-0.274	-0.974
1.50	...	...	1.099	1.186	0.904	0.099	-0.276	-0.972
1.60	...	...	1.104	1.201	0.969	0.153	-0.277	-0.959
1.70	...	...	1.110	1.207	1.004	0.207	-0.271	-0.964
1.80	...	...	...	1.211	1.046	0.262	-0.268	-0.970
1.90	...	...	...	1.209	1.082	0.319	-0.260	-0.976
2.00	...	...	...	1.208	1.119	0.384	-0.254	-0.973
2.20	...	...	...	1.210	1.174	0.533	-0.233	-0.979
2.40	...	...	...	1.207	1.215	0.678	-0.199	-0.972
2.60	...	...	...	...	1.220	0.820	-0.168	-0.983
2.80	...	...	...	...	1.218	0.914	-0.091	-0.991
3.00	...	...	...	...	1.196	0.962	0.036	-0.979
3.20	...	...	...	...	1.184	1.003	0.156	-0.944
3.40	...	...	...	...	1.187	1.038	0.305	-0.922
3.60	...	...	...	...	1.215	1.063	0.466	-0.928
3.80	...	...	...	...	1.231	1.086	0.590	-0.940
4.00	...	...	...	...	1.235	1.101	0.643	-0.866

Table A-16: Colors for VCC 1987

z	$(UV-U)$	$(U-B)$	$(B-V)$	$(V-I)$	$(I-J)$	$(J-H)$	$(H-K)$
0.02	0.229	0.899	0.112	0.012	-0.176	-0.165	-0.661
0.04	0.203	0.896	0.136	0.016	-0.169	-0.158	-0.625
0.06	0.178	0.890	0.160	0.019	-0.163	-0.154	-0.588
0.08	0.152	0.877	0.188	0.021	-0.155	-0.152	-0.549
0.10	0.126	0.859	0.220	0.025	-0.148	-0.152	-0.511
0.12	0.101	0.836	0.255	0.031	-0.144	-0.152	-0.472
0.14	0.077	0.810	0.292	0.037	-0.139	-0.151	-0.434
0.16	0.057	0.781	0.331	0.043	-0.135	-0.150	-0.397
0.18	0.042	0.756	0.363	0.051	-0.132	-0.149	-0.359
0.20	0.030	0.735	0.389	0.060	-0.129	-0.146	-0.323
0.22	0.022	0.702	0.423	0.071	-0.127	-0.143	-0.288
0.24	0.018	0.659	0.462	0.083	-0.125	-0.139	-0.256
0.26	0.016	0.618	0.499	0.096	-0.122	-0.135	-0.225
0.28	0.017	0.563	0.545	0.111	-0.119	-0.130	-0.197
0.30	0.021	0.516	0.579	0.128	-0.116	-0.126	-0.171
0.32	0.027	0.469	0.611	0.144	-0.113	-0.120	-0.149
0.34	0.033	0.420	0.643	0.162	-0.108	-0.115	-0.133
0.36	0.041	0.372	0.670	0.179	-0.103	-0.109	-0.124
0.38	0.049	0.335	0.684	0.195	-0.096	-0.102	-0.119
0.40	-2.270	0.312	0.685	0.212	-0.090	-0.096	-0.119
0.42	...	0.294	0.678	0.231	-0.086	-0.090	-0.123
0.44	...	0.279	0.668	0.252	-0.082	-0.083	-0.128
0.46	...	0.261	0.656	0.273	-0.075	-0.077	-0.134
0.48	...	0.244	0.647	0.295	-0.072	-0.071	-0.140
0.50	...	0.228	0.633	0.323	-0.070	-0.064	-0.147
0.54	...	0.199	0.602	0.381	-0.071	-0.050	-0.155
0.58	...	0.170	0.572	0.438	-0.068	-0.037	-0.159
0.62	...	0.148	0.534	0.489	-0.056	-0.027	-0.157
0.66	...	0.127	0.498	0.531	-0.035	-0.019	-0.154
0.70	...	0.107	0.460	0.586	-0.027	-0.013	-0.149
0.80	...	-1.079	0.349	0.713	0.011	0.001	-0.125
0.90	...	...	0.258	0.742	0.084	0.018	-0.105
1.00	...	...	0.222	0.656	0.228	0.024	-0.082
1.10	...	...	0.174	0.565	0.354	0.043	-0.055
1.20	...	...	0.118	0.486	0.450	0.077	-0.031
1.30	...	...	0.071	0.416	0.526	0.114	-0.011
1.40	...	...	0.030	0.351	0.586	0.154	0.004
1.50	...	...	0.006	0.293	0.622	0.201	+0.001
1.60	...	...	-0.004	0.242	0.634	0.256	-0.014
1.70	...	...	-0.004	0.213	0.615	0.304	-0.004
1.80	...	...	...	0.175	0.602	0.356	0.006
1.90	...	...	...	0.137	0.581	0.405	0.019
2.00	...	...	...	0.098	0.553	0.464	0.022
2.20	...	...	...	0.046	0.459	0.592	0.049
2.40	...	...	...	0.001	0.355	0.704	0.076
2.60	...	...	...	0.893	0.219	0.814	0.117
2.80	...	...	...	...	0.123	0.831	0.203
3.00	...	...	...	...	0.052	0.752	0.318
3.20	...	...	...	...	-0.001	0.674	0.403
3.40	...	...	...	...	-0.034	0.561	0.530
3.60	...	...	...	...	-0.031	0.424	0.697
3.80	...	...	...	...	-0.037	0.323	0.833
4.00	...	...	...	...	-0.048	0.285	0.813

Table A-17: K-corrections for M 82

z	$K(UV_{218})$	$K(U_{300})$	$K(B_{450})$	$K(V_{606})$	$K(I_{814})$	$K(J_{110})$	$K(H_{160})$	$K(K_{222})$
0.02	0.000	0.016	0.019	0.007	0.011	0.002	-0.008	-0.042
0.04	-0.003	0.030	0.041	0.015	0.023	0.004	-0.014	-0.081
0.06	-0.009	0.043	0.063	0.022	0.035	0.007	-0.017	-0.120
0.08	-0.018	0.054	0.089	0.030	0.048	0.011	-0.017	-0.158
0.10	-0.028	0.066	0.117	0.039	0.058	0.016	-0.016	-0.195
0.12	-0.039	0.078	0.147	0.048	0.066	0.021	-0.014	-0.233
0.14	-0.048	0.089	0.178	0.057	0.076	0.027	-0.014	-0.270
0.16	-0.056	0.100	0.210	0.065	0.083	0.033	-0.014	-0.307
0.18	-0.062	0.110	0.235	0.073	0.090	0.039	-0.014	-0.345
0.20	-0.066	0.118	0.257	0.083	0.096	0.045	-0.015	-0.382
0.22	-0.068	0.126	0.288	0.094	0.101	0.051	-0.017	-0.419
0.24	-0.068	0.132	0.324	0.106	0.106	0.057	-0.019	-0.454
0.26	-0.067	0.136	0.359	0.119	0.110	0.063	-0.020	-0.486
0.28	-0.065	0.140	0.400	0.133	0.115	0.069	-0.021	-0.515
0.30	-0.062	0.142	0.434	0.149	0.120	0.075	-0.022	-0.542
0.32	-0.059	0.142	0.467	0.165	0.125	0.081	-0.024	-0.564
0.34	-0.056	0.142	0.502	0.182	0.131	0.087	-0.025	-0.580
0.36	-0.053	0.140	0.533	0.200	0.138	0.094	-0.025	-0.589
0.38	-0.051	0.138	0.552	0.217	0.147	0.101	-0.024	-0.592
0.40	...	0.135	0.566	0.233	0.154	0.107	-0.024	-0.590
0.42	...	0.132	0.576	0.252	0.161	0.114	-0.023	-0.585
0.44	...	0.129	0.587	0.270	0.167	0.121	-0.022	-0.578
0.46	...	0.126	0.600	0.291	0.176	0.129	-0.020	-0.572
0.48	...	0.123	0.613	0.310	0.182	0.136	-0.018	-0.565
0.50	...	0.121	0.625	0.332	0.187	0.143	-0.016	-0.560
0.54	...	0.116	0.647	0.375	0.196	0.159	-0.013	-0.555
0.58	...	0.114	0.669	0.419	0.206	0.175	-0.010	-0.554
0.62	...	0.112	0.685	0.464	0.224	0.188	-0.005	-0.559
0.66	...	0.111	0.701	0.507	0.247	0.200	0.002	-0.565
0.70	...	0.110	0.716	0.552	0.257	0.210	0.009	-0.574
0.80	...	...	0.750	0.662	0.296	0.235	0.032	-0.592
0.90	...	...	0.766	0.738	0.367	0.264	0.061	-0.586
1.00	...	...	0.781	0.781	0.477	0.285	0.099	-0.570
1.10	...	...	0.784	0.819	0.574	0.311	0.131	-0.565
1.20	...	...	0.781	0.853	0.659	0.345	0.157	-0.564
1.30	...	...	0.776	0.880	0.739	0.380	0.179	-0.565
1.40	...	...	0.758	0.900	0.809	0.415	0.197	-0.564
1.50	...	...	0.744	0.913	0.866	0.456	0.212	-0.536
1.60	...	...	0.737	0.920	0.910	0.504	0.224	-0.492
1.70	...	...	0.734	0.922	0.936	0.548	0.240	-0.467
1.80	...	...	...	0.923	0.962	0.592	0.253	-0.444
1.90	...	...	...	0.921	0.982	0.636	0.268	-0.426
2.00	...	...	...	0.918	1.001	0.685	0.282	-0.406
2.20	...	...	...	0.909	1.036	0.788	0.318	-0.372
2.40	...	...	...	0.891	1.076	0.884	0.359	-0.340
2.60	...	...	...	...	1.080	0.977	0.393	-0.328
2.80	...	...	...	...	1.070	1.039	0.460	-0.322
3.00	...	...	...	...	1.045	1.073	0.553	-0.305
3.20	...	...	...	...	1.029	1.104	0.633	-0.261
3.40	...	...	...	...	1.024	1.126	0.737	-0.227
3.60	...	...	...	...	1.032	1.140	0.846	-0.219
3.80	...	...	...	...	1.033	1.150	0.927	-0.215
4.00	...	...	...	...	1.030	1.155	0.964	-0.145

Table A-18: Colors for M 82

z	$(UV-U)$	$(U-B)$	$(B-V)$	$(V-I)$	$(I-J)$	$(J-H)$	$(H-K)$
0.02	0.163	0.638	0.153	0.143	0.027	0.006	-0.516
0.04	0.146	0.629	0.168	0.139	0.036	0.014	-0.483
0.06	0.128	0.620	0.182	0.134	0.045	0.020	-0.447
0.08	0.107	0.607	0.200	0.130	0.054	0.025	-0.409
0.10	0.086	0.590	0.219	0.128	0.060	0.028	-0.371
0.12	0.063	0.572	0.240	0.128	0.063	0.032	-0.331
0.14	0.042	0.552	0.262	0.128	0.067	0.037	-0.294
0.16	0.023	0.532	0.286	0.128	0.068	0.043	-0.256
0.18	0.007	0.516	0.302	0.131	0.068	0.049	-0.219
0.20	-0.005	0.502	0.315	0.134	0.069	0.056	-0.183
0.22	-0.014	0.479	0.335	0.139	0.068	0.064	-0.147
0.24	-0.021	0.449	0.359	0.147	0.067	0.071	-0.115
0.26	-0.025	0.419	0.381	0.155	0.066	0.079	-0.084
0.28	-0.026	0.381	0.408	0.165	0.064	0.086	-0.056
0.30	-0.025	0.350	0.425	0.176	0.063	0.094	-0.030
0.32	-0.023	0.317	0.443	0.187	0.062	0.101	-0.008
0.34	-0.020	0.282	0.461	0.198	0.061	0.108	0.007
0.36	-0.015	0.250	0.474	0.208	0.062	0.115	0.016
0.38	-0.011	0.227	0.477	0.216	0.064	0.121	0.020
0.40	-2.273	0.211	0.474	0.226	0.064	0.127	0.019
0.42	...	0.197	0.467	0.238	0.064	0.134	0.014
0.44	...	0.183	0.459	0.250	0.064	0.139	0.008
0.46	...	0.167	0.451	0.261	0.066	0.145	0.004
0.48	...	0.152	0.444	0.274	0.064	0.150	-0.001
0.50	...	0.137	0.435	0.291	0.062	0.156	-0.004
0.54	...	0.110	0.414	0.326	0.054	0.169	-0.006
0.58	...	0.085	0.392	0.359	0.050	0.181	-0.004
0.62	...	0.067	0.364	0.386	0.054	0.189	0.006
0.66	...	0.051	0.336	0.407	0.065	0.195	0.019
0.70	...	0.034	0.307	0.440	0.065	0.198	0.034
0.80	...	-1.083	0.230	0.513	0.078	0.200	0.075
0.90	...	...	0.171	0.518	0.121	0.199	0.099
1.00	...	...	0.142	0.452	0.209	0.183	0.121
1.10	...	...	0.108	0.393	0.280	0.176	0.148
1.20	...	...	0.070	0.341	0.332	0.184	0.173
1.30	...	...	0.038	0.289	0.376	0.197	0.196
1.40	...	...	0.000	0.239	0.412	0.214	0.213
1.50	...	...	-0.027	0.194	0.428	0.241	0.201
1.60	...	...	-0.040	0.157	0.425	0.275	0.169
1.70	...	...	-0.046	0.133	0.406	0.305	0.159
1.80	...	...	...	0.108	0.388	0.336	0.148
1.90	...	...	...	0.086	0.364	0.364	0.145
2.00	...	...	...	0.064	0.335	0.399	0.139
2.20	...	...	...	0.020	0.266	0.467	0.141
2.40	...	...	...	-0.037	0.209	0.521	0.151
2.60	...	...	...	0.891	0.121	0.580	0.173
2.80	...	...	...	...	0.050	0.576	0.233
3.00	...	...	...	...	-0.010	0.517	0.309
3.20	...	...	...	...	-0.057	0.467	0.346
3.40	...	...	...	...	-0.084	0.386	0.416
3.60	...	...	...	...	-0.090	0.291	0.516
3.80	...	...	...	...	-0.099	0.220	0.594
4.00	...	...	...	...	-0.108	0.188	0.562

Table A-19: K-corrections for Arp 220

z	$K(UV_{218})$	$K(U_{300})$	$K(B_{450})$	$K(V_{606})$	$K(I_{814})$	$K(J_{110})$	$K(H_{160})$	$K(K_{222})$
0.02	-0.002	0.024	0.027	0.014	0.019	0.010	0.004	-0.020
0.04	-0.007	0.046	0.057	0.030	0.039	0.020	0.010	-0.040
0.06	-0.018	0.067	0.087	0.044	0.058	0.031	0.018	-0.062
0.08	-0.033	0.086	0.119	0.060	0.078	0.043	0.028	-0.085
0.10	-0.051	0.105	0.154	0.076	0.095	0.055	0.039	-0.108
0.12	-0.071	0.123	0.190	0.093	0.110	0.068	0.050	-0.132
0.14	-0.090	0.140	0.228	0.110	0.126	0.081	0.059	-0.157
0.16	-0.107	0.157	0.264	0.126	0.140	0.095	0.066	-0.182
0.18	-0.122	0.172	0.294	0.143	0.151	0.109	0.074	-0.210
0.20	-0.134	0.185	0.319	0.161	0.163	0.122	0.080	-0.236
0.22	-0.144	0.197	0.352	0.180	0.174	0.134	0.085	-0.262
0.24	-0.151	0.206	0.391	0.201	0.184	0.146	0.091	-0.284
0.26	-0.156	0.214	0.430	0.222	0.194	0.158	0.096	-0.303
0.28	-0.159	0.219	0.474	0.244	0.204	0.170	0.102	-0.319
0.30	-0.161	0.222	0.507	0.266	0.214	0.181	0.107	-0.332
0.32	-0.162	0.223	0.541	0.288	0.224	0.193	0.113	-0.342
0.34	-0.163	0.222	0.575	0.311	0.235	0.204	0.119	-0.347
0.36	-0.165	0.219	0.607	0.335	0.249	0.216	0.125	-0.345
0.38	-0.166	0.214	0.630	0.357	0.263	0.228	0.133	-0.338
0.40	...	0.208	0.649	0.379	0.276	0.240	0.140	-0.327
0.42	...	0.201	0.666	0.402	0.289	0.252	0.147	-0.313
0.44	...	0.193	0.684	0.425	0.301	0.265	0.155	-0.298
0.46	...	0.186	0.704	0.450	0.315	0.277	0.164	-0.283
0.48	...	0.178	0.724	0.475	0.327	0.289	0.173	-0.269
0.50	...	0.171	0.743	0.501	0.338	0.302	0.181	-0.256
0.54	...	0.157	0.779	0.552	0.359	0.329	0.196	-0.238
0.58	...	0.145	0.813	0.603	0.381	0.355	0.210	-0.226
0.62	...	0.136	0.840	0.654	0.413	0.378	0.224	-0.220
0.66	...	0.127	0.865	0.702	0.450	0.399	0.239	-0.218
0.70	...	0.118	0.889	0.751	0.474	0.418	0.255	-0.218
0.80	...	...	0.942	0.873	0.545	0.466	0.298	-0.218
0.90	...	...	0.970	0.963	0.639	0.515	0.348	-0.182
1.00	...	...	0.992	1.028	0.754	0.557	0.407	-0.134
1.10	...	...	0.993	1.090	0.856	0.602	0.460	-0.105
1.20	...	...	0.981	1.143	0.949	0.653	0.504	-0.087
1.30	...	...	0.962	1.186	1.039	0.705	0.542	-0.074
1.40	...	...	0.929	1.218	1.122	0.757	0.575	-0.063
1.50	...	...	0.897	1.239	1.194	0.815	0.603	-0.021
1.60	...	...	0.875	1.250	1.256	0.878	0.628	0.042
1.70	...	...	0.854	1.251	1.298	0.936	0.656	0.085
1.80	...	...	...	1.247	1.341	0.993	0.683	0.125
1.90	...	...	...	1.237	1.376	1.050	0.711	0.157
2.00	...	...	...	1.226	1.407	1.112	0.740	0.190
2.20	...	...	...	1.198	1.461	1.236	0.807	0.247
2.40	...	...	...	1.156	1.519	1.346	0.883	0.296
2.60	...	...	...	...	1.526	1.451	0.947	0.328
2.80	...	...	...	...	1.511	1.529	1.038	0.349
3.00	...	...	...	...	1.463	1.586	1.147	0.386
3.20	...	...	...	...	1.422	1.634	1.235	0.456
3.40	...	...	...	...	1.396	1.670	1.345	0.512
3.60	...	...	...	...	1.396	1.690	1.454	0.539
3.80	...	...	...	...	1.384	1.703	1.539	0.567
4.00	...	...	...	...	1.363	1.709	1.596	0.667

Table A-20: Colors for Arp 220

z	$(UV-U)$	$(U-B)$	$(B-V)$	$(V-I)$	$(I-J)$	$(J-H)$	$(H-K)$
0.02	0.244	0.765	0.279	0.247	0.163	0.178	-0.273
0.04	0.216	0.757	0.294	0.243	0.172	0.182	-0.247
0.06	0.186	0.749	0.308	0.238	0.181	0.185	-0.217
0.08	0.152	0.736	0.325	0.235	0.189	0.187	-0.185
0.10	0.115	0.720	0.344	0.234	0.194	0.188	-0.151
0.12	0.077	0.702	0.363	0.235	0.196	0.190	-0.116
0.14	0.040	0.682	0.383	0.237	0.198	0.195	-0.082
0.16	0.006	0.662	0.404	0.239	0.199	0.200	-0.049
0.18	-0.024	0.648	0.417	0.244	0.197	0.207	-0.015
0.20	-0.050	0.636	0.424	0.250	0.196	0.214	0.018
0.22	-0.071	0.614	0.438	0.258	0.194	0.221	0.049
0.24	-0.088	0.585	0.456	0.269	0.192	0.227	0.077
0.26	-0.101	0.554	0.474	0.280	0.190	0.234	0.101
0.28	-0.109	0.515	0.496	0.291	0.188	0.240	0.123
0.30	-0.114	0.484	0.507	0.304	0.187	0.246	0.142
0.32	-0.116	0.452	0.519	0.316	0.185	0.252	0.159
0.34	-0.117	0.417	0.530	0.327	0.185	0.257	0.170
0.36	-0.115	0.382	0.538	0.338	0.187	0.263	0.175
0.38	-0.112	0.354	0.540	0.346	0.189	0.268	0.175
0.40	-2.278	0.328	0.537	0.355	0.190	0.272	0.171
0.42	...	0.304	0.531	0.365	0.191	0.277	0.165
0.44	...	0.279	0.526	0.376	0.191	0.281	0.157
0.46	...	0.252	0.520	0.387	0.193	0.285	0.151
0.48	...	0.224	0.516	0.399	0.192	0.289	0.145
0.50	...	0.197	0.509	0.414	0.190	0.293	0.141
0.54	...	0.147	0.494	0.445	0.184	0.305	0.138
0.58	...	0.101	0.477	0.473	0.181	0.317	0.139
0.62	...	0.065	0.454	0.493	0.189	0.326	0.148
0.66	...	0.031	0.431	0.504	0.204	0.332	0.161
0.70	...	-0.002	0.406	0.528	0.209	0.336	0.177
0.80	...	-1.086	0.337	0.580	0.233	0.340	0.219
0.90	...	...	0.275	0.576	0.277	0.340	0.234
1.00	...	...	0.231	0.527	0.351	0.322	0.244
1.10	...	...	0.171	0.486	0.407	0.314	0.269
1.20	...	...	0.105	0.447	0.450	0.321	0.295
1.30	...	...	0.044	0.400	0.488	0.334	0.320
1.40	...	...	-0.022	0.348	0.519	0.354	0.341
1.50	...	...	-0.074	0.298	0.533	0.384	0.328
1.60	...	...	-0.108	0.247	0.532	0.422	0.290
1.70	...	...	-0.130	0.205	0.517	0.451	0.276
1.80	...	...	...	0.159	0.502	0.482	0.262
1.90	...	...	...	0.114	0.480	0.511	0.259
2.00	...	...	...	0.072	0.449	0.544	0.254
2.20	...	...	...	-0.010	0.380	0.601	0.264
2.40	...	...	...	-0.110	0.327	0.635	0.290
2.60	...	...	...	0.886	0.230	0.676	0.323
2.80	...	...	...	...	0.136	0.664	0.392
3.00	...	...	...	...	0.032	0.612	0.465
3.20	...	...	...	...	-0.058	0.572	0.483
3.40	...	...	...	...	-0.120	0.498	0.536
3.60	...	...	...	...	-0.140	0.408	0.619
3.80	...	...	...	...	-0.165	0.337	0.676
4.00	...	...	...	...	-0.191	0.286	0.633

Table A-21: K-corrections for Mrk 273

z	$K(UV_{218})$	$K(U_{300})$	$K(B_{450})$	$K(V_{606})$	$K(I_{814})$	$K(J_{110})$	$K(H_{160})$	$K(K_{222})$
0.02	-0.001	0.024	0.027	0.014	0.019	0.010	0.004	-0.020
0.04	-0.005	0.045	0.057	0.029	0.038	0.019	0.009	-0.040
0.06	-0.013	0.064	0.087	0.044	0.057	0.030	0.017	-0.062
0.08	-0.025	0.082	0.120	0.059	0.077	0.041	0.026	-0.085
0.10	-0.039	0.099	0.155	0.075	0.093	0.053	0.036	-0.108
0.12	-0.054	0.116	0.191	0.092	0.108	0.065	0.046	-0.133
0.14	-0.068	0.132	0.229	0.109	0.124	0.078	0.054	-0.157
0.16	-0.080	0.148	0.266	0.124	0.137	0.092	0.062	-0.183
0.18	-0.090	0.161	0.296	0.141	0.149	0.105	0.068	-0.210
0.20	-0.097	0.173	0.322	0.159	0.161	0.118	0.073	-0.238
0.22	-0.103	0.184	0.356	0.177	0.171	0.130	0.078	-0.263
0.24	-0.107	0.192	0.396	0.197	0.181	0.141	0.083	-0.286
0.26	-0.109	0.199	0.436	0.218	0.191	0.153	0.088	-0.305
0.28	-0.110	0.203	0.481	0.239	0.200	0.165	0.093	-0.322
0.30	-0.109	0.206	0.516	0.262	0.210	0.176	0.099	-0.335
0.32	-0.109	0.207	0.551	0.284	0.220	0.187	0.104	-0.346
0.34	-0.108	0.207	0.587	0.307	0.231	0.198	0.109	-0.351
0.36	-0.108	0.205	0.622	0.331	0.244	0.210	0.116	-0.350
0.38	-0.108	0.201	0.646	0.353	0.259	0.222	0.122	-0.343
0.40	...	0.197	0.666	0.375	0.271	0.234	0.129	-0.332
0.42	...	0.192	0.683	0.398	0.283	0.246	0.136	-0.318
0.44	...	0.187	0.701	0.422	0.296	0.258	0.144	-0.303
0.46	...	0.182	0.721	0.447	0.310	0.270	0.152	-0.289
0.48	...	0.178	0.741	0.472	0.321	0.282	0.161	-0.276
0.50	...	0.173	0.760	0.499	0.332	0.294	0.169	-0.263
0.54	...	0.164	0.795	0.551	0.352	0.321	0.183	-0.247
0.58	...	0.158	0.828	0.603	0.375	0.346	0.196	-0.235
0.62	...	0.152	0.853	0.654	0.406	0.369	0.210	-0.230
0.66	...	0.146	0.877	0.704	0.442	0.390	0.225	-0.229
0.70	...	0.141	0.898	0.754	0.466	0.409	0.240	-0.231
0.80	...	...	0.947	0.881	0.536	0.456	0.282	-0.231
0.90	...	...	0.970	0.974	0.628	0.504	0.331	-0.198
1.00	...	...	0.989	1.039	0.746	0.545	0.390	-0.151
1.10	...	...	0.992	1.098	0.852	0.590	0.442	-0.123
1.20	...	...	0.986	1.149	0.948	0.640	0.485	-0.106
1.30	...	...	0.976	1.188	1.042	0.691	0.523	-0.094
1.40	...	...	0.950	1.217	1.128	0.744	0.554	-0.083
1.50	...	...	0.926	1.235	1.202	0.802	0.582	-0.042
1.60	...	...	0.911	1.245	1.264	0.865	0.607	0.020
1.70	...	...	0.900	1.248	1.306	0.923	0.635	0.063
1.80	...	...	...	1.247	1.347	0.981	0.661	0.102
1.90	...	...	...	1.242	1.378	1.039	0.689	0.134
2.00	...	...	...	1.236	1.406	1.101	0.716	0.166
2.20	...	...	...	1.217	1.455	1.227	0.783	0.222
2.40	...	...	...	1.187	1.506	1.339	0.858	0.271
2.60	...	...	...	...	1.514	1.447	0.921	0.302
2.80	...	...	...	...	1.500	1.527	1.011	0.323
3.00	...	...	...	...	1.465	1.581	1.120	0.358
3.20	...	...	...	...	1.439	1.628	1.211	0.427
3.40	...	...	...	...	1.425	1.662	1.324	0.482
3.60	...	...	...	...	1.427	1.683	1.439	0.509
3.80	...	...	...	...	1.418	1.697	1.529	0.539
4.00	...	...	...	...	1.408	1.703	1.587	0.637

Table A-22: Colors for Mrk 273

z	$(UV-U)$	$(U-B)$	$(B-V)$	$(V-I)$	$(I-J)$	$(J-H)$	$(H-K)$
0.02	0.226	0.779	0.274	0.243	0.157	0.167	-0.279
0.04	0.201	0.771	0.290	0.239	0.166	0.171	-0.253
0.06	0.174	0.761	0.305	0.234	0.175	0.174	-0.224
0.08	0.144	0.746	0.322	0.231	0.183	0.177	-0.192
0.10	0.113	0.728	0.341	0.230	0.188	0.178	-0.159
0.12	0.081	0.709	0.361	0.231	0.190	0.180	-0.124
0.14	0.050	0.687	0.382	0.233	0.193	0.185	-0.091
0.16	0.023	0.666	0.403	0.235	0.193	0.191	-0.058
0.18	-0.001	0.649	0.417	0.240	0.192	0.198	-0.024
0.20	-0.021	0.635	0.425	0.246	0.191	0.205	0.008
0.22	-0.037	0.612	0.440	0.254	0.189	0.212	0.039
0.24	-0.049	0.581	0.460	0.264	0.187	0.219	0.066
0.26	-0.058	0.547	0.479	0.275	0.185	0.226	0.091
0.28	-0.063	0.507	0.502	0.287	0.183	0.232	0.113
0.30	-0.066	0.475	0.515	0.299	0.182	0.238	0.132
0.32	-0.067	0.441	0.529	0.311	0.180	0.244	0.148
0.34	-0.066	0.404	0.542	0.323	0.180	0.250	0.159
0.36	-0.063	0.368	0.553	0.334	0.182	0.256	0.164
0.38	-0.060	0.339	0.556	0.342	0.184	0.261	0.164
0.40	-2.275	0.315	0.553	0.352	0.185	0.266	0.161
0.42	...	0.293	0.547	0.362	0.185	0.270	0.154
0.44	...	0.270	0.542	0.374	0.185	0.275	0.147
0.46	...	0.246	0.536	0.385	0.187	0.279	0.141
0.48	...	0.221	0.531	0.398	0.187	0.283	0.135
0.50	...	0.197	0.524	0.414	0.185	0.287	0.131
0.54	...	0.154	0.507	0.445	0.179	0.299	0.129
0.58	...	0.114	0.488	0.475	0.176	0.311	0.130
0.62	...	0.083	0.462	0.495	0.184	0.320	0.139
0.66	...	0.053	0.435	0.509	0.199	0.326	0.153
0.70	...	0.026	0.407	0.535	0.205	0.330	0.169
0.80	...	-1.084	0.329	0.593	0.227	0.335	0.212
0.90	...	...	0.260	0.594	0.270	0.335	0.227
1.00	...	...	0.213	0.542	0.348	0.317	0.239
1.10	...	...	0.157	0.495	0.409	0.309	0.263
1.20	...	...	0.100	0.449	0.455	0.316	0.289
1.30	...	...	0.050	0.395	0.497	0.330	0.315
1.40	...	...	-0.005	0.338	0.532	0.350	0.336
1.50	...	...	-0.047	0.282	0.547	0.381	0.323
1.60	...	...	-0.072	0.230	0.547	0.419	0.286
1.70	...	...	-0.086	0.190	0.530	0.449	0.271
1.80	...	...	...	0.149	0.513	0.481	0.258
1.90	...	...	...	0.112	0.487	0.512	0.254
2.00	...	...	...	0.078	0.453	0.546	0.249
2.20	...	...	...	0.010	0.377	0.605	0.260
2.40	...	...	...	-0.071	0.315	0.642	0.285
2.60	...	...	...	0.888	0.215	0.687	0.318
2.80	...	...	...	...	0.121	0.677	0.386
3.00	...	...	...	...	0.032	0.623	0.461
3.20	...	...	...	...	-0.041	0.579	0.483
3.40	...	...	...	...	-0.090	0.500	0.541
3.60	...	...	...	...	-0.109	0.406	0.628
3.80	...	...	...	...	-0.131	0.329	0.689
4.00	...	...	...	...	-0.148	0.278	0.649

Table A-23: K-corrections for UGC 05101

z	$K(UV_{218})$	$K(U_{300})$	$K(B_{450})$	$K(V_{606})$	$K(I_{814})$	$K(J_{110})$	$K(H_{160})$	$K(K_{222})$
0.02	0.001	0.019	0.028	0.016	0.020	0.010	0.003	-0.022
0.04	0.000	0.036	0.058	0.032	0.039	0.020	0.008	-0.044
0.06	-0.004	0.052	0.087	0.048	0.059	0.031	0.016	-0.068
0.08	-0.011	0.066	0.120	0.066	0.079	0.042	0.025	-0.092
0.10	-0.019	0.080	0.153	0.083	0.096	0.054	0.035	-0.116
0.12	-0.028	0.094	0.188	0.101	0.112	0.067	0.045	-0.143
0.14	-0.037	0.107	0.223	0.120	0.128	0.080	0.054	-0.168
0.16	-0.043	0.120	0.257	0.137	0.143	0.094	0.061	-0.195
0.18	-0.047	0.131	0.284	0.155	0.155	0.107	0.068	-0.223
0.20	-0.049	0.141	0.307	0.175	0.168	0.120	0.074	-0.251
0.22	-0.049	0.150	0.337	0.195	0.180	0.133	0.079	-0.278
0.24	-0.048	0.157	0.371	0.216	0.191	0.144	0.084	-0.301
0.26	-0.046	0.163	0.406	0.238	0.202	0.157	0.089	-0.322
0.28	-0.043	0.168	0.445	0.261	0.213	0.168	0.094	-0.339
0.30	-0.039	0.171	0.474	0.284	0.224	0.180	0.100	-0.354
0.32	-0.035	0.173	0.502	0.306	0.235	0.192	0.105	-0.366
0.34	-0.031	0.173	0.531	0.329	0.247	0.203	0.111	-0.371
0.36	-0.028	0.173	0.558	0.352	0.262	0.216	0.117	-0.370
0.38	-0.025	0.171	0.577	0.374	0.277	0.228	0.124	-0.364
0.40	...	0.170	0.593	0.396	0.291	0.240	0.131	-0.353
0.42	...	0.168	0.608	0.419	0.304	0.252	0.138	-0.339
0.44	...	0.166	0.623	0.441	0.318	0.265	0.146	-0.324
0.46	...	0.165	0.640	0.465	0.333	0.277	0.155	-0.310
0.48	...	0.163	0.658	0.488	0.345	0.290	0.163	-0.296
0.50	...	0.162	0.674	0.513	0.357	0.303	0.172	-0.284
0.54	...	0.160	0.704	0.561	0.380	0.330	0.187	-0.267
0.58	...	0.160	0.732	0.608	0.405	0.357	0.200	-0.255
0.62	...	0.160	0.752	0.654	0.440	0.381	0.215	-0.250
0.66	...	0.160	0.771	0.697	0.477	0.403	0.230	-0.249
0.70	...	0.161	0.789	0.740	0.505	0.423	0.245	-0.250
0.80	...	...	0.828	0.845	0.579	0.474	0.288	-0.250
0.90	...	...	0.846	0.920	0.672	0.526	0.338	-0.215
1.00	...	...	0.863	0.974	0.778	0.571	0.397	-0.169
1.10	...	...	0.870	1.024	0.870	0.619	0.450	-0.140
1.20	...	...	0.872	1.066	0.953	0.672	0.494	-0.121
1.30	...	...	0.872	1.099	1.032	0.725	0.534	-0.108
1.40	...	...	0.857	1.122	1.105	0.778	0.569	-0.096
1.50	...	...	0.845	1.137	1.167	0.837	0.599	-0.055
1.60	...	...	0.841	1.146	1.219	0.898	0.627	0.006
1.70	...	...	0.841	1.151	1.254	0.955	0.658	0.049
1.80	...	...	...	1.155	1.288	1.010	0.687	0.089
1.90	...	...	...	1.156	1.312	1.065	0.717	0.121
2.00	...	...	...	1.157	1.334	1.123	0.748	0.155
2.20	...	...	...	1.153	1.373	1.234	0.821	0.214
2.40	...	...	...	1.140	1.417	1.328	0.902	0.266
2.60	...	...	...	...	1.426	1.416	0.970	0.302
2.80	...	...	...	...	1.419	1.481	1.062	0.328
3.00	...	...	...	...	1.399	1.527	1.165	0.367
3.20	...	...	...	...	1.389	1.567	1.245	0.441
3.40	...	...	...	...	1.389	1.596	1.343	0.500
3.60	...	...	...	...	1.399	1.615	1.438	0.529
3.80	...	...	...	...	1.401	1.629	1.509	0.565
4.00	...	...	...	...	1.402	1.637	1.559	0.669

Table A-24: Colors for UBG 05101

z	$(UV-U)$	$(U-B)$	$(B-V)$	$(V-I)$	$(I-J)$	$(J-H)$	$(H-K)$
0.02	0.193	0.686	0.298	0.260	0.161	0.170	-0.297
0.04	0.175	0.673	0.311	0.257	0.171	0.175	-0.270
0.06	0.155	0.660	0.324	0.253	0.180	0.178	-0.239
0.08	0.134	0.642	0.339	0.250	0.189	0.181	-0.206
0.10	0.111	0.622	0.356	0.251	0.194	0.182	-0.171
0.12	0.088	0.601	0.372	0.253	0.197	0.185	-0.134
0.14	0.067	0.579	0.389	0.255	0.200	0.190	-0.100
0.16	0.048	0.558	0.405	0.258	0.201	0.196	-0.066
0.18	0.032	0.543	0.414	0.263	0.200	0.203	-0.031
0.20	0.020	0.530	0.418	0.270	0.200	0.210	0.003
0.22	0.011	0.509	0.428	0.278	0.200	0.217	0.035
0.24	0.004	0.482	0.440	0.289	0.198	0.224	0.063
0.26	0.001	0.452	0.454	0.299	0.197	0.231	0.089
0.28	-0.001	0.419	0.469	0.311	0.196	0.238	0.112
0.30	0.000	0.392	0.476	0.323	0.196	0.244	0.132
0.32	0.002	0.366	0.482	0.334	0.195	0.250	0.149
0.34	0.005	0.338	0.488	0.345	0.196	0.256	0.161
0.36	0.009	0.311	0.491	0.354	0.198	0.262	0.166
0.38	0.013	0.290	0.489	0.360	0.201	0.267	0.167
0.40	-2.272	0.272	0.484	0.368	0.203	0.272	0.164
0.42	...	0.255	0.476	0.377	0.204	0.277	0.157
0.44	...	0.238	0.469	0.386	0.205	0.282	0.150
0.46	...	0.219	0.462	0.395	0.207	0.286	0.144
0.48	...	0.200	0.456	0.406	0.207	0.290	0.139
0.50	...	0.183	0.447	0.419	0.206	0.295	0.135
0.54	...	0.152	0.429	0.444	0.202	0.307	0.133
0.58	...	0.123	0.410	0.466	0.201	0.320	0.135
0.62	...	0.103	0.385	0.478	0.211	0.330	0.144
0.66	...	0.084	0.361	0.483	0.227	0.337	0.157
0.70	...	0.067	0.335	0.498	0.234	0.342	0.174
0.80	...	-1.081	0.269	0.529	0.257	0.349	0.216
0.90	...	...	0.213	0.512	0.298	0.352	0.232
1.00	...	...	0.175	0.460	0.359	0.338	0.244
1.10	...	...	0.132	0.418	0.403	0.333	0.269
1.20	...	...	0.092	0.377	0.433	0.341	0.295
1.30	...	...	0.060	0.331	0.459	0.354	0.321
1.40	...	...	0.022	0.281	0.479	0.373	0.344
1.50	...	...	-0.006	0.234	0.482	0.401	0.333
1.60	...	...	-0.019	0.191	0.473	0.435	0.300
1.70	...	...	-0.024	0.161	0.452	0.461	0.288
1.80	...	...	...	0.131	0.430	0.486	0.277
1.90	...	...	...	0.108	0.400	0.511	0.276
2.00	...	...	...	0.087	0.364	0.538	0.273
2.20	...	...	...	0.044	0.292	0.576	0.286
2.40	...	...	...	-0.014	0.242	0.590	0.315
2.60	...	...	...	0.892	0.162	0.610	0.347
2.80	...	...	...	...	0.091	0.583	0.413
3.00	...	...	...	...	0.025	0.526	0.477
3.20	...	...	...	...	-0.026	0.486	0.483
3.40	...	...	...	...	-0.055	0.417	0.522
3.60	...	...	...	...	-0.064	0.342	0.588
3.80	...	...	...	...	-0.076	0.284	0.623
4.00	...	...	...	...	-0.083	0.242	0.569

Table A-25: K-corrections for IRAS 05189-2524

z	$K(UV_{218})$	$K(U_{300})$	$K(B_{450})$	$K(V_{606})$	$K(I_{814})$	$K(J_{110})$	$K(H_{160})$	$K(K_{222})$
0.02	0.003	0.043	0.043	0.022	0.023	0.011	0.004	-0.020
0.04	0.002	0.082	0.089	0.046	0.045	0.023	0.011	-0.040
0.06	-0.003	0.118	0.136	0.070	0.068	0.035	0.019	-0.062
0.08	-0.012	0.151	0.186	0.095	0.092	0.048	0.029	-0.084
0.10	-0.023	0.183	0.240	0.120	0.112	0.061	0.041	-0.107
0.12	-0.035	0.212	0.294	0.148	0.132	0.076	0.052	-0.132
0.14	-0.047	0.240	0.350	0.175	0.152	0.091	0.061	-0.157
0.16	-0.057	0.266	0.404	0.202	0.170	0.106	0.070	-0.182
0.18	-0.065	0.289	0.450	0.229	0.187	0.121	0.077	-0.209
0.20	-0.071	0.309	0.489	0.259	0.204	0.136	0.084	-0.236
0.22	-0.075	0.326	0.536	0.290	0.219	0.150	0.090	-0.262
0.24	-0.077	0.341	0.591	0.323	0.234	0.164	0.096	-0.284
0.26	-0.078	0.354	0.648	0.356	0.250	0.177	0.102	-0.304
0.28	-0.078	0.364	0.710	0.389	0.265	0.191	0.108	-0.320
0.30	-0.077	0.372	0.756	0.424	0.281	0.205	0.115	-0.334
0.32	-0.075	0.377	0.802	0.457	0.297	0.218	0.121	-0.345
0.34	-0.074	0.381	0.848	0.492	0.314	0.232	0.128	-0.349
0.36	-0.074	0.382	0.896	0.528	0.334	0.246	0.135	-0.348
0.38	-0.073	0.382	0.934	0.562	0.355	0.260	0.143	-0.340
0.40	...	0.381	0.970	0.597	0.375	0.275	0.151	-0.329
0.42	...	0.379	1.003	0.633	0.394	0.289	0.159	-0.314
0.44	...	0.377	1.036	0.668	0.413	0.304	0.168	-0.298
0.46	...	0.374	1.071	0.706	0.433	0.319	0.178	-0.283
0.48	...	0.371	1.107	0.743	0.452	0.334	0.187	-0.269
0.50	...	0.368	1.139	0.783	0.470	0.349	0.197	-0.255
0.54	...	0.363	1.200	0.861	0.506	0.382	0.214	-0.237
0.58	...	0.359	1.261	0.937	0.546	0.414	0.229	-0.224
0.62	...	0.356	1.307	1.012	0.596	0.444	0.245	-0.218
0.66	...	0.353	1.351	1.083	0.652	0.472	0.262	-0.215
0.70	...	0.349	1.391	1.155	0.698	0.498	0.280	-0.215
0.80	...	...	1.477	1.336	0.821	0.566	0.328	-0.211
0.90	...	...	1.520	1.479	0.963	0.637	0.384	-0.173
1.00	...	...	1.557	1.597	1.120	0.702	0.450	-0.123
1.10	...	...	1.569	1.704	1.269	0.773	0.511	-0.090
1.20	...	...	1.569	1.794	1.407	0.849	0.564	-0.068
1.30	...	...	1.566	1.864	1.542	0.927	0.613	-0.052
1.40	...	...	1.545	1.918	1.670	1.009	0.657	-0.037
1.50	...	...	1.526	1.955	1.784	1.096	0.697	0.008
1.60	...	...	1.514	1.977	1.889	1.190	0.736	0.074
1.70	...	...	1.505	1.991	1.969	1.278	0.779	0.122
1.80	...	...	...	1.997	2.047	1.367	0.822	0.168
1.90	...	...	...	1.998	2.108	1.460	0.866	0.205
2.00	...	...	...	1.997	2.162	1.555	0.912	0.245
2.20	...	...	...	1.985	2.245	1.744	1.020	0.317
2.40	...	...	...	1.960	2.317	1.912	1.142	0.382
2.60	...	...	...	...	2.339	2.072	1.256	0.434
2.80	...	...	...	...	2.336	2.200	1.399	0.475
3.00	...	...	...	...	2.309	2.303	1.557	0.536
3.20	...	...	...	...	2.289	2.390	1.690	0.635
3.40	...	...	...	...	2.280	2.457	1.845	0.717
3.60	...	...	...	...	2.285	2.504	1.995	0.768
3.80	...	...	...	...	2.279	2.539	2.120	0.837
4.00	...	...	...	...	2.270	2.559	2.224	0.986

Table A-26: Colors for IRAS 05189-2524

z	$(UV-U)$	$(U-B)$	$(B-V)$	$(V-I)$	$(I-J)$	$(J-H)$	$(H-K)$
0.02	0.390	1.177	0.453	0.331	0.195	0.193	-0.274
0.04	0.350	1.170	0.476	0.332	0.207	0.198	-0.248
0.06	0.309	1.160	0.499	0.332	0.217	0.202	-0.218
0.08	0.267	1.143	0.524	0.334	0.228	0.205	-0.185
0.10	0.225	1.121	0.552	0.339	0.235	0.207	-0.151
0.12	0.183	1.097	0.579	0.347	0.240	0.210	-0.115
0.14	0.143	1.069	0.607	0.354	0.245	0.216	-0.081
0.16	0.107	1.040	0.635	0.362	0.249	0.222	-0.047
0.18	0.077	1.017	0.653	0.373	0.250	0.230	-0.012
0.20	0.050	0.998	0.663	0.386	0.252	0.238	0.022
0.22	0.028	0.968	0.679	0.401	0.254	0.246	0.054
0.24	0.011	0.929	0.701	0.418	0.255	0.253	0.082
0.26	-0.003	0.885	0.725	0.436	0.257	0.261	0.108
0.28	-0.013	0.834	0.753	0.454	0.258	0.269	0.130
0.30	-0.020	0.795	0.766	0.473	0.260	0.276	0.151
0.32	-0.025	0.755	0.778	0.491	0.263	0.283	0.168
0.34	-0.027	0.712	0.790	0.508	0.266	0.290	0.179
0.36	-0.028	0.666	0.801	0.524	0.272	0.297	0.185
0.38	-0.027	0.627	0.806	0.537	0.279	0.303	0.186
0.40	-2.274	0.590	0.807	0.552	0.284	0.310	0.183
0.42	...	0.555	0.804	0.569	0.289	0.316	0.177
0.44	...	0.520	0.802	0.585	0.294	0.321	0.170
0.46	...	0.481	0.800	0.602	0.299	0.327	0.164
0.48	...	0.443	0.797	0.621	0.302	0.333	0.159
0.50	...	0.408	0.790	0.643	0.305	0.339	0.155
0.54	...	0.342	0.774	0.684	0.309	0.354	0.153
0.58	...	0.277	0.758	0.721	0.316	0.371	0.156
0.62	...	0.227	0.730	0.746	0.336	0.385	0.165
0.66	...	0.180	0.702	0.762	0.364	0.395	0.180
0.70	...	0.136	0.671	0.788	0.384	0.404	0.197
0.80	...	-1.080	0.576	0.846	0.439	0.424	0.242
0.90	...	...	0.475	0.847	0.510	0.439	0.260
1.00	...	...	0.394	0.809	0.602	0.438	0.275
1.10	...	...	0.299	0.767	0.680	0.448	0.304
1.20	...	...	0.210	0.719	0.742	0.471	0.335
1.30	...	...	0.136	0.654	0.799	0.500	0.367
1.40	...	...	0.061	0.580	0.845	0.538	0.396
1.50	...	...	0.005	0.503	0.872	0.585	0.392
1.60	...	...	-0.030	0.420	0.884	0.640	0.365
1.70	...	...	-0.052	0.353	0.875	0.685	0.360
1.80	...	...	...	0.282	0.864	0.731	0.357
1.90	...	...	...	0.221	0.833	0.780	0.363
2.00	...	...	...	0.166	0.792	0.829	0.370
2.20	...	...	...	0.071	0.686	0.911	0.405
2.40	...	...	...	-0.026	0.590	0.956	0.463
2.60	...	...	...	0.890	0.452	1.002	0.525
2.80	...	...	...	...	0.321	0.988	0.626
3.00	...	...	...	...	0.191	0.932	0.724
3.20	...	...	...	...	0.085	0.886	0.758
3.40	...	...	...	...	0.008	0.799	0.830
3.60	...	...	...	...	-0.034	0.696	0.929
3.80	...	...	...	...	-0.075	0.606	0.986
4.00	...	...	...	...	-0.104	0.521	0.941

Table A-27: K-corrections for IRAS 12112+0305

z	$K(UV_{218})$	$K(U_{300})$	$K(B_{450})$	$K(V_{606})$	$K(I_{814})$	$K(J_{110})$	$K(H_{160})$	$K(K_{222})$
0.02	-0.002	0.022	0.024	0.013	0.019	0.010	0.004	-0.021
0.04	-0.008	0.042	0.052	0.026	0.037	0.019	0.010	-0.041
0.06	-0.019	0.060	0.078	0.039	0.056	0.030	0.018	-0.062
0.08	-0.034	0.078	0.108	0.053	0.074	0.041	0.027	-0.085
0.10	-0.053	0.095	0.139	0.067	0.090	0.053	0.038	-0.108
0.12	-0.072	0.112	0.172	0.081	0.104	0.066	0.049	-0.133
0.14	-0.092	0.128	0.207	0.096	0.119	0.079	0.057	-0.157
0.16	-0.109	0.144	0.241	0.110	0.132	0.092	0.065	-0.183
0.18	-0.124	0.158	0.268	0.125	0.143	0.105	0.072	-0.210
0.20	-0.137	0.171	0.291	0.141	0.154	0.117	0.078	-0.237
0.22	-0.146	0.181	0.322	0.157	0.163	0.130	0.083	-0.262
0.24	-0.154	0.190	0.359	0.175	0.172	0.141	0.088	-0.284
0.26	-0.159	0.197	0.395	0.194	0.180	0.152	0.093	-0.303
0.28	-0.162	0.201	0.437	0.214	0.189	0.164	0.099	-0.319
0.30	-0.164	0.204	0.469	0.235	0.198	0.175	0.105	-0.332
0.32	-0.165	0.205	0.500	0.254	0.207	0.186	0.110	-0.343
0.34	-0.167	0.203	0.533	0.275	0.216	0.197	0.116	-0.348
0.36	-0.168	0.200	0.563	0.296	0.229	0.208	0.122	-0.346
0.38	-0.170	0.195	0.585	0.317	0.242	0.220	0.129	-0.339
0.40	...	0.188	0.601	0.336	0.253	0.231	0.136	-0.328
0.42	...	0.181	0.617	0.357	0.264	0.242	0.143	-0.314
0.44	...	0.173	0.632	0.379	0.275	0.254	0.151	-0.299
0.46	...	0.165	0.650	0.402	0.288	0.266	0.159	-0.284
0.48	...	0.157	0.669	0.424	0.299	0.278	0.167	-0.270
0.50	...	0.150	0.686	0.448	0.308	0.289	0.176	-0.257
0.54	...	0.135	0.719	0.495	0.326	0.315	0.190	-0.239
0.58	...	0.124	0.750	0.542	0.345	0.339	0.203	-0.228
0.62	...	0.114	0.775	0.589	0.373	0.361	0.217	-0.222
0.66	...	0.105	0.798	0.634	0.405	0.381	0.232	-0.221
0.70	...	0.096	0.820	0.680	0.426	0.398	0.247	-0.221
0.80	...	...	0.869	0.795	0.487	0.441	0.288	-0.221
0.90	...	...	0.895	0.877	0.573	0.486	0.337	-0.187
1.00	...	...	0.915	0.937	0.681	0.522	0.394	-0.139
1.10	...	...	0.915	0.993	0.776	0.562	0.446	-0.112
1.20	...	...	0.902	1.042	0.863	0.608	0.487	-0.095
1.30	...	...	0.883	1.082	0.947	0.654	0.523	-0.083
1.40	...	...	0.849	1.111	1.025	0.701	0.552	-0.072
1.50	...	...	0.817	1.130	1.091	0.754	0.578	-0.031
1.60	...	...	0.794	1.140	1.147	0.811	0.600	0.030
1.70	...	...	0.773	1.140	1.186	0.864	0.625	0.073
1.80	...	...	...	1.135	1.224	0.916	0.648	0.111
1.90	...	...	...	1.125	1.256	0.968	0.673	0.141
2.00	...	...	...	1.113	1.284	1.024	0.698	0.173
2.20	...	...	...	1.085	1.335	1.139	0.757	0.226
2.40	...	...	...	1.041	1.390	1.241	0.823	0.272
2.60	...	...	...	...	1.397	1.339	0.879	0.299
2.80	...	...	...	...	1.380	1.412	0.961	0.316
3.00	...	...	...	...	1.332	1.463	1.061	0.347
3.20	...	...	...	...	1.290	1.507	1.142	0.411
3.40	...	...	...	...	1.263	1.539	1.246	0.462
3.60	...	...	...	...	1.263	1.556	1.350	0.484
3.80	...	...	...	...	1.251	1.567	1.430	0.505
4.00	...	...	...	...	1.230	1.572	1.481	0.596

Table A-28: Colors for IRAS 12112+0305

z	$(UV-U)$	$(U-B)$	$(B-V)$	$(V-I)$	$(I-J)$	$(J-H)$	$(H-K)$
0.02	0.227	0.707	0.244	0.228	0.154	0.173	-0.274
0.04	0.201	0.700	0.258	0.223	0.163	0.177	-0.248
0.06	0.172	0.693	0.272	0.217	0.171	0.180	-0.218
0.08	0.139	0.681	0.287	0.212	0.179	0.181	-0.186
0.10	0.103	0.666	0.305	0.210	0.183	0.182	-0.152
0.12	0.067	0.650	0.323	0.211	0.185	0.184	-0.117
0.14	0.031	0.632	0.343	0.211	0.186	0.188	-0.084
0.16	-0.002	0.614	0.362	0.212	0.186	0.194	-0.051
0.18	-0.032	0.601	0.375	0.216	0.184	0.200	-0.017
0.20	-0.057	0.590	0.383	0.221	0.182	0.207	0.016
0.22	-0.077	0.570	0.397	0.228	0.180	0.214	0.047
0.24	-0.093	0.542	0.416	0.237	0.177	0.220	0.074
0.26	-0.106	0.513	0.433	0.247	0.174	0.226	0.099
0.28	-0.114	0.476	0.455	0.258	0.172	0.232	0.120
0.30	-0.118	0.447	0.467	0.270	0.169	0.237	0.139
0.32	-0.120	0.416	0.479	0.281	0.167	0.243	0.155
0.34	-0.120	0.382	0.491	0.291	0.166	0.248	0.166
0.36	-0.119	0.348	0.500	0.301	0.166	0.253	0.171
0.38	-0.115	0.321	0.501	0.308	0.168	0.258	0.171
0.40	-2.278	0.298	0.498	0.316	0.168	0.262	0.167
0.42	...	0.275	0.493	0.326	0.168	0.267	0.160
0.44	...	0.252	0.487	0.337	0.167	0.270	0.153
0.46	...	0.226	0.482	0.346	0.168	0.274	0.147
0.48	...	0.200	0.478	0.358	0.167	0.277	0.141
0.50	...	0.175	0.472	0.373	0.165	0.281	0.136
0.54	...	0.127	0.457	0.402	0.157	0.292	0.133
0.58	...	0.084	0.442	0.430	0.152	0.303	0.134
0.62	...	0.050	0.419	0.450	0.157	0.311	0.142
0.66	...	0.018	0.397	0.462	0.170	0.316	0.155
0.70	...	-0.013	0.373	0.487	0.173	0.319	0.171
0.80	...	-1.087	0.308	0.541	0.192	0.320	0.212
0.90	...	...	0.251	0.539	0.232	0.317	0.227
1.00	...	...	0.211	0.490	0.305	0.295	0.236
1.10	...	...	0.156	0.450	0.359	0.284	0.260
1.20	...	...	0.094	0.413	0.401	0.288	0.284
1.30	...	...	0.035	0.369	0.438	0.299	0.308
1.40	...	...	-0.028	0.320	0.469	0.316	0.328
1.50	...	...	-0.080	0.273	0.483	0.343	0.312
1.60	...	...	-0.112	0.226	0.482	0.379	0.273
1.70	...	...	-0.133	0.188	0.468	0.406	0.256
1.80	...	...	...	0.145	0.454	0.435	0.240
1.90	...	...	...	0.103	0.434	0.462	0.235
2.00	...	...	...	0.063	0.406	0.493	0.228
2.20	...	...	...	-0.017	0.343	0.549	0.233
2.40	...	...	...	-0.115	0.295	0.585	0.254
2.60	...	...	...	0.885	0.204	0.628	0.282
2.80	...	...	...	...	0.115	0.619	0.347
3.00	...	...	...	...	0.015	0.570	0.417
3.20	...	...	...	...	-0.070	0.532	0.434
3.40	...	...	...	...	-0.130	0.460	0.487
3.60	...	...	...	...	-0.147	0.374	0.569
3.80	...	...	...	...	-0.171	0.305	0.628
4.00	...	...	...	...	-0.196	0.258	0.588

Table A-29: K-corrections for IRAS 14348-1447

z	$K(UV_{218})$	$K(U_{300})$	$K(B_{450})$	$K(V_{606})$	$K(I_{814})$	$K(J_{110})$	$K(H_{160})$	$K(K_{222})$
0.02	-0.002	0.017	0.018	0.008	0.016	0.008	0.003	-0.020
0.04	-0.007	0.032	0.039	0.016	0.032	0.016	0.007	-0.040
0.06	-0.016	0.046	0.059	0.024	0.048	0.025	0.014	-0.063
0.08	-0.029	0.059	0.082	0.033	0.064	0.035	0.022	-0.085
0.10	-0.043	0.072	0.108	0.041	0.077	0.045	0.031	-0.109
0.12	-0.059	0.085	0.135	0.051	0.088	0.056	0.040	-0.134
0.14	-0.074	0.097	0.163	0.060	0.099	0.067	0.047	-0.158
0.16	-0.087	0.109	0.192	0.068	0.109	0.079	0.054	-0.184
0.18	-0.097	0.120	0.214	0.077	0.117	0.090	0.059	-0.212
0.20	-0.105	0.130	0.234	0.087	0.124	0.101	0.063	-0.239
0.22	-0.111	0.138	0.262	0.098	0.130	0.111	0.067	-0.265
0.24	-0.115	0.144	0.295	0.110	0.136	0.121	0.071	-0.287
0.26	-0.117	0.149	0.327	0.123	0.141	0.131	0.075	-0.307
0.28	-0.118	0.152	0.365	0.137	0.146	0.140	0.079	-0.323
0.30	-0.118	0.154	0.395	0.153	0.151	0.150	0.083	-0.337
0.32	-0.118	0.154	0.426	0.167	0.157	0.159	0.087	-0.348
0.34	-0.117	0.152	0.458	0.183	0.163	0.168	0.092	-0.353
0.36	-0.117	0.149	0.487	0.200	0.171	0.178	0.097	-0.352
0.38	-0.117	0.145	0.507	0.216	0.180	0.187	0.103	-0.346
0.40	...	0.140	0.520	0.231	0.187	0.197	0.108	-0.336
0.42	...	0.134	0.531	0.248	0.194	0.206	0.114	-0.323
0.44	...	0.129	0.543	0.265	0.202	0.216	0.121	-0.308
0.46	...	0.123	0.557	0.284	0.211	0.226	0.128	-0.295
0.48	...	0.118	0.572	0.302	0.218	0.236	0.135	-0.283
0.50	...	0.112	0.586	0.322	0.223	0.245	0.142	-0.271
0.54	...	0.103	0.611	0.361	0.233	0.267	0.154	-0.256
0.58	...	0.095	0.636	0.401	0.244	0.286	0.165	-0.247
0.62	...	0.089	0.654	0.442	0.263	0.304	0.177	-0.243
0.66	...	0.083	0.671	0.482	0.286	0.318	0.189	-0.244
0.70	...	0.077	0.687	0.523	0.296	0.331	0.202	-0.246
0.80	...	...	0.724	0.627	0.334	0.362	0.239	-0.251
0.90	...	...	0.742	0.700	0.399	0.393	0.282	-0.221
1.00	...	...	0.756	0.747	0.497	0.415	0.333	-0.178
1.10	...	...	0.756	0.789	0.582	0.442	0.378	-0.154
1.20	...	...	0.748	0.828	0.660	0.475	0.412	-0.141
1.30	...	...	0.736	0.858	0.736	0.508	0.441	-0.134
1.40	...	...	0.708	0.879	0.805	0.542	0.462	-0.128
1.50	...	...	0.683	0.892	0.863	0.582	0.479	-0.090
1.60	...	...	0.667	0.898	0.909	0.628	0.493	-0.031
1.70	...	...	0.656	0.898	0.938	0.670	0.509	0.008
1.80	...	...	...	0.895	0.966	0.712	0.523	0.041
1.90	...	...	...	0.889	0.988	0.753	0.538	0.067
2.00	...	...	...	0.881	1.009	0.798	0.553	0.093
2.20	...	...	...	0.860	1.047	0.895	0.591	0.135
2.40	...	...	...	0.828	1.092	0.984	0.635	0.171
2.60	...	...	...	...	1.096	1.072	0.668	0.185
2.80	...	...	...	...	1.079	1.134	0.730	0.190
3.00	...	...	...	...	1.042	1.173	0.813	0.207
3.20	...	...	...	...	1.013	1.206	0.884	0.253
3.40	...	...	...	...	0.998	1.230	0.978	0.290
3.60	...	...	...	...	0.999	1.243	1.077	0.301
3.80	...	...	...	...	0.990	1.251	1.153	0.307
4.00	...	...	...	...	0.979	1.254	1.193	0.374

Table A-30: Colors for IRAS 14348-1447

z	$(UV-U)$	$(U-B)$	$(B-V)$	$(V-I)$	$(I-J)$	$(J-H)$	$(H-K)$
0.02	0.176	0.603	0.156	0.172	0.121	0.142	-0.283
0.04	0.155	0.597	0.169	0.164	0.129	0.146	-0.259
0.06	0.133	0.591	0.181	0.156	0.136	0.148	-0.230
0.08	0.107	0.581	0.196	0.149	0.143	0.150	-0.199
0.10	0.080	0.568	0.212	0.144	0.146	0.150	-0.167
0.12	0.051	0.554	0.230	0.143	0.146	0.152	-0.133
0.14	0.024	0.538	0.249	0.140	0.146	0.157	-0.101
0.16	-0.001	0.522	0.269	0.139	0.144	0.162	-0.069
0.18	-0.023	0.510	0.283	0.140	0.141	0.168	-0.037
0.20	-0.041	0.500	0.293	0.143	0.138	0.175	-0.005
0.22	-0.055	0.481	0.310	0.147	0.133	0.181	0.025
0.24	-0.066	0.454	0.331	0.154	0.129	0.187	0.051
0.26	-0.073	0.427	0.350	0.161	0.125	0.193	0.075
0.28	-0.077	0.393	0.374	0.170	0.120	0.198	0.095
0.30	-0.079	0.364	0.389	0.180	0.116	0.203	0.114
0.32	-0.078	0.333	0.405	0.190	0.112	0.208	0.129
0.34	-0.076	0.299	0.421	0.200	0.109	0.213	0.139
0.36	-0.073	0.267	0.433	0.208	0.107	0.218	0.143
0.38	-0.069	0.243	0.437	0.215	0.106	0.222	0.143
0.40	-2.276	0.224	0.436	0.223	0.104	0.225	0.139
0.42	...	0.207	0.431	0.233	0.102	0.229	0.132
0.44	...	0.190	0.425	0.243	0.099	0.232	0.124
0.46	...	0.171	0.420	0.252	0.099	0.235	0.118
0.48	...	0.151	0.417	0.263	0.096	0.238	0.112
0.50	...	0.131	0.411	0.278	0.092	0.240	0.108
0.54	...	0.096	0.397	0.307	0.080	0.249	0.105
0.58	...	0.064	0.381	0.336	0.072	0.259	0.106
0.62	...	0.040	0.358	0.359	0.073	0.264	0.114
0.66	...	0.016	0.336	0.376	0.081	0.267	0.127
0.70	...	-0.006	0.311	0.406	0.079	0.266	0.142
0.80	...	-1.085	0.244	0.472	0.086	0.260	0.184
0.90	...	...	0.189	0.482	0.119	0.248	0.197
1.00	...	...	0.156	0.430	0.195	0.219	0.206
1.10	...	...	0.114	0.388	0.254	0.201	0.227
1.20	...	...	0.068	0.347	0.299	0.199	0.248
1.30	...	...	0.025	0.302	0.341	0.205	0.269
1.40	...	...	-0.023	0.255	0.376	0.217	0.285
1.50	...	...	-0.062	0.209	0.394	0.240	0.265
1.60	...	...	-0.084	0.169	0.395	0.271	0.219
1.70	...	...	-0.095	0.140	0.382	0.298	0.197
1.80	...	...	...	0.109	0.369	0.326	0.177
1.90	...	...	...	0.080	0.350	0.351	0.167
2.00	...	...	...	0.053	0.324	0.382	0.155
2.20	...	...	...	-0.007	0.267	0.440	0.151
2.40	...	...	...	-0.084	0.222	0.486	0.159
2.60	...	...	...	0.888	0.138	0.540	0.178
2.80	...	...	...	...	0.059	0.542	0.234
3.00	...	...	...	...	-0.017	0.496	0.301
3.20	...	...	...	...	-0.079	0.460	0.325
3.40	...	...	...	...	-0.118	0.390	0.382
3.60	...	...	...	...	-0.130	0.303	0.470
3.80	...	...	...	...	-0.146	0.235	0.541
4.00	...	...	...	...	-0.160	0.198	0.514

Table A-31: K-corrections for IRAS 15250+3609

z	$K(UV_{218})$	$K(U_{300})$	$K(B_{450})$	$K(V_{606})$	$K(I_{814})$	$K(J_{110})$	$K(H_{160})$	$K(K_{222})$
0.02	-0.002	0.019	0.021	0.010	0.017	0.008	0.003	-0.020
0.04	-0.006	0.035	0.044	0.020	0.034	0.017	0.008	-0.040
0.06	-0.015	0.050	0.067	0.030	0.051	0.027	0.015	-0.062
0.08	-0.028	0.065	0.093	0.041	0.068	0.037	0.023	-0.085
0.10	-0.042	0.079	0.121	0.052	0.082	0.047	0.033	-0.108
0.12	-0.058	0.093	0.151	0.063	0.095	0.059	0.042	-0.133
0.14	-0.072	0.106	0.182	0.075	0.107	0.071	0.050	-0.158
0.16	-0.085	0.119	0.213	0.085	0.118	0.083	0.056	-0.184
0.18	-0.095	0.131	0.237	0.097	0.127	0.095	0.062	-0.211
0.20	-0.103	0.141	0.259	0.109	0.136	0.106	0.067	-0.238
0.22	-0.109	0.150	0.289	0.122	0.144	0.117	0.071	-0.264
0.24	-0.113	0.157	0.323	0.137	0.150	0.128	0.075	-0.286
0.26	-0.115	0.162	0.358	0.152	0.157	0.138	0.079	-0.306
0.28	-0.116	0.165	0.397	0.168	0.164	0.148	0.084	-0.322
0.30	-0.116	0.167	0.429	0.186	0.170	0.158	0.089	-0.336
0.32	-0.116	0.167	0.461	0.202	0.177	0.168	0.093	-0.347
0.34	-0.115	0.166	0.494	0.220	0.185	0.178	0.098	-0.352
0.36	-0.115	0.163	0.525	0.239	0.195	0.188	0.103	-0.351
0.38	-0.115	0.159	0.546	0.257	0.205	0.199	0.109	-0.345
0.40	...	0.154	0.561	0.274	0.214	0.209	0.115	-0.335
0.42	...	0.149	0.574	0.293	0.223	0.219	0.122	-0.321
0.44	...	0.143	0.587	0.312	0.231	0.230	0.129	-0.307
0.46	...	0.138	0.602	0.332	0.242	0.240	0.136	-0.293
0.48	...	0.133	0.618	0.352	0.250	0.251	0.144	-0.280
0.50	...	0.128	0.633	0.374	0.257	0.261	0.151	-0.269
0.54	...	0.118	0.662	0.417	0.271	0.284	0.164	-0.253
0.58	...	0.111	0.688	0.460	0.285	0.306	0.175	-0.243
0.62	...	0.105	0.708	0.504	0.308	0.325	0.188	-0.239
0.66	...	0.099	0.727	0.547	0.334	0.342	0.201	-0.239
0.70	...	0.093	0.744	0.590	0.349	0.357	0.215	-0.241
0.80	...	...	0.784	0.700	0.396	0.392	0.253	-0.244
0.90	...	...	0.804	0.779	0.468	0.429	0.298	-0.213
1.00	...	...	0.819	0.830	0.572	0.457	0.352	-0.169
1.10	...	...	0.820	0.877	0.663	0.489	0.399	-0.144
1.20	...	...	0.812	0.918	0.746	0.527	0.436	-0.129
1.30	...	...	0.801	0.951	0.827	0.566	0.468	-0.121
1.40	...	...	0.773	0.974	0.900	0.605	0.493	-0.113
1.50	...	...	0.748	0.988	0.962	0.651	0.513	-0.074
1.60	...	...	0.733	0.995	1.013	0.701	0.530	-0.014
1.70	...	...	0.721	0.996	1.045	0.748	0.550	0.026
1.80	...	...	...	0.993	1.076	0.794	0.568	0.061
1.90	...	...	...	0.988	1.101	0.840	0.587	0.089
2.00	...	...	...	0.981	1.123	0.890	0.606	0.117
2.20	...	...	...	0.960	1.165	0.995	0.653	0.164
2.40	...	...	...	0.928	1.211	1.090	0.706	0.204
2.60	...	...	...	...	1.215	1.183	0.748	0.223
2.80	...	...	...	...	1.199	1.250	0.817	0.233
3.00	...	...	...	...	1.163	1.293	0.908	0.256
3.20	...	...	...	...	1.135	1.330	0.984	0.309
3.40	...	...	...	...	1.120	1.356	1.083	0.351
3.60	...	...	...	...	1.121	1.371	1.186	0.367
3.80	...	...	...	...	1.113	1.380	1.267	0.380
4.00	...	...	...	...	1.102	1.384	1.311	0.456

Table A-32: Colors for IRAS 15250+3609

z	$(UV-U)$	$(U-B)$	$(B-V)$	$(V-I)$	$(I-J)$	$(J-H)$	$(H-K)$
0.02	0.188	0.651	0.192	0.195	0.133	0.150	-0.282
0.04	0.167	0.644	0.205	0.188	0.141	0.154	-0.257
0.06	0.143	0.637	0.218	0.181	0.149	0.157	-0.228
0.08	0.116	0.625	0.233	0.175	0.156	0.159	-0.197
0.10	0.088	0.611	0.250	0.171	0.160	0.160	-0.164
0.12	0.059	0.595	0.268	0.170	0.161	0.162	-0.130
0.14	0.030	0.578	0.288	0.169	0.161	0.166	-0.098
0.16	0.005	0.560	0.308	0.169	0.160	0.172	-0.065
0.18	-0.017	0.547	0.321	0.171	0.157	0.178	-0.033
0.20	-0.036	0.535	0.331	0.175	0.155	0.185	-0.001
0.22	-0.050	0.515	0.347	0.180	0.151	0.191	0.030
0.24	-0.061	0.487	0.367	0.187	0.148	0.198	0.056
0.26	-0.069	0.458	0.387	0.196	0.144	0.204	0.080
0.28	-0.074	0.422	0.410	0.205	0.141	0.210	0.101
0.30	-0.076	0.392	0.424	0.216	0.137	0.215	0.120
0.32	-0.075	0.361	0.439	0.227	0.134	0.220	0.135
0.34	-0.074	0.326	0.455	0.237	0.132	0.225	0.146
0.36	-0.071	0.293	0.466	0.246	0.131	0.230	0.150
0.38	-0.067	0.267	0.470	0.253	0.131	0.235	0.150
0.40	-2.276	0.247	0.468	0.261	0.130	0.239	0.146
0.42	...	0.229	0.463	0.271	0.128	0.243	0.139
0.44	...	0.210	0.457	0.281	0.127	0.246	0.132
0.46	...	0.190	0.452	0.291	0.127	0.249	0.126
0.48	...	0.168	0.448	0.303	0.125	0.252	0.120
0.50	...	0.148	0.441	0.318	0.121	0.256	0.116
0.54	...	0.111	0.426	0.347	0.111	0.266	0.113
0.58	...	0.077	0.409	0.376	0.104	0.276	0.114
0.62	...	0.050	0.386	0.398	0.107	0.282	0.123
0.66	...	0.026	0.362	0.414	0.117	0.286	0.136
0.70	...	0.002	0.336	0.442	0.117	0.287	0.151
0.80	...	-1.085	0.266	0.506	0.129	0.284	0.193
0.90	...	...	0.207	0.512	0.164	0.276	0.207
1.00	...	...	0.170	0.460	0.240	0.250	0.217
1.10	...	...	0.125	0.416	0.299	0.235	0.239
1.20	...	...	0.076	0.374	0.344	0.236	0.262
1.30	...	...	0.032	0.327	0.385	0.244	0.284
1.40	...	...	-0.019	0.276	0.420	0.258	0.301
1.50	...	...	-0.058	0.228	0.437	0.283	0.284
1.60	...	...	-0.081	0.185	0.436	0.316	0.241
1.70	...	...	-0.093	0.153	0.422	0.343	0.220
1.80	...	...	...	0.119	0.407	0.372	0.202
1.90	...	...	...	0.088	0.386	0.398	0.194
2.00	...	...	...	0.059	0.358	0.429	0.185
2.20	...	...	...	-0.003	0.295	0.487	0.185
2.40	...	...	...	-0.081	0.246	0.530	0.198
2.60	...	...	...	0.888	0.158	0.581	0.220
2.80	...	...	...	...	0.074	0.579	0.279
3.00	...	...	...	...	-0.005	0.530	0.348
3.20	...	...	...	...	-0.069	0.491	0.371
3.40	...	...	...	...	-0.111	0.418	0.428
3.60	...	...	...	...	-0.124	0.330	0.515
3.80	...	...	...	...	-0.143	0.259	0.583
4.00	...	...	...	...	-0.157	0.218	0.551

REFERENCES

Abraham, R. G., Ellis, R. S., Fabian, A. C., Tanvir, N. R., & Glazebrook, K. 1999, MNRAS, 303, 641

Abraham, R. G., Tanvir, N. R., Santiago, B. X., Ellis, R. S., Glazebrook, K., & Van Den Bergh, S. 1996, MNRAS, 279, 47

Adelberger, K. L., Steidel, C. C., Giavalisco, M., Dickinson, M., Pettini, M., & Kellogg, M. 1998, ApJ, 505, 18

Aguerri, J. A. L. & Trujillo, I. 2002, MNRAS 333, 633

Aragón-Salamanca, A., Ellis, R. S., Couch, W.J., & Carter, D. 1993, MNRAS, 262, 764

Arnouts, S., Cristiani, S., Moscardini, L., Matarrese, S., Lucchin, F., Fontana, A., & Giallongo, E. 1999, MNRAS, 310, 540

Bardeen, J. M., Bond, J. R., Kaiser, N., & Szalay, A. S. 1986, ApJ, 304, 15

Barnes, J. & Hernquist, L. 1996, ApJ, 471, 115

Barnes, J. E. 1992, ApJ, 393, 484

Baugh, C. M., Cole, S., Frenk, C. S., & Lacey, C. G. 1998, ApJ, 498, 504

Bender, R., Burnstein, D., & Faber, S. M. 1992, ApJ, 399, 462

Budavári, T., Szalay, A. S., Connolly, A. J., Csabai, I., & Dickinson, M. 2000, AJ, 120, 1588

Bullock, J. S., Wechsler, R. H., & Somerville, R. S. 2002, MNRAS, 329, 246

Byun, Y. I., Freeman, K. C., & Kylafis, N. D. 1994, ApJ, 432, 114

Casertano, S., de Mello, D., Dickinson, M., Ferguson, H.C., Fruchter, A. S., Gonzalez-Lopezlira, R. A., Heyer, I., Hook, R. N., Levay, Z., Lucas, R. A., Mack, J., Makidon, R. B., Mutchler, M., Smith, T. E., Stiavelli, M., Wiggs, M. S., & Williams, R. E. 2000, AJ, 120, 2747

Chen, H., Fernandez-Soto, A., Lanzetta, K. M., Pascarelle, S. M., Puetter, R.C., Yahat, N., & Yahil, A. 1998, Astro-Physics/9812339

Code, A. D., & Welch, G. A. 1979, ApJ, 228, 95

Cohen, J. G., Cowie, L. L., Hogg, D. W., Songaila, A., Blandford, R., Hu, E. M., & Shopbell, P. 1996, ApJ, 471, L5

Cole, S., Aragon-Salamanca, A., Frenk, C. S., Navarro, J. F., & Zepf, S. E. 1994 MNRAS, 271, 781

Connolly, A. J., Szalay, A. S., Brunner, R.J. 1998, ApJ, 499, 125

Conselice, C. J., Bershady M. A., & Gallagher, J. S., III 2000 A&A, 354, 21

Corbin, M. R., Urban, A., Stobie, E., Thompson, R. I., Schneider, & Glenn 2001, ApJ, 551, 23

de Boer, K. S. 1982, A&AS, 50, 247

de Jong, R. S. 1996, A&A, 313, 377

de Vaucouleurs, G. 1948, AnAp, 11, 247

Devriendt, J. E. G., Guiderdoni, B., & Sadat, R. 1999 A&A, 350, 381

Dickinson, M. 1998, in STScI Symp. Ser. 11, The Hubble Deep Field, ed. M. Livio, S. M. Fall, & P. Madau (New York: Cambridge University Press), 219

Dickinson, M. 1998, "A Complete NICMOS Map of the Hubble Deep Field", The Space Telescope Science Institute, Retrieved May, 2003 from http://nemesis.stsci.edu/∼med/hdfNIC7817

Dickinson, M. 1999, in After the Dark Ages: When Galaxies were Young, eds. S. Holt & E. Smith, (New York: AIP), 122

Dickinson, M., Hanley, C., Elston, R., Eisenhardt, P. R., Stanford, S. A., Adelberger, K. L., Shapley, A., Steidel, C.C., Papovich, C., Szalay, A. S., Bershady, M. A., Conselice, C. J., Ferguson, H. C., & Fruchter, A. S. 2000, ApJ, 531, 624

Eggen, O.J., Lynden-Bell, D., & Sandage, A. R. 1962, ApJ, 136, 748

Ellis, R. S., Smail, I., Dressler, A., Couch, W.J., Oemler, A. Jr., Harvey, B., & Sharples, R. M. 1997, ApJ, 483, 582

Evans, R. 1994, MNRAS, 266, 511

Franx, M., Illingworth, G., & Heckman, T. 1989, AJ, 98, 538

Freeman, K. C. 1970 ApJ, 160, 811

Fruchter, A. S. & Hook, R. N. 1998, PASP, 792, 144

Giavalisco, M. 2002, ARA&A, 40, 579

Giavalisco, M. & Dickinson. M. 2001, ApJ, 550, 177

Giavalisco, M., Steidel, C. C., Adelberger, K. L., Dickinson, M.E., Pettini, M., & Kellogg, M. 1998, ApJ, 503, 543

Giavalisco, M., Steidel, C. C., & Macchetto, F. D. 1996, ApJ, 470, 189

Giavalisco, M., Steidel. C. C., & Szalay, A. S. 1994, ApJ, 425, 5

Guzmán, R., Jangren, A., Koo, D. C., Bershady, M., & Simard, L. 1998, ApJ, 495, L13

Gwynn, S. D. J. & Hartwick, F. D. A. 1996, Astro-Physics/9603149

Heckman, T. M., Armus, L., & Miley, G. K. 1990, ApJs, 74, 833

Hernquist, L. & Mihos, J. 1995, ApJ, 448, 41

Hogg, D. W., Neugebauer, G., Armus, L., Matthews, K., Pahre, M. A., Soifer, B. T., & Weinberger, A. J. 1997, AJ, 113, 2338

Jedrzejewski, R. I. 1987, MNRAS, 226, 747

Kaiser, N. 1984, ApJ, 344, 685

Kauffmann, G., Nusser, A., & Steinmetz, M. 1997, MNRAS, 286, 795

Kobulnicki, H. A. & Koo, D. C. 2000, AJ, 119, 1608

Koo, D. C., Bershady, M. A., Wirth, G. D., Stanford, S. A., & Majewski, S. R. 1994, ApJ, 427, L9

Koo, D. C., Guzmán, R., Faber, S. M., Illingworth G. D., Bershady, M. A., Kron, R. G., & Takamiya, M. 1995 ApJ, 440, L49

Lehnert, M. D., & Heckmann, T. M. 1996, ApJ, 472, 546

Lowenthal, J. D., Koo, D. C., Guzmán, R., Gallego, J., Phillips, A. C., Faber, S. M., Vogt, N.P., Illingworth, G. D., & Gronwall, C. 1997, ApJ, 481, 673

Madau, P., Ferguson, H. C., Dickinson, M. E., Giavalisco, M., Steidel, C.C., & Fruchter, A. 1996, MNRAS, 283, 1388

Marleau, F. R. & Simard, L. 1998, ApJ, 507, 585

Menanteau, F., Abraham, R.G., & Ellis, R. S. 2001, MNRAS, 322, 1

Meurer, G., Heckman, T., & Calzetti, D. 1999, ApJ, 521, 64

Meurer, G., Heckman, T., Lehnert, M., Leitherer, C., & Lowenthal, J. 1997, AJ, 114, 54

Mihos, J. & Hernquist, L. 1994a, ApJ, 425, 13

Mihos, J. & Hernquist, L. 1994b, ApJ, 427, 112

Mihos, J. & Hernquist, L. 1995, ApJ, 438, L75

Mihos, J. & Hernquist, L. 1996, ApJ, 464, 641

Mihos, C. J., Richstone, D. O., & Bothun, G. 1992, ApJ, 400, 153

Moorwood, A. F. M., vad der Werf, P. P., Cuby, J. G., & Olivia, E. 2000, A&A, 362, 9

Moustakas, L. A. & Somerville, R. S. 2002, ApJ, in press, Astro-Physics/0110584

Negroponte, J. & White, S. D. M. 1983, MNRAS, 205, 1009

O'Connell, R. W., Bohlin, R. C., Collins, N. R., Cornett, R. H., Hill, J. K., Hill, R. S., Landsman, W. B., Roberts, M. S., Smith, A. M., & Stecher, T. P. 1992, ApJ, 395, L45

Ohl, R. G., O'Connell, R. W., Bohlin, R. C., Collins, N. R., Dorman, B., Fanelli, M.N., Neff, S. G., Roberts, M. S., Smith, A. M., & Stecher, T. P. 1998, ApJ, 505, L11

Oke, J. B., & Gunn, J. 1983, ApJ, 266, 713

Oke, J. B. & Sandage, A. 1968, ApJ, 154, 210

Papovich, C., Dickinson, M., & Ferguson, H. C. 2001, ApJ, 559, 620

Peebles, P. J. E. 1970, AJ, 75, 13

Peletier, R. F., Valentijn, E. A., & Jameson, R. F. 1990, A&A, 233, 62

Pettini, M., Kellogg, M., Steidel, C. C., Dickinson, M., Adelberger, K. L., & Giavalisco, M. 1998, ApJ, 508, 539

Pettini, M., Shapley, A. E., Steidel, C.C., Cuby, J., Dickinson, M., Moorwood, A. F. M., Adelberger,K. L., & Giavalisco, M. 2001, ApJ, 554: 981

Pettini, M., Steidel, C. C., Adelberger, K. L., Dickinson, M., & Giavalisco, M. 2000, ApJ, 528, 96

Porciani, C. & Giavalisco, M. 2002, ApJ, 565, 24

Roukema, B. F., Quinn, P. J., Peterson B. A., & Rocca-Volmerange, B. 1997, MNRAS, 292, 835

Sawicki, M. & Yee, H. 1998, AJ, 115, 1329

Sérsic, J. L. 1968, Atlas de Galaxias Australes (Cordoba: Observatorio Astronomica)

Shapley, A. E., Steidel, C. C., Adelberger, K. L., Dickinson, M., Giavalisco, M., & Pettini, M. 2001, ApJ, 562, 95

Shlosman, I., Begelman, M. C., & Frank, J. 1990, Nature, 345, 679

Silva, D. R. & Elston, R. 1994, ApJ, 428, 511

Somerville, R., Primack, J. R., & Faber, S. M. 2001, MNRAS, 320, 504

Stanford, S. A., Eisenahrdt, P. R. , & Dickinson, M. 1998, ApJ, 492, 461

Stanford, S. A., Eisenhardt, P. R. M., & Dickinson, M. 1995, ApJ, 450, 512

Steidel, C., Adelberger, K., Dickinson, M., Giavalisco, M., Pettini, M., & Kellogg, M. 1998, ApJ, 492, 428

Steidel, C. C., Adelberger, K. L., Giavalisco, M., Dickinson, M., & Pettini, M. 1999, ApJ, 519, 1

Steidel, C. C., Giavalisco, M., Dickinson, M., & Adelberger, K. L. 1996a, AJ, 112, 352

Steidel, C. C., Giavalisco, M., Pettini, M., Dickinson, M., & Adelberger, K. L. 1996b, ApJ, 462, 17

Steidel, C. C. & Hamilton, D. 1993, AJ, 105, 2017

Steidel, C. C., Pettini, M., & Adelberger, K. 2001, ApJ, 546, 665

Steidel, C. C., Pettini, M., & Hamilton, D. 1995, AJ, 110, 2519

Tamura, N., Kobayashi, C., Arimoto, N., Kodama, T., & Ohta, K. 2000, AJ, 119, 2134

Tamura, N. & Ohta, K. 2000, AJ, 120, 533

Teplitz, H. I., Malkan, M.A., Steidel, C. C., McLean, I. S., Becklin, E. E., Figer, D. F., Gilbert, A. M., Graham, J. R., Larkin, J. E., Levenson, N. A., & Wilcox, M. K. 2000a, ApJ, 542, 18

Teplitz, H. I., Mclean, I. S., Becklin, E. E., Figer, D. F., Gilbert, A. M., Graham, J. R., Larkin, J. E., Levenson, N. A., & Wilcox, M. K. 2000b, ApJ, 533, 65

Thompson, R. I., Storrie-Lombardi, L. J., Weymann, R. J., Rieke, M. J., Schneider, G., Stobie, E., & Lytle, D. 1999, AJ, 117, 17

Tinsley, B. M., & Gunn, J. E., 1976, ApJ, 203, 52

Trujillo, I., Aguerri, J. A. L., Cepa, J., & Gutiérrez, C. M. 2001, MNRAS, 321, 269

Vader, J. P., Vigroux, L., Lachieze-Rey, M., & Souviron, J. 1988, A&A, 203, 217

Van Den Bergh, S. V., Abraham, R. G., Ellis, R. S., Tanvir, N. R., Santigo, B.X., & Glazebrook, K. G. 1996, AJ, 112, 359

Van Den Bergh, S. V., Cohen, J. G., Hogg, D. W., & Blandford, R. 2000, AJ, 120, 2190

Wang, B. & Heckman, T. 1996, ApJ, 457, 645

Weschler, R.H., Somerville, R. S., Bullock, J. S., Kollatt, T. S., Primack, J. R., Blumenthal, G. R., & Dekel, A. 2001, ApJ, 554, 85

White, S. D. & Frenk, C. S. 1991, ApJ, 379, 52

Williams, R. E., Blacker, B., Dickinson, M., Dixon, W. V., Ferguson, H. C., Fruchter, A. S., Giavalisco, M., Gilliland, R. L., Heyer, I., Katsanis, R., Levay, Z., Lucas, R. A., McElroy, D. B., Petro, L., Postman, M., Adorf, H., & Hook, R. 1996, AJ, 112, 1335

Wise, M. W. & Silva, D. R. 1996, ApJ, 461, 155

Wu, K. 1999, Ph.D. Thesis, University of California, Santa Cruz

Yahata, N., Lanzetta, K. M., Chen, H., Fernández-Soto, A., Pascarelle, S. M., Yahil, A., & Puetter, R. C. 2000, ApJ, 538, 493

Zepf, S. E., Moustakas, L. A., & Davis, M. 1997, ApJ, 474, L1

BIOGRAPHICAL SKETCH

I was born in Battambang, Cambodia in 1974. In 1975, the fanatic Khmer Rouge regime took over the country and evacuated the cities. The Khmer Rouge wanted to transform Cambodia into a self-sufficient agrarian communist state and distrusted all wealthy or intellectual people. The 4-year-long war was responsible for taking the lives of 1.5 million out of a population of 7 million Cambodians. In January 1979, Vietnam invaded Cambodia and the Khmer Rouge soldiers scattered and hid in the forests. The reign of terror was finally over. My family and I escaped to Thailand and lived for a few months at the refugee camp Khao-I-Dang. Under the effort and sponsorship of my grandfather, we were able to leave for the U.S. in 1980.

Ever since I was a child, I was fascinated with thoughts of the Universe. I asked my aunt, Suntary, such questions as how did we come to be and does the Universe have a boundary? She told me that she didn't know the answers, but that when I grew up, I could study these questions at the university. I was excited to think that it was actually something I could study at school.

During the summer of 1992, I had an internship at the Tech Museum of Innovation. It was during this time that I became very impressed by the marvels of science and technology. Thus, when I graduated from Santa Clara High school in 1993 and attended the University of California at Berkeley, I knew right away that I would major in Astronomy, the subject that has fascinated me since I was little. During the summer of 1996, I was an intern at the Lunar and Planetary Institute in Houston, TX. I worked for Dr. Deborah Domingue on a project comparing the spectra of Io taken during the Voyager and Galileo missions to observe for

changes in the composition of sulfur dioxide. In 1997, I graduated from Berkeley and packed my bags to travel all the way across the country to the land of the Gators. During the several years of research with Dr. Richard Elston, I was able to understand more about the early Universe by studying the properties of high-redshift galaxies. This dissertation has allowed me to investigate the questions that have fascinated me since childhood.

I certify that I have read this study and that in my opinion it conforms to acceptable standards of scholarly presentation and is fully adequate, in scope and quality, as a dissertation for the degree of Doctor of Philosophy.

Richard J. Elston, Chair
Professor of Astronomy

I certify that I have read this study and that in my opinion it conforms to acceptable standards of scholarly presentation and is fully adequate, in scope and quality, as a dissertation for the degree of Doctor of Philosophy.

Fredrick Hamann III
Associate Professor of Astronomy

I certify that I have read this study and that in my opinion it conforms to acceptable standards of scholarly presentation and is fully adequate, in scope and quality, as a dissertation for the degree of Doctor of Philosophy.

Rafael L. Guzmán
Associate Professor of Astronomy

I certify that I have read this study and that in my opinion it conforms to acceptable standards of scholarly presentation and is fully adequate, in scope and quality, as a dissertation for the degree of Doctor of Philosophy.

Vicki L. Sarajedini
Assistant Professor of Astronomy

I certify that I have read this study and that in my opinion it conforms to acceptable standards of scholarly presentation and is fully adequate, in scope and quality, as a dissertation for the degree of Doctor of Philosophy.

James N. Fry
Professor of Physics

This dissertation was submitted to the Graduate Faculty of the Department of Astronomy in the College of Liberal Arts and Sciences and to the Graduate School and was accepted as partial fulfillment of the requirements for the degree of Doctor of Philosophy.

December 2003

Winfred M. Phillips
Dean, Graduate School